FREEPLAY INDUCED LIMIT CYCLE OSCILLATION PREDICTION BY USING EQUIVALENT STIFFNESS METHODOLOGY

A THESIS SUBMITTED TO
THE GRADUATE SCHOOL OF NATURAL AND APPLIED SCIENCES
OF
MIDDLE EAST TECHNICAL UNIVERSITY

BY

MURAT AYDIN

IN PARTIAL FULFILLMENT OF THE REQUIREMENTS
FOR
THE DEGREE OF MASTER OF SCIENCE
IN
AEROSPACE ENGINEERING

DECEMBER 2023

Approval of the thesis:

FREEPLAY INDUCED LIMIT CYCLE OSCILLATION PREDICTION BY USING EQUIVALENT STIFFNESS METHODOLOGY

submitted by **MURAT AYDIN** in partial fulfillment of the requirements for the degree of **Master of Science** i**n Aerospace Engineering, Middle East Technical University** by,

Prof. Dr. Halil Kalıpçılar
Dean, Graduate School of **Natural and Applied Sciences** _____

Prof. Dr. Serkan Özgen
Head of the Department, **Aerospace Engineering** _____

Prof. Dr. Altan Kayran
Supervisor, **Aerospace Engineering, METU** _____

Examining Committee Members:

Prof. Dr. Demirkan Çöker
Aerospace Engineering Dept., METU _____

Prof. Dr. Altan Kayran
Aerospace Engineering Dept., METU _____

Assoc. Prof. Dr. Melin Şahin
Aerospace Engineering Dept., METU _____

Asst. Prof. Dr. Görkem Eğemen Güloğlu
Aerospace Engineering Dept., METU. _____

Assoc. Prof. Dr. Turaç Farsadi
Mechanical Engineering Dept., ATÜ _____

Date: 11.12.2023

I hereby declare that all information in this document has been obtained and presented in accordance with academic rules and ethical conduct. I also declare that, as required by these rules and conduct, I have fully cited and referenced all material and results that are not original to this work.

Name Last name : Murat Aydın

Signature :

ABSTRACT

FREEPLAY INDUCED LIMIT CYCLE OSCILLATION PREDICTION BY USING EQUIVALENT STIFFNESS METHODOLOGY

Aydın, Murat
Master of Science, Aerospace Engineering
Supervisor : Prof. Dr. Altan Kayran

December 2023, 153 pages

This study examines the aeroelastic instability effect of freeplay on an aircraft using the equivalent stiffness methodology. The main motivation of the equivalent stiffness method is that it is also applicable for actuators implemented finite element model. The offset moment requires the modelling of total rotational stiffness around the hinge line with spring element which is CBUSH element in Nastran. The equivalent stiffness methodology is applicable for both bush and actuator implemented finite element model. The 3 DOF airfoil case and AGARD 445.6 wing with loosened root connection are used to validate the equivalent stiffness approach. In the validation phase, ZAERO Nonlinear Flutter Module (NLFLT) is used. METU Very Light Aircraft Model (VLA) is selected to apply the equivalent stiffness methodology on a complete aircraft for both bush and actuator implemented finite element model. The structural and aeroelastic models are created in MSC Nastran/Patran. A set of points are selected from the envelope, and analyses are performed for different flight conditions with different freeplay angles. The maximum free-play limits of control surfaces are determined by following the maximum pilot seat acceleration limitation that it should not exceed the ± 0.12g. The results show that the effect of elevator freeplay on the pilot seat acceleration is the

highest one, and it should have the smallest freeplay limit. The rudder has no LCO behavior due to the absence of the flutter mechanism in the envelope for both zero and nominal rotational stiffness around the hinge line. Apart from the determination of allowable maximum freeplay limits of each control surface alone, the combined control surface freeplay analysis is also conducted in this study. The results show that the combined freeplay case is the most critical one while determining the maximum allowable freeplay limits.

Keywords: Aeroelasticity, Freeplay, Fictitious mass approach, Equivalent stiffness, Limit cycle oscillation

ÖZ

EŞDEĞER SERTLİK METODOLOJİSİ KULLANILARAK BOŞLUKLU YAPI KAYNAKLI LİMİT DÖNGÜ SALINIMI TAHMİNİ

Aydın, Murat
Yüksek Lisans, Havacılık ve Uzay Mühendisliği
Tez Yöneticisi: Prof. Dr. Altan Kayran

Aralık 2023, 153 sayfa

Bu çalışma, eşdeğer sertlik yöntemini kullanarak serbest oynamanın bir uçak üzerindeki aeroelastik kararsızlık etkisini incelemektedir. Eşdeğer sertlik yönteminin ana motivasyonu, eyleyicilerle modellenmiş sonlu elemanlar modeli için de uygulanabilir olmasıdır. Offset moment yöntemi, Nastran'da CBUSH elemanı olan yay elemanı ile menteşe ekseni etrafındaki toplam dönme sertliğinin modellenmesini gerektirir. Eşdeğer sertlik metodolojisi ise yay veya eyleyici ile modellenmiş sonlu eleman modeli için uygulanabilirdir. Eşdeğer sertlik metodolojisini doğrulamak için 3 serbestlik dereceli (3 DOF) kanat profili ve kök bağlantısı gevşetilmiş AGARD 445.6 kanat kullanılmıştır. Doğrulama aşamasında ZAERO Doğrusal Olmayan Çarpıntı Modülü (NLFLT) kullanılmıştır. ODTÜ Çok Hafif Uçak Modeli (VLA), hem yay hem de eyleyici ile modellenerek eşdeğer sertlik metodolojisini komple bir uçakta uygulamak üzere seçilmiştir. Yapısal ve aeroelastik modeller MSC Nastran/Patran'da oluşturulmuştur. Uçus zarfından bir dizi nokta seçilmiş ve farklı serbest oyun açılarına sahip farklı uçuş koşulları için analizler yapılmıştır. Kontrol yüzeylerinin maksimum serbest oynama limitleri, ±0,12g'yi aşmaması gereken maksimum pilot koltuğu ivmelenmesi sınırlaması takip edilerek belirlenmiştir. Sonuçlar, irtifa dümeninin serbest boşluğunun pilot koltuğu ivmesi üzerindeki

etkisinin en yüksek olduğunu ve en küçük serbest oynama sınırına sahip olması gerektiğini göstermektedir. Menteşe ekseni etrafında hem sıfır hem de nominal dönme sertliği için uçuş zarfında çırpıntı mekanizmasının bulunmamasından dolayı istikamet dümeninin LCO davranışı yoktur. Bu çalışmada, her bir kontrol yüzeyinin izin verilen maksimum serbestlik sınırlarının ayrı ayrı belirlenmesinin yanı sıra, birleşik kontrol yüzeyi serbestlik analizi de yapılmıştır. Sonuçlar, izin verilen maksimum serbest oyun limitlerinin belirlenmesinde, birleşik serbest oyun durumunun en kritik durum olduğunu göstermektedir.

Anahtar Kelimeler: Aeroelastisite, Boşta hareket davranışı, Eşdeğer sertlik, Limit döngü salınım

To my family …

ACKNOWLEDGMENTS

I want to express my deepest gratitude to my thesis advisor, Prof. Dr. Altan Kayran, for his support, guidance, and valuable insights throughout the thesis study.

In this study, the model of the METU-VLA project is used. I want to express my gratitude to all the project members who contributed to this project, as well as METU and Turkish Aerospace Industries, Inc., for their support in project.

I am deeply grateful to my beloved family, Dilek Aydın and Servet Aydın, and my sister, Sinem Aydın, for their endless support throughout my education. I extend my heartfelt gratitude to Burcu Kalkan, for her endless support and encouragement to continue this journey.

Lastly, my thanks are to my friend, Oğuzhan Köse. I am grateful for his valuable insights, which have significantly contributed to the improvement of my work. I am sincerely grateful for his friendship and guidance. Furthermore, I want to extend my special thanks to Ayberk Yurtsever, and Özgür Zafer for their endless friendships and support.

TABLE OF CONTENTS

LIST OF TABLES

TABLES

LIST OF FIGURES

FIGURES

LIST OF ABBREVIATIONS

ABBREVIATIONS

AIC	Aerodynamic Influence Coefficient Matrix
CG	Center of Gravity
DLM	Doublet-lattice Method
DOF	Degrees of Freedom
FEM	Finite Element Model
FM	Fictitious Mass
GAF	Generalized Aerodynamic Forces
GFEM	Global Finite Element Model
IPS	Infinite Plate Spline
LCO	Limit Cycle Oscillation
MAC	Modal Assurance Criteria
VLA	Very Light Aircraft

LIST OF SYMBOLS

SYMBOLS	
A_0	Aerodynamic Stiffness
A_1	Aerodynamic Damping
A_2	Aerodynamic Mass
c	Reference Chord
C	Damping Matrix
CL	Control Loop Stiffness
F_S	Equivalent Stiffness Ratio
g	Gravitational Acceleration
GM	Generalized Mass
GK	Generalized Stiffness
Hz	Hertz
k	Reduced Frequency
K	Stiffness Matrix
M	Mass Matrix
M_f	Fictitious Mass
q_∞	Dynamic Pressure
Q_{hh}	Generalized Aerodynamic Force Matrix
V	Free-Stream Velocity
x	Displacement
x_b	Generalized Coordinate Eigenvectors
X_1	Maximum Amplitude of Motion
ρ	Air Density
ϕ	Modal Matrix
ω	Circular Frequency
ξ	Modal Coordinate
δ_0	Freeplay Angle

$\emptyset$	Phase Angle
δ	Control Surface Deflection
β	Aerodynamic Lag Root

CHAPTER 1

INTRODUCTION

1.1 Focus of Aeroelasticity

The academic field of aeroelasticity encompasses a variety of studies aimed at understanding and solving the complex dynamics of aircraft and other flexible structures subjected to aerodynamic forces. It is an interdisciplinary subject that examines the complex interactions between the structural properties of these systems and the aerodynamic loads acting on them, using the concepts of structural mechanics, control theory, and aerodynamics. The researchers aim to understand better the structural response, stability, and control by exploring the key ideas and phenomena underlying the aeroelastic behavior. This will lead to improvements in the creation, use, and safety of aviation systems.

The study of structural response to aerodynamic loads is one of the main areas of aeroelasticity. To predict and control the behavior of an aircraft in flight, it is necessary to understand how its flexible structure interacts with the complex flow field around it. Researchers study the dynamics of vibrations, strains, and stresses caused by aerodynamic forces to build precise analytical and computational models to predict and optimize the structural response. The aim is to explore how structural behavior is affected by the material properties, geometric configurations, and loading conditions and how uncertainties and fluctuations in the operating environment affect this.

Stability analysis is another critical topic in aeroelastic research. Analyzing the ability of an aeroelastic system to maintain stability and resist oscillation or deflection behavior is critical to determining its stability. Researchers investigate

various stability criteria, such as flutter and control reversal, to ensure that aircraft are stable and safe throughout the operating envelope. How structural changes affect the stability of the system should be examined carefully. The dynamic instability caused by the interaction of aerodynamic forces and structural vibrations can have disastrous effects. Therefore, flutter events must be thoroughly investigated and addressed when designing and operating aircraft. Engineers can set safe operating limits by identifying flutter speeds and flight conditions and ensuring structural integrity and stability. A thorough understanding of flutter also helps to establish effective control mechanisms and design techniques to reduce its incidence. Aircraft safety, performance, and reliability can be significantly improved by implementing appropriate safeguards to suppress or prevent flutter. Flutter analysis is essential as it helps to maintain control of aviation vehicles, prevents structural failures, and ensures safe operation in various flight conditions. It is also essential to examine how aeroelastic stability interacts with other flight dynamics, such as impulse response and maneuvering, for detailed aircraft design and control.

Difficulties in incorporating aeroelastic factors into aircraft design are also addressed in aeroelastic research. To achieve this, methods, tools, and standards must be developed for aeroelastic analysis, validation, and optimization. To better capture aeroelastic phenomena and simplify their integration into the design cycle, researchers improve the accuracy and efficiency of computational methods such as finite element models, computational fluid dynamics, and multidisciplinary optimization. By incorporating aeroelasticity into the design process and considering aeroelastic effects early in the design phase, engineers can improve aircraft performance, reduce development costs, and ensure compliance with certification standards.

In summary, studying aeroelasticity is a dynamic, interdisciplinary discipline essential to understand how flexible structures such as airplanes respond to aerodynamic forces. To better understand and control aeroelastic processes,

researchers in this discipline focus on exploring the integration of structural responses, stability, control, and design.

1.2 Definition of Nonlinear Aeroelasticity

The study of the complex interactions and dynamic behavior that occur when there are gaps between structural elements in aeroelastic systems is known as nonlinear aeroelasticity due to freeplay. Small relative displacements or erratic interactions between system components are called "freeplay" and can result from manufacturing tolerances, wear, or deliberate design decisions [6,25].

Many nonlinear phenomena can be produced by intermittent contacts or impacts between structural components in nonlinear aeroelastic systems. These include chaotic motions, limit cycle oscillations (LCOs), jump phenomena, and snap-slip motions. Of particular interest is the formation of LCOs, which appear as stable, self-sustaining oscillations of amplitude and frequency [14]. Freeplay can cause or worsen these LCOs, due to energy loss and reaccumulating during each cycle caused by intermittent contact between components. This results in a sustained oscillation behavior.

The nonlinearity inherent in aeroelastic systems creates analysis, prediction, and control problems. Traditional linear analytical approaches cannot adequately capture complex dynamics and behavior of freeplay nonlinearity. Advanced numerical simulations, experimental studies, and theoretical evaluations are used to understand the system's response better.

For many reasons, it is essential to investigate the nonlinear aeroelasticity caused by freeplay. It is helpful first to recognize and assess the potential hazards and limitations associated with freeplay in aeroelastic systems. Nonlinearity from freeplay can adversely affect the performance, stability, and structural integrity of

flexible structures. A better understanding of these effects makes it possible to develop design techniques that consider freeplay and reduce their hazards.

The nonlinear aeroelasticity caused by freeplay offers possibilities for creative control methods and strategies. By identifying the nonlinear behavior caused by freeplay, engineers can create custom control algorithms that successfully suppress or prevent unwanted oscillations and imbalances. This may include using adaptive control, active control systems, or passive control techniques to mitigate the consequences of nonlinearity caused by freeplay.

1.3 Objective of Thesis

This study examines the problems that may occur due to freeplay such as LCO, pilot comfortability, fatigue life etc. in the VLA aircraft by using the equivalent stiffness methodology and determines the maximum allowable freeplay limits. The primary motivation behind using the equivalent stiffness method is that it is also suitable for actuators implemented structure. The offset moment necessitates the use of the BUSH element to simulate overall rotational stiffness around the hinge line. The equivalent stiffness technique applies to both the bush and actuator implemented finite element models. The structure can be analyzed without converting to the single spring elements which represent the total rotational stiffness of control surfaces.

1.4 Scope of Thesis

The results of the effects caused by freeplay are expressed in the following sections and concluded.

Chapter 2 presents a literature review on non-linear aeroelasticity, specifically concentrating on the freeplay nonlinearity.

The methods for conducting nonlinear aeroelastic analyses are examined in Chapter 3. The equivalent stiffness methodology is introduced, and the method is validated by using 3 DOF airfoil with freeplay and AGARD 445.6 wing with loosened root connection.

A thorough definition of the structural model of the Very Light Aircraft (VLA) is given in Chapter 4. In this context, the steps used to create the VLA's FEM, the connection modeling of the control surfaces, and normal modes analysis are explained in depth. Then, the control loop measurements technique from GFEM is discussed. The actuator and bush implemented structural models are created. A description of the fictitious mass technique is then provided, followed by a discussion of the application of the fictitious mass technique to both models. The creation of aerodynamic surfaces in the Nastran program is described in Chapter 4, also. After thoroughly describing the technique to transfer the frequency-domain aerodynamic data to the time domain, the frequency-domain and time-domain forces are compared. Finally, the coupling between the structural and aerodynamic models is discussed in detail in Chapter 4. The developed model's spline verification results are examined, and its appropriateness for the aeroelastic analysis is demonstrated.

Chapter 5 explains the methods for conducting nonlinear aeroelastic analysis of the actuator and bush implemented GFEM of the VLA, specifically the freeplay aeroelastic analysis via the equivalent stiffness methodology and discusses the findings of the study for probable freeplay combinations of each control surface. Furthermore, the describing function method which is frequency domain approach for freeplay analysis is explained and the results of describing function method are compared with the results of equivalent stiffness approach.

1.5 Assumptions and Limitations of Study

The primary limitations and assumptions are listed below.

- Aeroservoelastic interactions are not considered.
- No structural damping is assumed.

CHAPTER 2

LITERATURE REVIEW

2.1 Approaches to the Nonlinear Aeroelasticity and Mathematical Modelling of Freeplay

Freeplay can be defined as looseness or flexibility in a system. Gaps can occur at the points where mechanical parts connect or where moving components come together. A variety of factors can cause freeplay. These include reasons such as assembly errors, worn parts, tolerance problems, or material properties. Freeplay may occur over time or during the design or the production phase.

Many freeplay induced damages exist. First, it can cause a degradation in the system performance. A loose or hollow component can cause unwanted movements or vibrations, affecting the system stability and control. It can also affect the distribution of energy-induced loads in the system and lead to excessive stresses or deformations. Freeplay can also shorten the system's life due to fatique, as repetitive loads can worsen slack and cause components to wear out faster. Therefore, freeplay analysis has become critical.

Determination of freeplay limits is also necessary in terms of standards. For example, MIL-A-8870C [1] has limited allowable freeplay limits for control surfaces. In the 1950s, LCOs due to freeplay were described as dangerous instability and even equated with flutter. Hoffmann et al. [2] conducted a wind tunnel study for an unswept all-movable horizontal tail and reported that the critical flutter velocity decreased as the freeplay increased. This wind tunnel experiment also pioneered the questions of what could be the maximum freeplay limits that arose in those years. However, the limits were introduced in the 1950s and only slightly changed afterward. At this point, reaching these limits is sometimes impossible when manufacturing capabilities are considered. In addition, since the freeplay limits are

decided with zero preload, it is thought that they are conservative. However, Kholodar [3] emphasized in his article that in the case of non-zero control surface preload or angle of attack, a certain amount of preload appears to destabilize the structure and leads to unexpected high-frequency oscillations. These findings suggested that airplane control surface freeplay would not be conservative with only zero preload.

In contrast, Chen et al. [4] conducted analyses on the F-16 horizontal tail and showed that freeplay limits are very tight and could be exceeded. It has been shown that preload reduces the amplitude of LCO. Also, Deman Tang et al. [5] also stated in their article that the LCO can be suppressed with the increasing angle of attack.

With the development of mathematical models, wind tunnel results were compared with these models. Researchers generally used three sub-domain modeling in the mathematical modeling of freeplay [6], and they used 3-DOF or 2-DOF airfoil models for validation. Mathematical results of Verstraelen et al. [6] agree with the tunnel results. Some differences exist between the time domain modeling of freeplay and the frequency domain modeling. As mentioned above, there are three subdomains in the time domain solution. However, equivalent linearization is used in the frequency domain. There are different approaches used on this issue. The most famous method is the "Harmonic Balance" or the "Describing Function" method. Bansal et al. [7] described this method as a methodology used to linearize the effects of nonlinear freeplay flutter analysis. It is based on the assumption that when a sinusoidal input is provided, the only significant output of a nonlinear element is the sinusoidal component at the input frequency. It is thought that higher harmonics do not affect the system's behavior. The describing function method calculates the Fourier components of nonlinearity, and only the first-order term is preserved. This procedure yields a similar linear system dependent on the amplitude of nonlinearity, which is freeplay in this example. With this approach, many tunnel data and time domain solution data were compared, and it was seen that there was a good fit [8-14]. Anderson et al. [15] mentions that he used the "Den Hartog Equivalent Spring Equation" to account for freeplay effects during the design phase of the F-22 aircraft.

This approach is based on the same method as harmonic balance. However, Anderson mentions that this method can be conservative. Feixin et al. [16] investigated nonlinear damping behavior for 2-DOF airfoil using the equivalent linearization method.

The equivalent stiffness calculated in the harmonic balance method changes according to the behavior created by the freeplay. This is why it needs to be used with caution. For example, in Anderson et al. [15] the freeplay behavior assumed is shown in Figure 2.1. However, Panchal [17] has included the freeplay effect in many ways in his thesis. These are also shown in Figure 2.2. Chung et al. [18] mentioned the "Perturbation-Incremental Method" in their article. They postulated that with this method they overcame some situations where the harmonic balance method was insufficient.

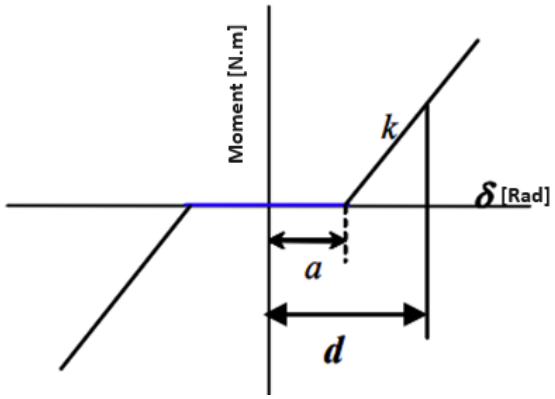

Figure 2.1. Freeplay Modelling of Anderson [15]

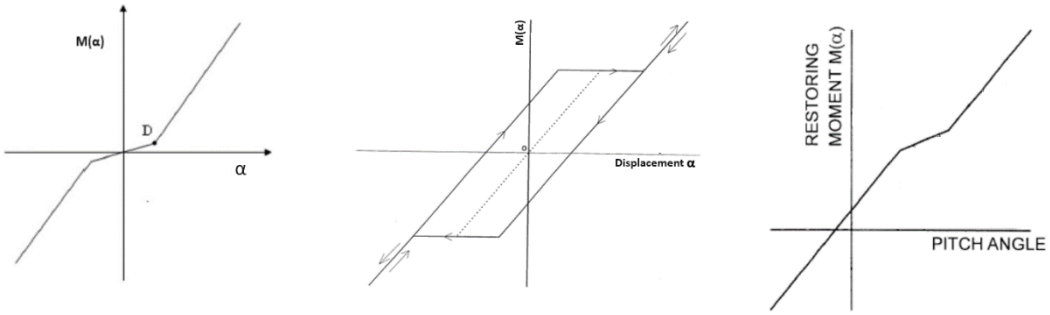

Figure 2.2. Freeplay Modelling of Panchal [17]

The method generally used in time domain analysis is the "Offset Moment Method." It provides a simple method for estimating the effect of various nonlinearities. The technique assumes that freeplay can be represented as a system moment. This moment is directly related to the displacement of the freeplay element from its neutral position.

The “Offset Moment Method” approaches a nonlinear system as a linear one by adding an extra moment offset that eliminates the consequences of nonlinear freeplay. As a result, the system has three linear sub-domains. Adding some amount of an offset moment, the system is modified into a linear system with updated parameters. Following this, the analysis is performed using typical linear techniques. The definition of offset moment is shown in Figure 2.3. In this figure, δ and β are the freeplay angle and the control surface rotation angle, respectively. Unlike Offset Moment, freeplay in 3-DOF airfoil approximation can also be mathematically modeled as a "Hyperbolic Tangent Representation" for time domain analysis [19].

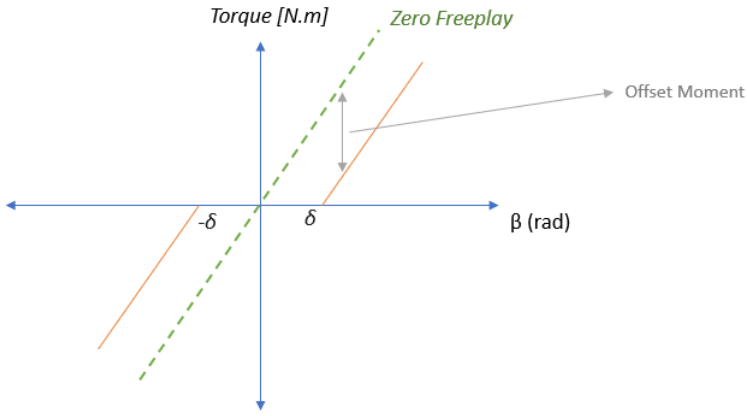

Figure 2.3. Offset Moment Definition

P.C. Chen et al. [20] and P.C. Chen et al. [4] used the offset moment approach while performing folding wing analysis and F-16 analysis, respectively. The primary purpose of time domain calculations is solving a system of ODEs. Therefore, the numerical solution has an important place in it. In their article, Dai et al. [21] conducted investigations on this subject. They compared the results of the classical

RK-4 and Henon method implemented RK-4. The Henon method aims to find the exact switching point between sub-domains. He mentions that chaotic motion cannot be captured with the RK-4 method, and finding the switching point is essential. Y.M. Chen et al. [22] also discussed the importance of having a switching point in their article. They argued that it could be solved more efficiently by implementing the "Precise Integration Method." In this sense, the chosen numerical solver method is essential. Conner et al. [23,24] compared the wind tunnel results for 3 DOF airfoils with the time-domain results implemented and resolved by the Henon method and found a good fit.

Apart from these, Kholodar [25] examined the stability envelopment of a jet aircraft. In this study, the flutter analysis was performed by using zero rotational stiffness of the control surface which has a freeplay. The study concluded that if any instability point occurs within the envelope for zero stiffness of the control surface, the LCO will be seen at that point in the envelope due to freeplay. It means that the system should have an aeroelastic instability in the freeplay region to get LCO. This is important because the LCO regions of the aircraft can be determined quickly.

2.2 Fictitious Mass Approach

Fictitious masses (FM) are used to improve the accuracy and efficiency of modal-based structural assessments including substructure synthesis, local excitation, and local structural alterations. During normal-mode analysis, fictitious masses are added to specified coordinates in the finite element model and then removed, resulting in modes with localized deformations around the selected points in addition to the nominal natural vibration modes.

Large masses, on the other hand, are used to produce static constraint modes for modal coupling with defined bounds. These masses are many orders of magnitude greater and help to depict rigid-body relative motion between structural parts, notably in load analysis. The use of fictitious masses as optional elements within

existing structural dynamic techniques facilitates their integration in conventional practices. This enables increased flexibility and extended capabilities in structural system analysis.

FM method is a precise mathematical method for estimating the impacts of freeplay, yielding more realistic outcomes. Even if the stiffness characteristic of the structure varies, the modal coordinates remain constant in this technique, and it is the most precise way to move between sub-domains.

In the paper, Karpel et al. [26] describes FM as a functional technique that can be used to a wide range of modal-based issues with localized effects. The major goal of this work was to depict local structural changes such as freeplay do not directly affect the modal coordinates, and as a result, the analysis time is drastically decreased. Karpel [38] goes on to address the significant local structural change in aeroelastic calculations. This study deals with the development of time-domain aeroelastic equations with a focus on their capacity to manage considerable local structural changes with a small number of generalized coordinates. A fundamental aeroelastic model is built using computed vibration modes and corresponding aerodynamic force matrices, allowing for the study of structural modifications with the addition of mass, stiffness, and damping coupling factors. In comparison to the old method, the methodology proposes that fewer modes are required, allowing for more efficient analysis of stiffness changes. Also, Karpel and Wieseman [39] used this technique in time-domain solutions for flutter that employs a state-space model with a small number of generalized coordinates. It assesses structural changes effectively by combining vibration modes and aerodynamic force coefficients.

The implementation of the FM method starts with adding a huge fictitious mass to the location where stiffness change occurs. After the addition of fictitious mass, the equation of motion becomes,

$$\left[M + M_f\right]\ddot{x} + [K]x = 0 \tag{2.1}$$

FM is huge enough which won't create numerical issue. The generalized mass and stiffness matrices are then given as,

$$[GM_f] = [\phi_f]^T [M + M_f][\phi_f] \tag{2.2}$$

$$[GK_f] = [\phi_f]^T [K][\phi_f] \tag{2.3}$$

where $[\phi_f]$ is the fictitious mass eigenvectors. The FMs are then removed. The stiffness of the structure that is to be analyzed may be different from the structure which fictitious mass applied. In this case, a coordinate transformation should be performed for desired structural case whose stiffness matrix may differ from the fictitious mass applied one [38]. By using fictitious mass output, stiffness changes on the location which fictitious mass added can be get correctly by using the Equation 2.4.

$$\det\left|-\left([GM_f] - [\phi_f]^T [M_f][\phi_f]\right)\omega^2 + ([GK_f] - [\phi_f]^T [\Delta K][\phi_f])\right| = 0 \tag{2.4}$$

Results of the Equation 2.4 become natural frequency of the system with stiffness change and the generalized coordinate eigenvectors of actual "basic" system (x_b). The eigenvector of the desired structure can be calculated as,

$$\phi_b = \phi_f * x_b \tag{2.5}$$

As a result, the stiffness change on the structural model can be represented as a linear combination of fictitious mass mode shapes without changing the modal coordinates. The fictitious mass method is used in freeplay analysis to get more accurate and continuous results in transitions between sub-domains.

CHAPTER 3

FREEPLAY MODELING THROUGH THE EQUIVALENT STIFFNESS APPROACH

In this chapter, the equivalent stiffness methodology is explained and verified with two test cases which are 3 DOF airfoil and AGARD 445.6 wing with loosened root connection cases.

3.1 Freeplay Modelling Methodology

For freeplay analysis, as mentioned before, the offset moment method is used generally. The offset moment can be defined as the delta moment between the zero freeplay and existence of the freeplay on the torque vs control surface rotation curve. Figure 2.3 shows the offset moment for a system which includes freeplay.

The offset moment method should be implemented in a state space model to solve the aeroelastic system with freeplay. The general solution of freeplay system can be obtained by using the time domain solutions. State space representation is required to solve the system in the time domain [33]. The state space matrix for an aeroelastic system without any nonlinearity is derived below.

The modal approach to structural dynamics is based on the idea that structural displacements may be appropriately described as a linear combination of certain baseline modes and modal displacement vectors.

$$\{x\} = [\phi]\{\xi\} \tag{3.1}$$

where $\{x\}$ is the structural displacements vector, $\{\xi\}$ is the modal displacements vector and $[\phi]$ is the modal matrix.

Equation 3.2 provides the general description of a discrete system's equation of motion [47].

$$[M]\{\ddot{q}(t)\} + [C]\{\dot{q}(t)\} + [K]\{q(t)\} = \{Q(t)\} \tag{3.2}$$

$[M]$,$[K]$ and $[C]$ matrices in Equation 3.2 represent mass, stiffness, and damping matrices, respectively. $Q(t)$ is the force column vector, and q is the degree of freedom vector reflecting structural deformation. The $Q(t)$ vector can be divided into two as in Equation 3.3.

$$\{Q(t)\} = F_a(q) + F_e(t) \tag{3.3}$$

In Equation 3.3, $F_e(t)$ represents external forces, whereas $F_a(q)$ represents unsteady aerodynamic loads caused by structure deformation. External forces include continuous turbulence, discrete gusts, and aerodynamic forces caused by pilot input commands on control surfaces. Since, flutter is a self-excited phenomena in nature, $F_e(t)$ is taken as zero. If zero structural damping is assumed, Equation 3.4 is formed by combining Equations 3.3 and 3.2.

$$[M]\{\ddot{q}(t)\} + [K]\{q(t)\} - F_a(q) = 0 \tag{3.4}$$

The Aerodynamic Influence Coefficient (AIC) matrix is widely used in dynamic aeroelastic analysis utilizing the DLM to determine the unsteady load vector $F_a(q)$ [36]. The link between the AIC matrix and the deformation and the force exerted on the aerodynamic panels is established by Equation 3.5 [36].

$$\{F_h\} = q_\infty [AIC]\{h\} \tag{3.5}$$

In Equation 3.5, q_∞ represents the dynamic pressure, $\{F_h\}$ is the force acting on the aerodynamic model, and h is the deformation of the aerodynamic boxes. As mentioned before, the DOFs of the aerodynamic panels and structural model are not the same. Therefore, spline matrices are used. The spline matrix allows displacements to be transferred from the structural model to the aerodynamic model, allowing a link between the two components of an aeroelastic system.

$$\{h\} = [G]\{q\} \tag{3.6}$$

The spline matrix not only transfers displacements from the structural model to the aerodynamic model, but it also transfers the aerodynamic loads back to the structural model. In Equation 3.6, $[G]$ is referring the spline matrix. Equation 3.7 may be written using the virtual work method [47].

$$\{\delta h\}^T\{F_h\} = \{\delta q\}^T\{F_a\} \tag{3.7}$$

In Equation 3.7, $\{F_a\}$ denotes aerodynamic forces acting on the structural element, $\{F_h\}$ represents aerodynamic forces on aerodynamic boxes, and δh and δq refers to the virtual displacement vectors on the aerodynamic and structural grids, respectively.

When Equation 3.6 and 3.7 are combined, Equation 3.8 is obtained.

$$\{\delta q\}^T([G]^T\{F_h\} - \{F_a\}) = 0 \tag{3.8}$$

As the virtual displacement vector cannot be zero, the expression within the parentheses in Equation 3.8 must be equated to zero. Consequently, by using the spline matrix $[G]$, forces can be effectively transferred from the aerodynamic boxes to the structural finite element grid points, as given in Equation 3.9.

$$\{F_a\} = [G]^T\{F_h\} \tag{3.9}$$

Aerodynamic forces on the structural model can be obtained when Equation 3.5, 3.6 and 3.9 are combined [47].

$$\{F_a\} = q_\infty[G]^T[AIC][G]\{q\} \tag{3.10}$$

The equation motion given in Equation 3.4 can be written in generalized coordinates as,

$$[GM]\{\ddot{\xi}\} + [GK]\{\xi\} = [Q_{HH}] \tag{3.11}$$

where; $[GM]$,$[GC]$ and $[GK]$ are the generalized mass, damping and stiffness matrices with respect to the modal matrix $[\phi]$, respectively. Also, $[Q_{HH}]$ is the generalized aerodynamic force matrix.

$$[GM] = [\phi]^T[M][\phi] \tag{3.12}$$

$$[GK] = [\phi]^T[K][\phi] \tag{3.13}$$

$$[GC] = [\phi]^T[C][\phi] \tag{3.14}$$

$$[Q_{HH}] = [\phi]^T\{\mathrm{F_a(t)}\} = q_\infty[\phi]^T[G]^T[AIC][G][\phi]\{\xi(t)\} \tag{3.15}$$

Prior to building the nonlinear aeroelastic model, aerodynamic forces in Equation 3.11 must be represented in time-domain. This requires transferring the aerodynamic forces from the frequency domain to the time domain using the Rational Function Approximation (RFA). This phase requires converting the GAF matrices from the frequency domain to the Laplace (s) domain. It should be noted that the GAF matrices are initially computed for discrete reduced frequencies. However, because the Laplace domain is continuous, a particular expression is assumed during this transformation procedure. Therefore, the assumption given in Equation 3.16 is made. In Equation 3.16, 's' is the Laplace variable, 'k' is the reduced frequency ($\frac{\omega c}{2V}$) where, V, c and ω are the freestream velocity, reference chord length and harmonic frequency in rad/sec, respectively. The parameter 'g' extends the unsteady aerodynamics from the imaginary axis to the entire Laplace domain [40]. The parameter 'g' is neglected throughout the GAF matrix creation process [40]. However, the neglecting the 'g' causes another problem on approximation which is shown in Figure 3.1. The transformation requires introducing aerodynamic lag roots on the negative axis, aligning with the negative real axis in the Laplace domain, facilitating a smooth transition to the time domain using Inverse Fourier Transform methods and resolving discontinuity by strategically placing lag roots, as shown in Figure 3.2 [40].

$$g + jk = \frac{sc}{2V} \tag{3.16}$$

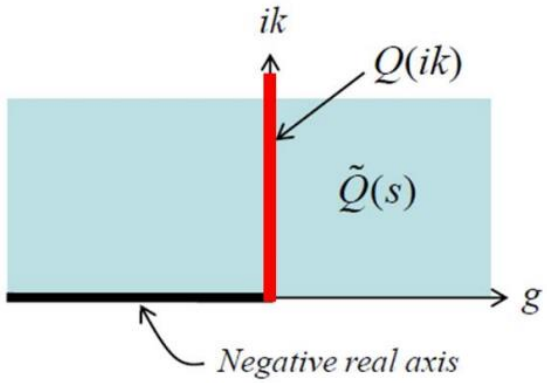

Figure 3.1. Representation of Transformation of GAF from Frequency Domain to the Laplace Domain [40]

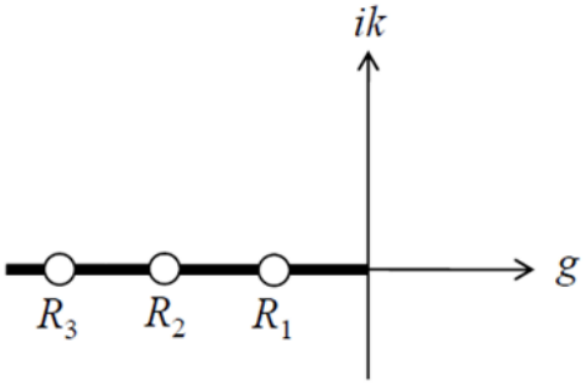

Figure 3.2. Aerodynamic Lag Roots [40]

The approximation of the aerodynamic forces in the Laplace domain can be written as in Equation 3.17 [33].

$$Q(s) = A_0 + \left(\frac{c}{2V}\right) sA_1 + \left(\frac{c}{2V}\right)^2 s^2 A_2 + \sum_{n=1}^{M} \frac{sA_{n+2}}{\left(s + \frac{2V}{c}\beta_n\right)} \tag{3.17}$$

where, A_0, A_1, A_2 are aerodynamic stiffness, damping and mass matrices, respectively. These matrices can be calculated by using the least square method to

fit Equation 3.17 [33]. In addition to this, β_n are the aerodynamic lag roots. M is the partial fractions which is equal to the order of the overall denominator of polynomial.

The aerodynamic lag term can be represented as an extra variable ξ_{ai} which is called as augmented state [33].

$$\xi_{ai}(s) = \frac{s}{\left(s + \frac{2V}{c}\beta_{n-2}\right)}\xi(s) \tag{3.18}$$

The first stage is to formulate the aerodynamic mass, damping and stiffness terms of the rational function approximation of GAF matrices while taking into account the effect of structural mode shapes (ξ) [40].

$$Q(\xi) = A_0\{\xi(t)\} + \left(\frac{c}{2V}\right)A_1\{\dot{\xi}(t)\} + \left(\frac{c}{2V}\right)^2 A_2\{\ddot{\xi}(t)\} \tag{3.19}$$

Then, $\xi(s)$ can be written as given in Equation 3.20 by using the Equation 3.18 [41].

$$\xi(s) = \xi_{ai}(s) + \xi_{ai}(s) * \frac{\frac{2V}{c}\beta_{n-2}}{s} \tag{3.20}$$

The inverse Laplace transform can be performed after multiplying each side of Equation 3.20 with the Laplacian variable 's'.

$$s\xi(s) = \xi_{ai}(s)s + \xi_{ai}(s) * \frac{2V}{c}\beta_{n-2} \tag{3.21}$$

Then, the inverse Laplace transform of Equation 3.21 becomes,

$$\dot{\xi}(t) = \dot{\xi}_{ai}(t) + \xi_{ai}(t) * \frac{2V}{c}\beta_{n-2} \tag{3.22}$$

Now, the Laplace domain aerodynamic approximation of GAF which is given in Equation 3.17 can be written in time domain with the augmented states.

$$Q(\xi) = A_0\{\xi(t)\} + \left(\frac{c}{2V}\right)A_1\{\dot{\xi}(t)\} + \left(\frac{c}{2V}\right)^2 A_2\{\ddot{\xi}(t)\} + \sum_{n=3}^{M} A_n\,\xi_{ai} \tag{3.23}$$

$$\dot{\xi}_{ai}(t) = \dot{\xi}(t) - \xi_{ai}(t) * \frac{2V}{c}\beta_{n-2} \tag{3.24}$$

Finally, states are defined as,

$$\{x\} = \begin{bmatrix} \xi \\ \dot{\xi} \\ \xi_{ai} \end{bmatrix} \tag{3.25}$$

where, ξ_{ai} are augmented states.

Then, a state-space matrix of an aeroelastic system is generated by using Equations 3.11, 3.23 and 3.24.

$$\{\dot{x}\} = [A]\{x\} \tag{3.26}$$

The expanded form of the state-state matrix is given in Equation 3.27 [33].

$$[\dot{x}] = \begin{bmatrix} 0 & [I] & 0 & 0 & \dots \\ -[M_S]^{-1}[K_s] & -[M_S]^{-1}[B_s] & q[M_S]^{-1}[A_3] & q[M_S]^{-1}[A_4] & \dots \\ 0 & [I] & -\left(\frac{2V}{c}\right)\beta_1[I] & 0 & \dots \\ 0 & [I] & 0 & -\left(\frac{2V}{c}\right)\beta_2[I] & \dots \\ \dots & \dots & \dots & \dots & \dots \end{bmatrix} [x] \tag{3.27}$$

where, $[M_S], [B_s]$ and $[K_s]$ are defined as,

$$[M_S] = [GM] - \frac{1}{2}\rho\left(\frac{c}{2}\right)^2 [A_2] \tag{3.28}$$

$$[B_s] = -\frac{1}{2}\rho\left(\frac{c}{2}\right) V[A_1] \tag{3.29}$$

$$[K_s] = [GK] - \frac{1}{2}\rho V^2[A_0] \tag{3.30}$$

The state-space matrix should be updated for the implementation of the offset moment approach. Figure 3.3 shows the torque versus control surface rotation curve with the freeplay angle being δ_0 and the nominal stiffness value as $K_{Rotational}$. The nominal stiffness can be defined as the stiffness without freeplay. Figure 3.3 shows the discontinuities in stiffness at the freeplay limits ($\delta_0 \; and \; -\delta_0$), which might lead

to unrealistic greater limit cycle oscillations. To overcome this issue, it is suggested that the freeplay modeling be modified by introducing an offset moment [40]. Equation 3.11 is divided into three linear zones described by Equations 3.31-3.33 to handle the nonlinearity and include the freeplay nonlinear behavior into the aeroelastic system. By including offset moment adjustments on the right side of the equations, the three governing equations for the nonlinear aeroelastic problem are formed [40].

$$[GM]\{\ddot{\xi}\} + [GK]_{nom}\{\xi\} - q[Q(ik)]\{\xi\} = [\phi]^T[K]_{Hinge}\{\delta_0\} \quad for\ \delta > \delta_0 \quad (3.31)$$

$$[GM]\{\ddot{\xi}\} + [GK]_{free}\{\xi\} - q[Q(ik)]\{\xi\} = 0 \qquad for\ \delta_0 \geq \delta \geq -\delta_0 \quad (3.32)$$

$$[GM]\{\ddot{\xi}\} + [GK]_{nom}\{\xi\} - q[Q(ik)]\{\xi\} = -[\phi]^T[K]_{Hinge}\{\delta_0\} for\ \delta < -\delta_0 \quad (3.33)$$

In Equation 3.31-3.33, $[GK]_{free}$ represents the generalized stiffness matrix of the aeroelastic system without any rotational stiffness with respect to the hinge axis and $[GK]_{nom}$ which is the generalized nominal stiffness matrix which is the stiffness matrix of the aeroelastic system with the interact control surface rotational stiffness. In addition to this, $[\phi]^T[K_{Hinge}]\{\delta_0\}$ is the offset moment correction with respect to the control surface rotational freeplay angle δ_0. $[K_{Hinge}]$ is defined as,

$$[K]_{Hinge} = [K]_{Nom} - [K]_{free} \quad (3.34)$$

where, $[K]_{Hinge}$ is a matrix which includes a full of zeros except for the related portion which belongs to the control surface rotational stiffness. Also, $\{\delta_0\}$ is a vector which includes zeros except for the corresponding value of rotational DOF of the control surface which is δ_0. The offset moment correction removes the nonlinearity shown in Figure 3.3. By allocating the restoring moments depending on the freeplay zone in the range of control surface rotation, this correction enables a smooth shift in stiffness. Hence, Equations 3.31-3.33 can be used to solve aeroelastic problems involving freeplay effects [40].

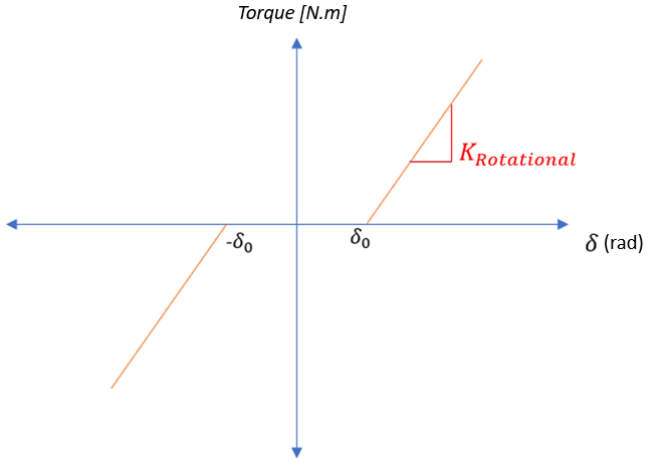

Figure 3.3. Torque vs Rotation Curve

The offset moment equations should be transformed into the state-space form to solve the aeroelastic system of equations in time-domain. The modified state-space matrix becomes as shown in Equation 3.35:

$$\{\dot{x}\} = [A]\{x\} + [Offset\ Moment] \tag{3.35}$$

The sign of the offset moment term changes in time with respect to the deflection of the control surface. It should be noted that in this case Equations 3.31-3.33, all should be converted into the time-domain. Hence, the number of state-space matrices becomes three in this case. The expanded form of Equation 3.35 is given as in Equation 3.36 for $\delta > \delta_0$ as an example [42].

$$[\dot{x}] = \begin{bmatrix} 0 & [I] & 0 & 0 & \dots \\ -[M_S]^{-1}[K_s] & -[M_S]^{-1}[B_s] & q[M_S]^{-1}[A_3] & q[M_S]^{-1}[A_4] & \dots \\ 0 & [I] & -\left(\frac{2V}{c}\right)\beta_1[I] & 0 & \dots \\ 0 & [I] & 0 & -\left(\frac{2V}{c}\right)\beta_2[I] & \dots \\ \dots & \dots & \dots & \dots & \dots \end{bmatrix}[x] + \begin{bmatrix} 0 \\ -[M_S]^{-1}([\phi]^T[K]_{Hinge}\{\delta_0\}) \\ 0 \\ 0 \\ \dots \end{bmatrix} \tag{3.36}$$

It should be noted that concentrated nonlinearity is needed to use the offset moment approach in freeplay analysis. The concentrated nonlinearity means that the total rotational stiffness of the control surface should be represented in a single element in the finite element model. If the FEM of control surfaces includes an actuator system, $[K]_{Hinge}$ term cannot be defined as a rotational stiffness in the stiffness matrix of the finite element model. In addition to this, the total rotational stiffness will be sum of the effects of the actuator, the location at which the actuator is connected, the backup structures of the main and control surfaces. In this case, there will be no stiffness term to multiply with δ_0 to calculate the offset moment, as shown in Equation 3.36. To model the rotational stiffness of the control surface as a single concentrated element, the NASTRAN CBUSH element, which is a concentrated spring element, is generally used. The CBUSH element in NASTRAN is a structural element used to describe connections between two locations in a finite element model, such as bushings or rotating springs. Because it has six degrees of freedom at each end, it can simulate translational and rotational stiffness, making it appropriate for expressing various flexible connections in mechanical systems.

In this study, instead of the offset moment approach, the equivalent stiffness methodology has been used to linearize the stiffness for the current rotation angle of the control surface. The moment vs rotation curve for a freeplay behavior of a control surface is given in Figure 3.3. This behavior can be expressed mathematically as in Equations 3.37-3.39,

$$Torque = K_{Rotational} * (\delta - \delta_0) \qquad for\ \delta > \delta_0 \quad (3.37)$$

$$Torque = 0 \qquad for\ \delta_0 \geq \delta \geq -\delta_0 \quad (3.38)$$

$$Torque = K_{Rotational} * (\delta + \delta_0) \qquad for\ \delta < -\delta_0 \quad (3.39)$$

where $K_{Rotational}$ is the nominal control surface rotational stiffness around hinge line.

At a certain time, t, the equivalent stiffness can be defined as a stiffness which creates the same amount of torque for the current rotation.

$$K_{equivalent} = \frac{Torque}{\delta} \tag{3.40}$$

$K_{equivalent}$ represents the equivalent rotational stiffness of control surface around the hinge line in the aeroelastic model. It should be noted that $K_{equivalent}$ is not a matrix, it is a value of the equivalent rotational stiffness of a control surface around the hinge line. Therefore, stiffness ratio (F_S) can be defined as,

$$F_S = \frac{K_{equivalent}}{K_{Rotational}} \tag{3.41}$$

where, F_S represents the stiffness degradation of the control surface stiffness due to the freeplay. Then, the stiffness matrix of an aeroelastic system can be written as given in Equation 3.42.

$$[K]_{Nom} = [K]_{Hinge} + [K]_{free} \tag{3.42}$$

where $[K]_{Hinge}$ is a matrix which includes full of zeros except for the related portion which belongs to the bush elements of the control surface rotation. $[K]_{Nom}$ which is called the nominal stiffness matrix is the stiffness matrix of the aeroelastic system with the control surface rotational stiffness. $[K]_{free}$ represents the stiffness matrix of the aeroelastic system without rotational stiffness with respect to the hinge axis. Equation 3.42 can be generalized using the generalized coordinates as given in Equations 3.43 and 3.44.

$$[\phi]^T[K]_{Nom}[\phi] = [\phi]^T([K]_{Hinge} + [K]_{free})[\phi] \tag{3.43}$$

$$[\phi]^T[K]_{Nom}[\phi] = [\phi]^T[K]_{Hinge}[\phi] + [\phi]^T[K]_{free}[\phi] \tag{3.44}$$

The freeplay in the aeroelastic system will cause a degradation on the rotational stiffness of control surfaces around the hinge line. This degradation can be implemented as shown in Equation 3.45.

$$[\phi]^T[K]_{equivalent}[\phi] = [\phi]^T([K]_{Hinge} * F_S)[\phi] + [\phi]^T[K]_{free}[\phi] \tag{3.45}$$

where $[K]_{equivalent}$ is the stiffness matrix of an aeroelastic system which includes the equivalent rotational stiffness of the control surface.

Then, $[-[M_s]^{-1}[K_s]]$ term appearing in the state-space equation given by Equation 3.27, can be updated in each time step as follows.

$$[K_s] = [GK'] - \frac{1}{2}\rho V^2 [A_0] \tag{3.46}$$

$$[GK'] = [\phi]^T [K]_{equivalent} [\phi] \tag{3.47}$$

In Equation 3.47, $[GK']$ refers to the equivalent generalized stiffness matrix which includes the equivalent rotational stiffness of control surface and $[\phi]$ is the modal matrix which is extracted after fictitious mass implementation.

An important advantage of the equivalent stiffness approach is the number of subdomains to represent the regions. If the equivalent stiffness methodology is used, there is no need to define any subdomains. The only thing that is needed is that the control surface rotation angle should be checked, and the corresponding moment should be calculated, accordingly. This operation can be done either by calculating torque from Figure 3.3 or by using a look-up table for the torque-control surface rotation curve. However, three possibilities exist for the offset moment approach. These are positive offset moments, zero offset moment and the negative offset moment. In case there are freeplays in multiple components, then, the combination of sublinear systems must be taken into account. For example, if two ailerons exist, the solution needs nine check points for the offset moment approach and two for equivalent stiffness approach. This example is only related to just one component. If there are more than two freeplays in the aeroelastic system, such as aileron, elevator, rudder, this leads to many subdomain conditions. In addition to this, concentrated nonlinearity is required to use the offset moment approach. The overall rotational stiffness of the control surface should be represented in the FEM by a single element. If the control surface FEM model incorporates an actuator system, the $[K]_{Hinge}$ term specified in Equation 3.31 and 3.33 cannot be defined as rotational stiffness in the

FEM stiffness matrix. Furthermore, the overall rotational stiffness depends on the effects coming from the actuator, the location to where the actuator is attached on both the main surface and the control surface [43]. Hence, in the offset moment approach, to compute the offset moment, there is no stiffness term to multiply with the freeplay angle. In the finite element model, the NASTRAN CBUSH element is commonly used to model the concentrated stiffness around the hinge line. However, the rotational stiffness of the surface cannot always be represented by converting it into concentrated bush element in the aeroelastic model. The reason for this is the change of the load path in the control surface and the mode shapes due to the existence of an actual actuator model in the aeroelastic model. In this case, the actuator can be selected as an adjustable element and the equivalent stiffness approach can be used. When an aeroelastic system has an actuator system, total rotational stiffness around the hinge line depends on the actuator-control surface attachment stiffness (control surface backup stiffness), actuator stiffness and the stiffness of the location where the actuator attaches to the main surface (main surface backup stiffness). The representative modelling of the actuation system is shown in Figure 3.4

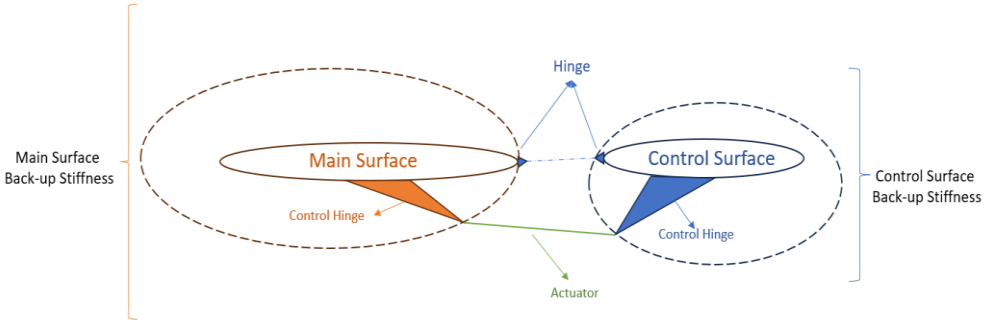

Figure 3.4. Representative Modelling of the Control Surface Actuation System

The total rotational stiffness can be defined as serially connected component stiffness terms [43] as given in Equation 3.48 for the representative model given in Figure 3.4.

$$\frac{1}{Total\ Rotational\ Stiffness} = \frac{1}{Control\ Surface\ Backup\ Stiffness} + \frac{1}{Main\ Surface\ Backup\ Stiffness} + \frac{1}{Actuator\ Stiffness} \tag{3.48}$$

When there is freeplay, it causes a reduction in the total rotational stiffness around the hinge line on the aeroelastic system. If actuator is selected to adjust the nonlinearity, the equivalent actuator stiffness can be found from Equation 3.49.

$$\frac{1}{Equivalent\ Actuator\ Stiffness} = \frac{1}{Equivalent\ Rotational\ Stiffness} - \frac{1}{Main\ Surface\ Backup\ Stiffness} - \frac{1}{Control\ Surface\ Backup\ Stiffness} \tag{3.49}$$

The calculation of main surface and control surface back-up stiffnesses are explained in detail in Chapter 4. Moreover, the equivalent rotational stiffness term is known from Equation 3.40. Then, the stiffness ratio can be calculated as,

$$F_S = \frac{K_{equivalent\ actuator}}{K_{Nominal\ actuator}} \tag{3.50}$$

where $K_{equivalent\ actuator}$ is the equivalent actuator stiffness which is calculated from Equation 3.49 and $K_{Nominal\ actuator}$ is the nominal actuator stiffness value without any reduction due to freeplay. Equation 3.43 can then be rewritten for the actuator implemented system as given in Equation 3.51.

$$[\phi]^T[K]_{Nom}[\phi] = [\phi]^T[K]_{actuator}[\phi] + [\phi]^T[K]_{free}[\phi] \tag{3.51}$$

where $[K]_{actuator}$ is a matrix which includes full of zeros except for the related portion which belongs to the actuator. $[K]_{free}$ represents the stiffness matrix of the aeroelastic system without any actuator stiffness. Then, the equivalent stiffness of the aeroelastic system can be defined as in Equation 3.52.

$$[\phi]^T[K]_{equivalent}[\phi] = [\phi]^T([K]_{actuator} * F_S)[\phi] + [\phi]^T[K]_{free}[\phi] \tag{3.52}$$

By using Equations 3.46,3.47 and 3.52, the effects of freeplay can be analyzed by updating the $[\ -[M_s]^{-1}[K_s]]$ term appearing in the state-space equation given by Equation 3.27 in each time step without using any concentrated rotational stiffness, such as CBUSH in FEM.

In this study, a MATLAB code is generated to the solve state space equation which is shown in Equation 3.27 with changing stiffness. MATLAB ODE45 is used as a numerical solver. Zero-point detection has been enabled to find the exact switching point in the freeplay region. Figure 3.5 shows the general algorithm for the control surface freeplay implementation. The C matrix on state-space matrix in Figure 3.5 maps the state variables (modal displacement, modal velocity etc.) to the output variables such as displacement and acceleration on selected grid points in the FEM. C matrix includes the mode shapes of the grid points which are related with the displacement and acceleration.

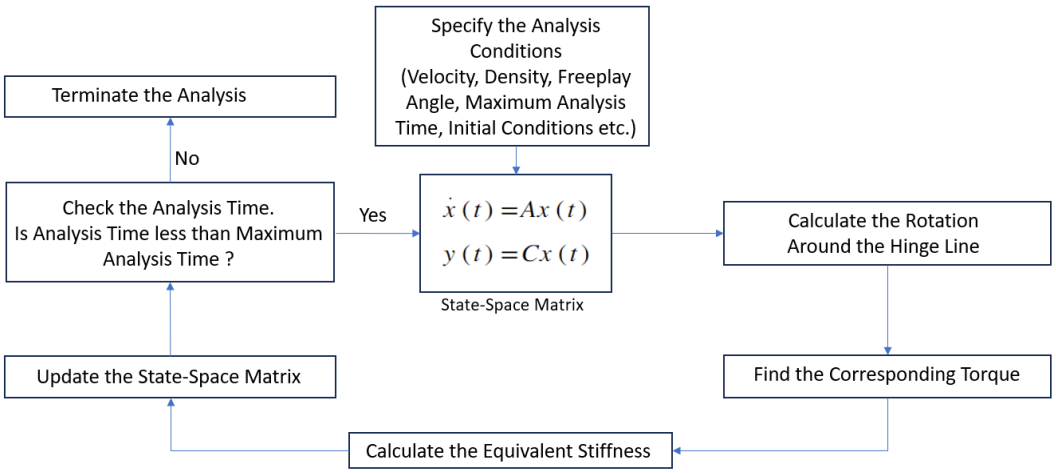

Figure 3.5. The General Algorithm for Freeplay Solutions

3.2 Verification of Equivalent Stiffness Methodology

ZAERO Nonlinear Flutter Module (NLFLT) [30] is used for the verification of the equivalent stiffness methodology. This module presents a thorough technique for modeling nonlinear aeroelastic systems in both open and closed-loop analysis. The

method employs a "nonlinear parameter" methodology to divide nonlinear systems into sub-linear systems, yielding a set of discrete time-domain state-space equations. This enables the simultaneous integration of nonlinearity in structural components, control systems, and unstable aerodynamics. To excite the nonlinear system, external disturbances such as discrete gusts or pilot input commands can be supplied. To solve the state-space equations at each time step, the transient response is determined using an interpolation approach. After obtaining the time-domain solution of the generalized coordinates, the transient response of any parameter of the aeroelastic system may be determined. This module uses the offset moment approach to analyze the freeplay nonlinearity.

3.2.1 Three DOF Airfoil Case

Conner et al. [23] obtained the transient response of a typical airfoil section with control surface freeplay both numerically and experimentally. Figure 3.6 depicts the structural system of an airfoil section with three degrees of freedom (3 DOF), namely the plunge (h), pitch (α), and flap (β). The control surface freeplay is given 2.12°, resulting in the restoring moment diagram illustrated in Figure 3.6. In this case, since the rotational stiffness is decoupled, there is no need for fictitious mass implementation.

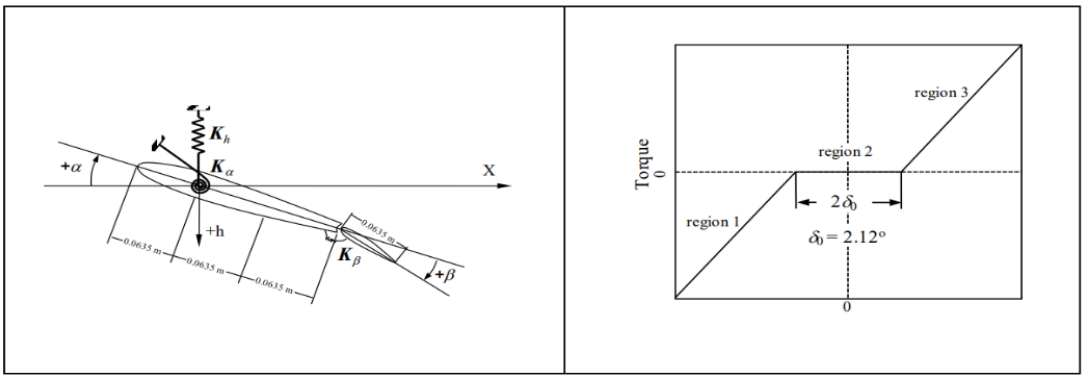

Figure 3.6. Three DOF Airfoil with Freeplay and the Moment Curve [44]

The equation of motion for the 3 DOF airfoil is expressed as [44],

$$[M]\{\ddot{\xi}\} + [C]\{\dot{\xi}\} + [K]\{\xi\} - q_\infty[Q]\{\xi\} = \{M_0\} \qquad \beta > \delta_0 \quad (3.53)$$

$$[M]\{\ddot{\xi}\} + [C]\{\dot{\xi}\} + [K]\{\xi\} - \lambda\{\mathrm{M_B}\} - q_\infty[Q]\{\xi\} = 0 \qquad \delta_0 \geq \beta \geq -\delta_0 \quad (3.54)$$

$$[M]\{\ddot{\xi}\} + [C]\{\dot{\xi}\} + [K]\{\xi\} - q_\infty[Q]\{\xi\} = \{M_0\} \qquad \beta < -\delta_0 \quad (3.55)$$

where,

$[M] = \begin{bmatrix} 3.293 & 0.0859 & 0.0039 \\ 0.0859 & 0.0135 & 0.0008 \\ 0.0039 & 0.0008 & 0.000326 \end{bmatrix}$ is the generalized mass matrix.

$[C] = \begin{bmatrix} 3.29618 & 0.03517 & -0.000356 \\ 0.03517 & 0.03042 & 0.00202 \\ -0.000356 & 0.00202 & 0.0007757 \end{bmatrix}$ is the generalized damping matrix.

$[K] = \begin{bmatrix} K_h & 0 & 0 \\ 0 & K_\alpha & 0 \\ 0 & 0 & K_\beta \end{bmatrix}$ is the generalized stiffness matrix without any freeplay. K_h, K_α and K_β are the plunge, pitch, and control surface stiffness', respectively. In 3DOF airfoil case, the K_h, K_α and K_β are 2818, 37.3 and 3.9, respectively.

Also, $q_\infty[Q]$ is the time domain generalized aerodynamic force matrix. In 3 DOF airfoil model, $\{\xi\}$ is defined as {-h, α, β} [44] where "h" represents a downward vertical displacement, "α" is the pitch angle, and "β" is the relative deflection angle between the airfoil and the control surface.

The vector $\lambda\{\mathrm{M_B}\}$ in the equations of motion captures the nonlinear structural effects arising from freeplay. The λ and $\mathrm{M_B}$ definitions are given in Equation 3.56 and 3.57. δ_0 refers to the freeplay angle.

$$\lambda = \begin{cases} -1, & |\beta| \leq \delta_0 \\ 0, & |\beta| > \delta_0 \end{cases} \quad (3.56)$$

$$\{M_B\} = \begin{bmatrix} 0 & 0 & 0 \\ 0 & 0 & 0 \\ 0 & 0 & K_\beta \end{bmatrix} \begin{bmatrix} 0 \\ 0 \\ \beta \end{bmatrix} + \begin{bmatrix} 0 \\ 0 \\ M_0 \end{bmatrix} \quad (3.57)$$

In addition to this, M_0 in Equation 3.57 is expressed as [44],

$$\{M_0\} = \begin{bmatrix} 0 \\ 0 \\ \overline{M_0} \end{bmatrix} \tag{3.58}$$

where,

$$\overline{M_0} = \begin{cases} K_\beta * \delta_0, & \beta > 0 \\ -K_\beta * \delta_0, & \beta < 0 \end{cases} \tag{3.59}$$

$\overline{M_0}$ is an offset moment.

The experiment on the 3 DOF airfoil system with freeplay was carried out in a low-speed wind tunnel, with airspeeds ranging from 4.3 m/s to 24 m/s [23]. The 3DOF airfoil with freeplay presented in this experiment may be considered as a conventional benchmark study. It provides a solid foundation for verifying nonlinear aeroelastic techniques by demonstrating that the system's behavior can be adequately described and predicted using existing numerical approaches [44].

In this study, GAFs are extracted from ZAERO Flutter Analysis Module for several reduced frequencies. Then, GAFs are converted into time domain by using rational function approximation (RFA) which is explained in detail in section 4.2.1. The state-space matrix which is given in Equation 3.27 is constructed. $[\ -[M_s]^{-1}[K_s]]$ term appearing in the state-space equation is updated in each time step as follows,

$$[K_s] = [GK'] - \frac{1}{2}\rho V^2 [A_0] \tag{3.60}$$

where,

$$[GK'] = \begin{bmatrix} 2818 & 0 & 0 \\ 0 & 37.3 & 0 \\ 0 & 0 & 3.9 * F_s \end{bmatrix} \tag{3.61}$$

Figure 3.7-Figure 3.15 shows the comparison of the results between the experimental, ZAERO and equivalent stiffness approaches. The results are compared for three velocities: 6.453 m/s, 10.3 m/s and 14.447 m/s. Figure 3.7-Figure 3.15 shows the one second interval of converged solutions. The ZAERO and experimental

results are directly taken from ZAERO Application Manual [44]. The results exhibit a precise concordance.

Figure 3.7-Figure 3.9 present the result of the 6.453 m/s. They show the time response comparisons of the flap angle, pitch angle and plunge displacement obtained by the equivalent stiffness methodology implemented in this study and experimental and ZAERO results. In Figure 3.7-Figure 3.9, it is seen that ZAERO analysis results based on the offset moment approach and the present solution based on the equivalent stiffness approach agree very well. At this velocity, periodic LCO is observed. This LCO is not a straightforward harmonic motion. The LCO differs from simple harmonic motion because it doesn't strictly adhere to the characteristics of a linear restoring force. As a result, it is categorized specifically as "periodic LCO." [44]. In this analysis, it is also discovered that to get an LCO behavior, the initial disturbance must be sufficiently high. Otherwise decaying oscillatory motion occurs. In this analysis, the required initial condition is calculated utilizing the work of Tang et al. [45]. The plunge mode is excited with a modal amplitude 0.2 in the present study. ZAERO uses 0.1 rad control surface rotation to trigger the LCO [44].

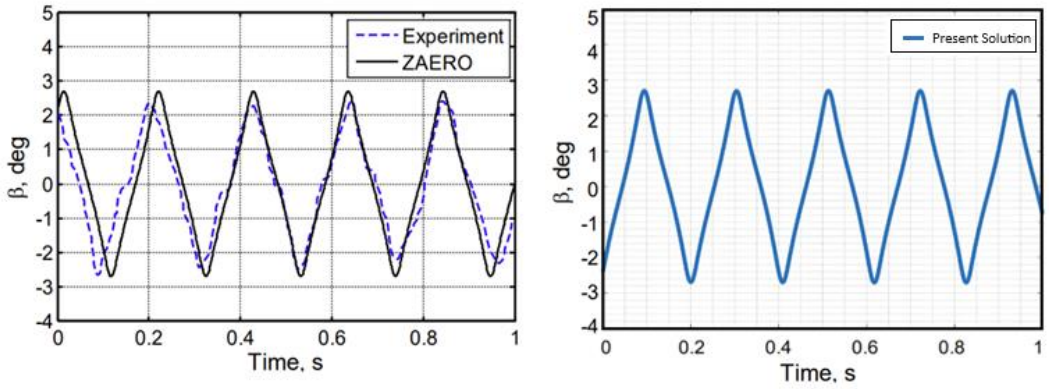

Figure 3.7. Flap Rotation Comparison for V=6.453 m/s

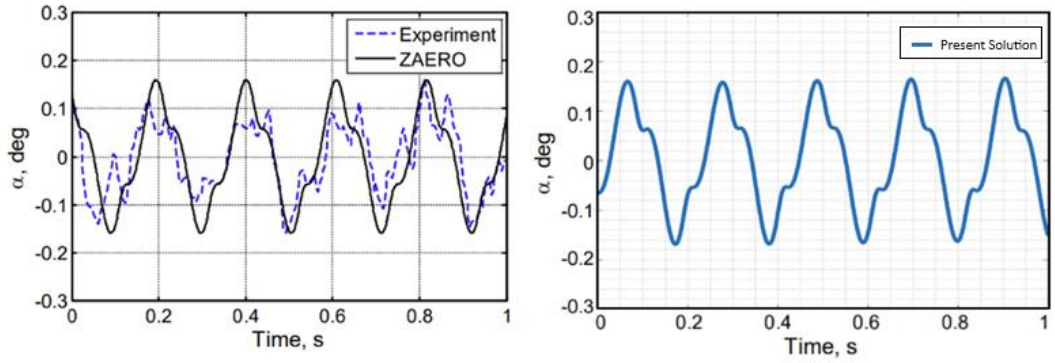

Figure 3.8. Pitch Angle Comparison for V=6.453 m/s

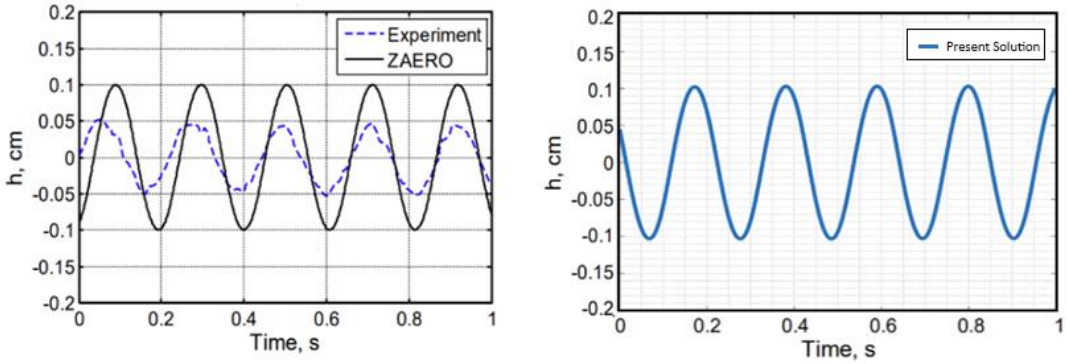

Figure 3.9. Plunge Comparison for V=6.453 m/s

For the 10.3 m/s velocity case, Figure 3.10-Figure 3.12 present the time response comparisons of the flap angle, pitch angle and plunge displacement obtained by the equivalent stiffness methodology implemented in this study and experimental and ZAERO results. In this case, LCO can be defined as "intermittent chaos" [44]. It is also discovered that the emergence of such an intermittent chaos is essentially independent from the initial disturbance; that is, the chaotic reaction may be initiated even by a minor initial disturbance. In this analysis, the plunge mode is excited with a modal amplitude of 0.2. ZAERO uses 0.1 rad control surface rotation to trigger the LCO [44].

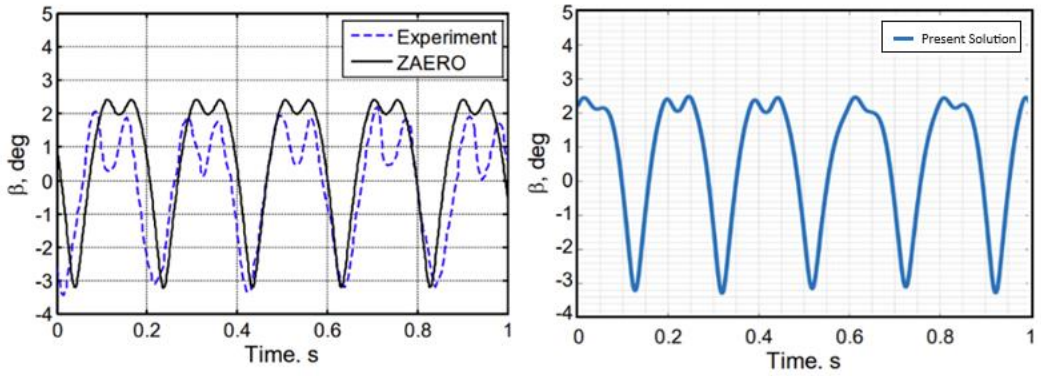

Figure 3.10. Flap Rotation Comparison for V=10.3 m/s

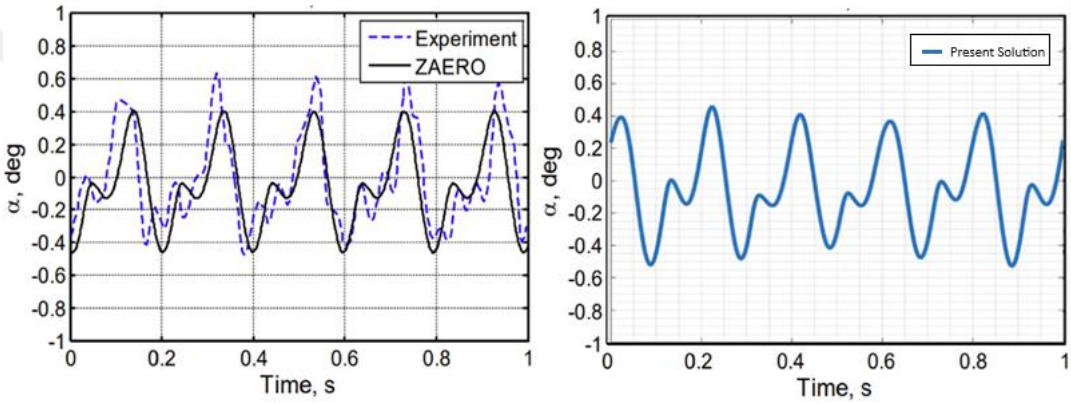

Figure 3.11. Pitch Angle Comparison for V=10.3 m/s

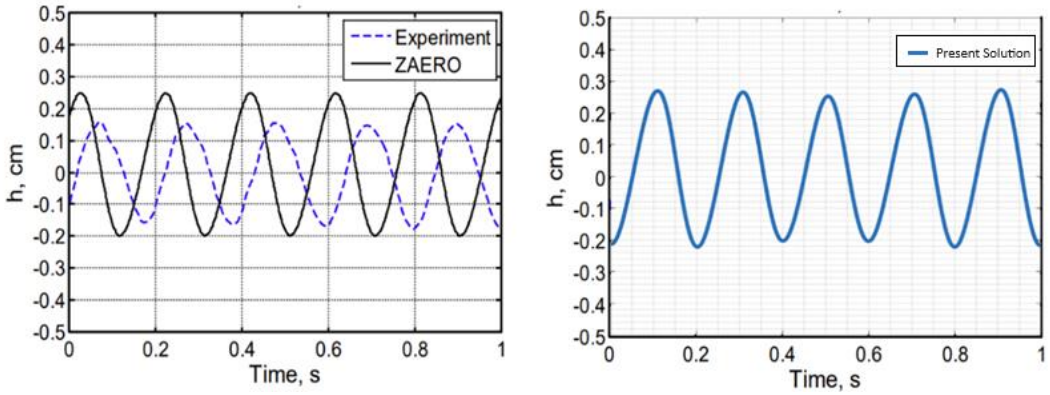

Figure 3.12. Plunge Comparison for V=10.3 m/s

For the 17.447 m/s velocity case, Figure 3.13-Figure 3.15 present the time response comparisons of the flap angle, pitch angle and plunge displacement obtained by the equivalent stiffness methodology implemented in this study and experimental and ZAERO results. The LCO behavior that is obtained at 17.447 m/s can be defined as a "nearly harmonic LCO", because the response has a dominant frequency, resulting in a nearly simple harmonic motion. In this analysis, the plunge mode is exited with a modal amplitude 0.2 in the present study. ZAERO uses 0.1 rad control surface rotation to trigger the LCO [44].

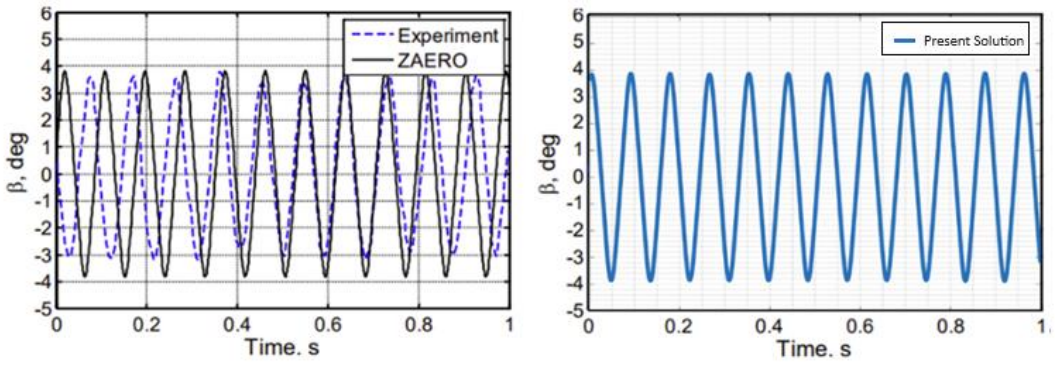

Figure 3.13. Flap Rotation Comparison for V=17.447 m/s

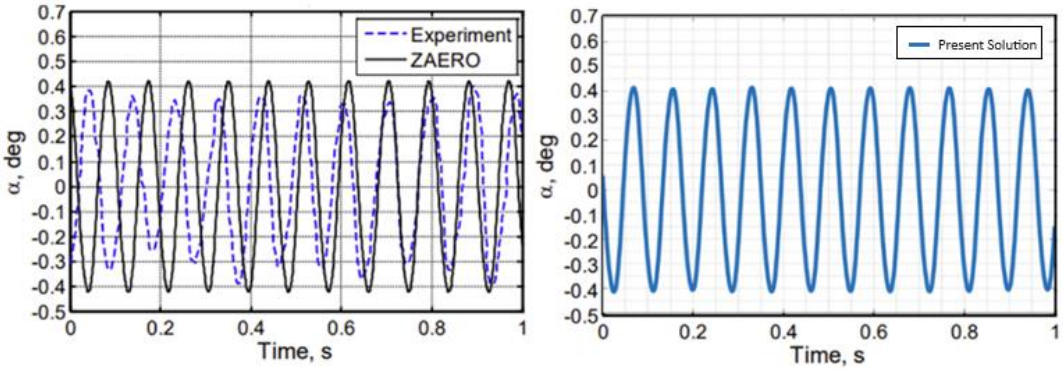

Figure 3.14. Pitch Angle Comparison for V=17.447 m/s

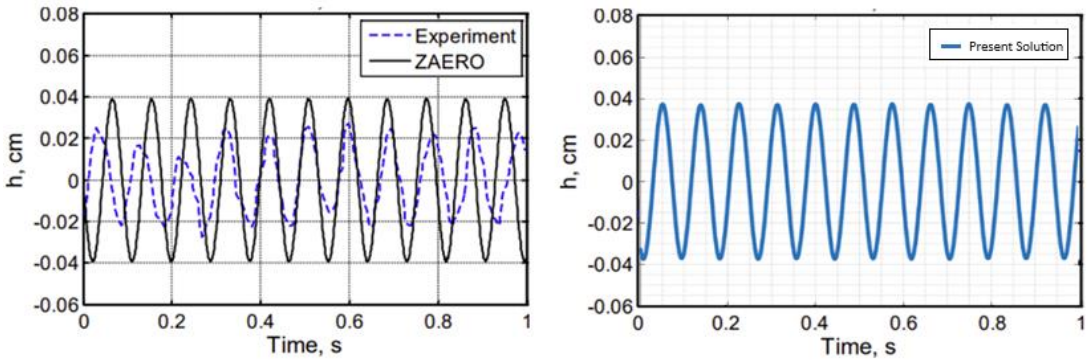

Figure 3.15. Plunge Comparison for V=17.447 m/s

3.2.2 AGARD 445.6 Case with Freeplay

In this study, the AGARD 445.6 wing model is employed. The model comprises a tapered swept wing with a NACA 65A004 airfoil section and a 45-degree sweep angle as seen in Figure 3.16 [46]. The wing's material properties are given in Table 3.1.

Table 3.1 AGARD 445.6 Wing Material Properties

Parameter	Definitions	Value
ρ	Density	381.98 [kg/m^3]
E_{xx}	Spanwise elastic modulus	3.15 x 10^9 [Pa]
E_{zz}	Chordwise elastic modulus	4.16 x 10^8 [Pa]
G_{XZ}	Shear modulus	4.39 x 10^8 [Pa]
v	Poisson's Ratio	0.31

The AGARD flutter experiment remains widely acknowledged in the literature as a key benchmark for validating aeroelastic frameworks. The AGARD 445.6 wing exhibits weak aerodynamic nonlinearity and a linear structure, leading to generally favorable correlation with experimental data through numerical aeroelastic frameworks [46].

For this study, modifications are made to the AGARD 445.6 wing to emulate an all-movable tail with a root connection supported by a torsional spring. Freeplay nonlinearities are introduced to validate the equivalent stiffness approach against ZAERO. The all-movable tail means that the tail can rotate around a pivot point which is located its root location. The root boundary conditions are removed, and grounded rotational spring is added and connected to the node which given in Figure 3.17 as the red circle. All spring DOFs are specified as 1e+9 [N/m] for the translational DOFs and 1e+9 [N.m/rad] for the rotational DOFs except for the pitching DOF of the bush element. The rotational stiffness of the pitching DOF is defined as 1e+3 [N.m/rad] [46].

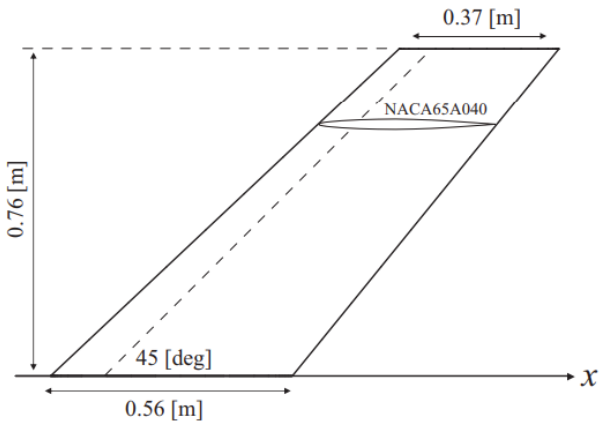

Figure 3.16. Wing dimension for the AGARD 445.6 Weakened Wing

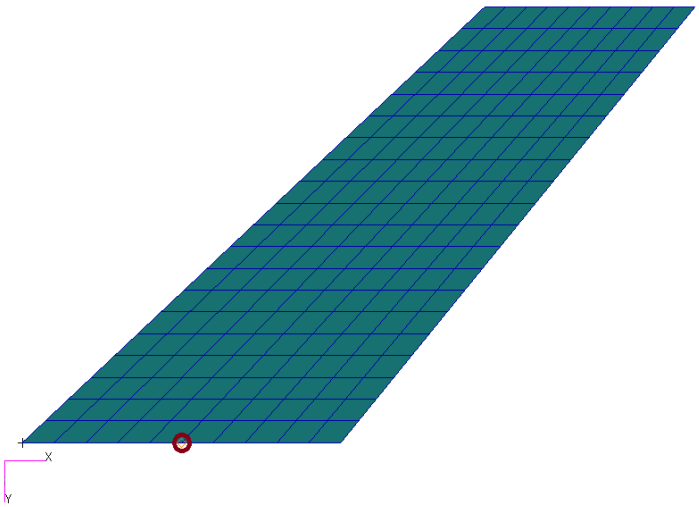

Figure 3.17. NASTRAN FEM of the AGARD 445.6 Weakened Wing with the Loosened Root Connection

The AGARD FEM model consists of 200 QUAD4 elements and 232 GRID points and one bush element is added to the root to transform from the original AGARD 455.6 wing to all movable tail. The total mass of the wing is 1.68 kg. After the model is converted to the all-movable tail, fictitious mass is added to the pitching DOF of the corresponding bush node seen in Figure 3.17 with a value of 1.4 x 10^5 [kg.m^2] moment of inertia around the hinge line by using the CONM1 card. After the addition of fictitious mass, the steps which are defined in Equation 2.1 to Equation 2.5 are followed to get fictitious mass eigenvectors. Then, the fictious mass eigenvectors are provided to ZAERO to get the GAFs at several reduced frequencies. GAFs are then converted into time domain by using the rational function approximation (RFA) which is explained in detail in section 4.2.1. The state-space matrix which is given in Equation 3.27 is used and the [$-[M_s]^{-1}[K_s]$] term appearing in the state-space equation, is updated in each time step by following the Equation 3.40 to Equation 3.47.

In addition to the equivalent stiffness methodology, AGARD 445.6 wing test case in ZAERO Application Manual [36] is used to perform the aeroelastic analysis with freeplay by using the nonlinear flutter analysis module (NLFLT) of ZAERO to

compare with the equivalent stiffness method. The AGARD test case units are Imperial units. Therefore, in ZAERO analysis, all structural model units are converted into Imperial Units. Moreover, in the analysis performed in ZAERO, ZAERO ZTRAN module is employed to capture the effects of the aerodynamic nonlinearities for the transonic Mach numbers.

ZAERO addresses a wide range of aeroelastic issues, including static aeroelastic/trim analysis and aeroservoelasticity. ZONA Technology INC. created it as a commercial program for aeroelastic analysis. The ZTRAN unit was developed by adding computational fluid dynamics data into the solution process. Flow effects that standard approaches cannot capture can therefore be accomplished by ZTRAN. ZTRAN [36] solves the time linearized transonic small distortion integral problem using an upper field panel approach. This integral equation is divided into two parts. These components are a surface integral equation, which can be solved using panel techniques like ZONA6 and ZONA7, and a volume integral equation, which can be solved by modeling the flow field using volume cells encircling the surface. Examples of volume and surface modelling for the AGARD 445.6 test case [37] to use in ZTRAN module are in Figure 3.18. In addition to this, the Cp distribution comparison is shown in Figure 3.19.

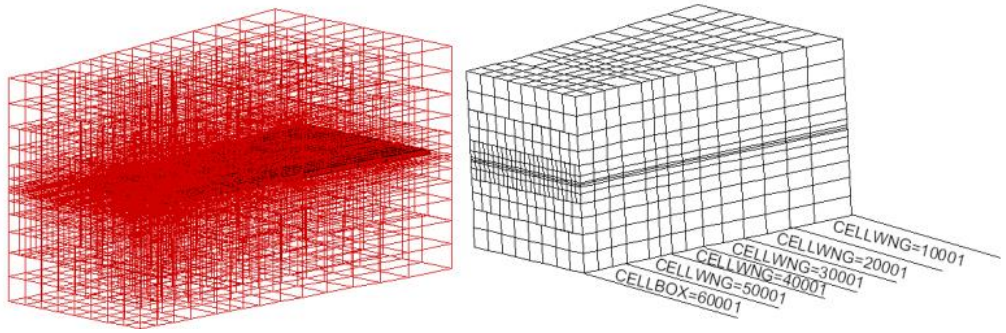

(a) (b)

Figure 3.18. ZTRAN model for the AGARD 445.6 Wing: (a) Surface-Box, (b) Volume-Cell Models [37]

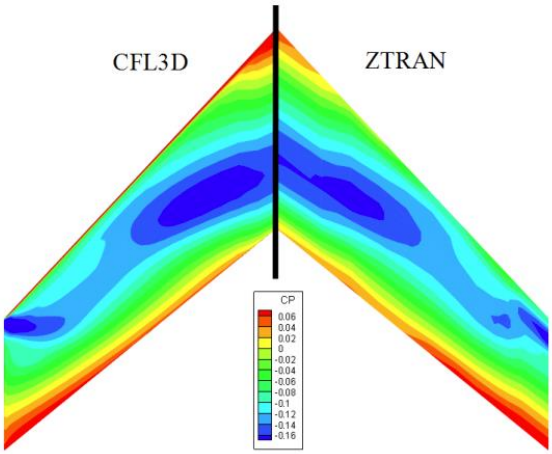

Figure 3.19. The Comparison of Interpolated Steady Cp Distribution of ZTRAN Aerodynamic Panel and Cp Distribution of CFL3D at M=0.954 [37]

The source term in the volume integral includes the so-called constant background flow solution, which is provided externally by other high-accuracy computational fluid dynamics codes such as the Navier-Stokes solver. ZTRAN then combines the effect coefficients calculated from the surface and volume integral equations to form an aerodynamic effect coefficient matrix of the same form, calculated by linear panel methods such as ZONA6 and ZONA7.

The modal analysis is performed for nominal structural model by using NASTRAN and the first 4 mode shapes of the nominal structure are shown in Table 3.2. Dark Blue colors refer to undeformed shapes and red ones refer to the mode shapes of all movable AGARD 445. The nominal means the structural model without freeplay.

Table 3.2 Nominal Mode Shapes of the All Movable AGARD 445.6

Mode 1 [Bending-Rotation Mode: 6.63 Hz]	Mode 2 [Wing Tip Bending-Rotation Mode: 34.91 Hz]
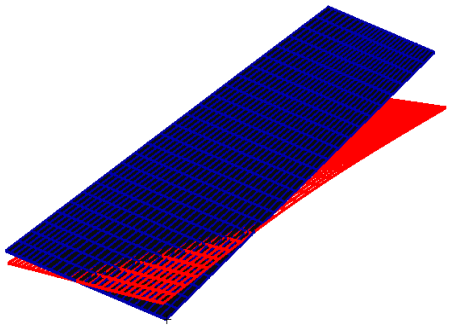	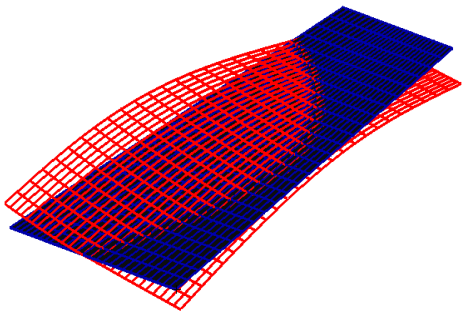
Mode 3 [Torsion Mode:38.90 Hz]	Mode 4 [Second Torsion-Rotation Mode: 84.76 Hz]
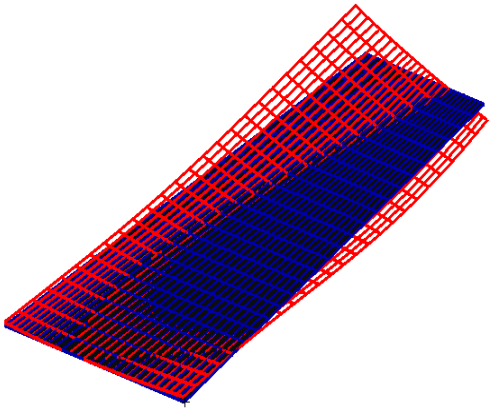	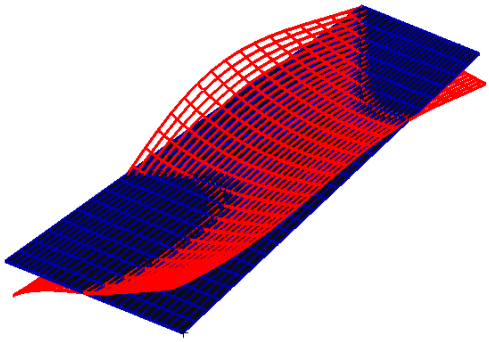

The fictitious mass method should be implemented to AGARD all movable tail case. Because the stiffness change on the root connection is affecting the structural mode shapes and frequencies. To capture these effects, Fictitious Mass is applied to the corresponding rotational DOF at the root connection seen in Figure 3.17. Table 3.3 gives the natural frequencies of all moveable AGARD 445.6 wing obtained by the

direct method and the fictitious mass method. The direct method means the results of modal analysis which are performed without using FM in the MSC NASTRAN. In this case, structure is called nominal structure, and the results of the modal analysis are directly obtained from MSC NASTRAN. Table 3.3 shows the comparison between the direct and the FM approach results for the nominal and the free structural model. Free structural model refers to the model with the rotational stiffness of the grounded bush at root being zero.

Table 3.3 Frequency of the All Movable AGARD 445.6 Wing

	Direct Approach [Hz]		FM Approach [Hz]	
Mode	Nominal	Free	Nominal	Free
1	6.63	0.00	6.63	0.00
2	34.91	28.68	34.91	28.69
3	38.90	38.89	38.90	38.89
4	84.76	77.99	84.76	78.01

3.2.2.1 Freeplay Analysis Results of the All Movable AGARD 445.6

The aeroelastic system which includes freeplay is analyzed by using all movable AGARD 445.6 model. For this purpose, ±0.5° freeplay is assumed and nonlinear transient analysis of the aeroelastic system is performed for two Mach numbers;0.678 and 0.95 Mach. The analysis is performed by using the state-space equation which is given in Equation 3.27. GAFs for several reduced frequencies are obtained from ZAERO by providing the fictious mass eigenvectors. Then, GAFs are converted into time domain by using the rational function approximation (RFA) which is explained in section 4.2.1. The state-space matrix which is given in Equation 3.27 is constructed and the $[\ -[M_s]^{-1}[K_s]]$ term appearing in the state-space equation is updated at each time step by following Equations 3.40-3.47. The

initial 4.0° rotation is given to the aeroelastic model for both ZAERO and present analysis. In ZAERO, this is made by providing a pilot input command. In the present study, the modal displacement value for the first mode of the aeroelastic system, which is the rotational mode, is used to give 4.0° rotation initial condition. Solutions are presented following the convergence for a duration of 0.5 seconds.

First, the analysis performed on Mach 0.678 for ±0.5° freeplay. In this case, the analysis conditions are shown in Table 3.4. The nonlinear transient analysis is performed at the same conditions in ZAERO NLFLT. Then, ZAERO results are compared with the results of the equivalent stiffness methodology. Note that, there is no flow nonlinearity such as shock at Mach 0.678 [37]. Rotation angle histories of the root connection are shown in Figure 3.20. Reasonably good correlation exists between the ZAERO results and the equivalent stiffness methodology in terms of the LCO amplitude. A possible reason for the amplitude differences could be numerical methods that are used to solve the state-space equations for both ZAERO and present results. ZAERO uses fixed time step and there is no definitive information whether the exact switching points are checked or not. This may cause a numerical difference.

Table 3.4 Analysis Conditions

Mach	*0.678*
Density	*0.15 kg/m^3*
Freeplay angle	*0.5^o*
Velocity	*231.3 m/s*
Initial Condition	*4.0^o Root Rotation*

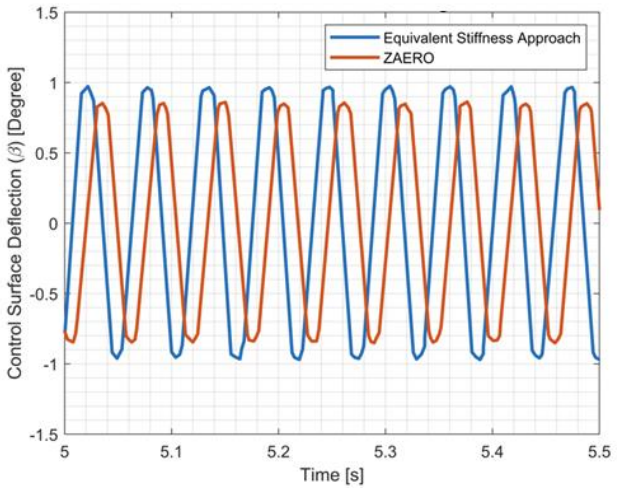

Figure 3.20. Rotation Angle History of the Root Connection at Mach=0.678

The final analysis performed on Mach 0.954 for ±0.5° freeplay. In this case, analysis conditions are shown in Table 3.5. Nonlinear transient aeroelastic analysis results obtained with ZAERO, and the present equivalent stiffness approach are compared in Figure 3.21. It should be noted that Mach 0.954 is an aerodynamically nonlinear Mach number in terms of shock. The steady Cp distribution of Mach 0.954 is given in Figure 3.19. As Figure 3.21 shows, again, except for the offset in time, rotation angle histories of the root connection obtained by ZAERO, and the present approach are in good agreement in terms of the LCO amplitude and general behavior.

Table 3.5 Analysis Conditions

Mach	*0.954*
Density	*0.037 kg/m^3*
Freeplay angle	*0.5* ^{o}
Velocity	*307.2 m/s*
Initial Condition	*4.0* ^{o} *Root Rotation*

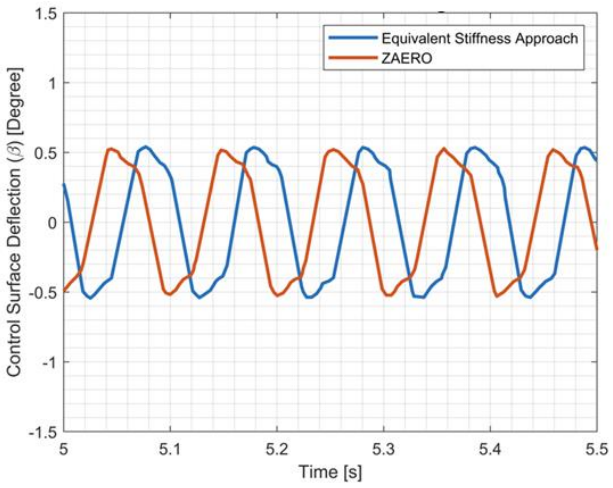

Figure 3.21. Rotation Angle History of the Root Connection at Mach=0.954

CHAPTER 4

AEROELASTIC MODELING AND ANALYSIS OF THE VLA

This chapter presents the generation of the structural modeling of the METU VLA aircraft. MSC Nastran and Patran are used to model the aircraft. To take the control surfaces into account, two different models are investigated in this chapter. These models are the actuator implemented GFEM model and the "Bush" implemented GFEM model of VLA. The methodology is defined to develop the concentrated stiffness model (bush model) from the actuator implemented model. Validation of the dynamic characteristics of the two models is performed. After the models are created, MSC Nastran SOL103 is used to obtain the eigen vectors and the eigen values of the structures, which characterize the dynamic behavior of the structural models. A fictitious mass approach is implemented to use the models with freeplay in the nonlinear analysis. In the fictitious mass approach, huge inertia is added to the areas in which stiffness changes occur. The verification process is performed after the eigenvectors and eigenvalues of the fictitious mass-implemented structures are obtained.

The generation of the aerodynamic model of the METU VLA in MSC Nastran is then studied. A brief summary of the Doublet Lattice Method (DLM) is given. The procedure which should be followed while the aerodynamic model is created is listed, and the aerodynamic model is created for the METU VLA aircraft. Rational Function Approximation is needed for time domain analysis to convert the frequency domain aerodynamic data to the time domain. After the conversion of data, the verification study is presented.

Finally, the generation of the aeroelastic model is covered. The aeroelastic model requires coupling between the structural model and the aerodynamic model. Splines are created for this purpose. Selected spline grids on the corresponding aero panels

are shown. The created splines are verified by using the MSC Patran FLDS module. After the aeroelastic model is created, linear flutter analysis is performed for nominal and zero rotational stiffness cases. The results are shown in the envelope.

4.1 Structural Modelling of the Very Light Aircraft

In this thesis, METU VLA structural global finite element model (GFEM) has been used. It is a computational model that uses the finite element method (FEM) to depict the global behavior of a structure. GFEM is a numerical approach used in structural analysis to study and forecast the behavior of complex structures subjected to diverse loads and boundary conditions.

By discretizing the structure into finite elements, the GFEM technique enables the modeling of complicated geometries and complex material behavior. A collection of nodes represents each element, and the connections between them are constructed using shape functions and interpolation techniques. GFEM is widely utilized in engineering domains such as civil, mechanical, aerospace, and structural. It is a robust tool for modeling and comprehending structure responses to various stress circumstances. The GFEM analysis' accuracy is determined by parameters such as mesh density, element type, and material modeling methodologies employed. The METU VLA GFEM model is shown in Figure 4.1.

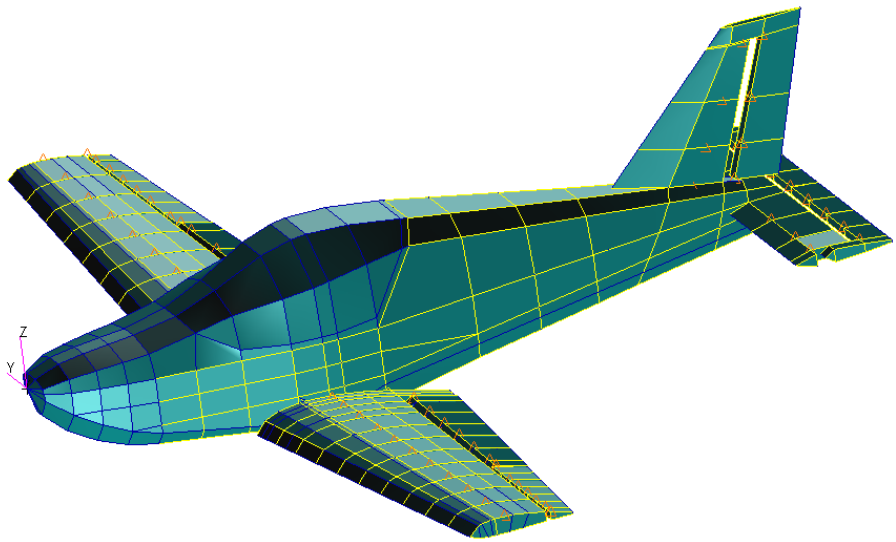

Figure 4.1. METU VLA GFEM Model

The nose of the aircraft is located at [0,0,0] coordinate. The reference coordinate system is defined in Figure 4.1 METU VLA GFEM Model. The model consists of eight primary components. These are the fuselage, wing, horizontal tail, vertical stabilizer, aileron, flap, elevator, and rudder.

METU VLA GFEM is generated in MSC PATRAN. Some approaches are used to represent the actual structure in the FEM model. For example, elements intended to carry only axial loads are modeled as pure axial load carrying rod elements (CROD in Nastran), and elements intended to carry transverse shear forces, bending moments, and the loads associated with cross-sectional warping are modeled as beam elements (CBAR/CBEAM in Nastran). Skin elements in the structure are modeled as shell elements (QUAD4 or TRIA in Nastran). These types of elements are responsible for carrying internal forces such as in-plane force, moments, and shear forces. Spring elements are used to connect different parts or components. These are modeled as CBUSH or CELAS elements in NASTRAN. The differences between CBUSH and CELAS elements is that CELAS is used to define one DOF spring in model. It means that if the stiffness on each DOF is desired to be defined, it requires 6 CELAS element. However, this can be defined by using just one CBUSH element.

In the METU VLA GFEM model, stringers, flanges, and longerons are modeled as rod (CROD), whereas triangular or quadrilateral shell elements represent spar webs, ribs, and skin structures. In addition to this, wings are connected to fuselage with RBE2 element.

The mass of GFEM is modeled as a lump mass model. This model adds and combines mass components to depict a system's scattered mass as a single point. In some cases, the lump mass model is favored. Detailed modeling of the total mass can be time-consuming and challenging in examining the large and complicated structures. The lump mass model may be used to simplify the structure and shorten the analysis time. In addition, density-based FEM models can cause local natural modes. In Nastran, lump masses are modeled as CONM2 elements. Initially, GFEM is generated using a density-based mass model in this study. Then, the mass properties tool in the MSC Patran program is used to transform the density-based mass model into a lumped-based mass model. This tool aids in determining the chosen area's center of gravity (CG) and mass moment of inertia. Lumped masses are created by combining CONM2 cards with mass and CG values computed using the MSC Patran mass properties tool. RBE3 elements are used for distribution purposes. RBE3 is an element used for stiffness or load transmission in Nastran. The RBE3 element is linked to main points; can be linked to one or more number of ports. These interfaces are used to transfer stiffness or mass from other parts. In a finite element model, it is usually used to describe rigid connections between numerous nodes. It should be noted that RBE3 elements do not adding an extra stiffness to the structure. On the other hand, the RBE2 element transfers displacements, rotations, and forces between linked nodes, thereby treating them as a single rigid body. In contrast to RBE3, RBE2 makes the nodes where it is connected to infinitely stiffen. Therefore, caution is required when using it. Using RBE3 elements, these resulting lumped masses are then distributed to the hard points of the relevant region, such as the rib-spar connection and frames. The RBE3 elements are connected to independent nodes which refer to the nodes which are in the area where the mass is distributed, and lump masses are attached to the dependent center node. Mass model

used in the GFEM is shown in Figure 4.2 and an example of lump mass distribution with the use of RBE3 Element is shown in Figure 4.3. In Figure 4.3, brown circles show the selected independent nodes for RBE3 connections. The hinges are not modelled in VLA GFEM. Therefore, the hinges are assumed to be rigid in this analysis. The hinges in the GFEM model are modeled using RBE2 elements. The total FEM elements used in GFEM are shown in Table 4.1.

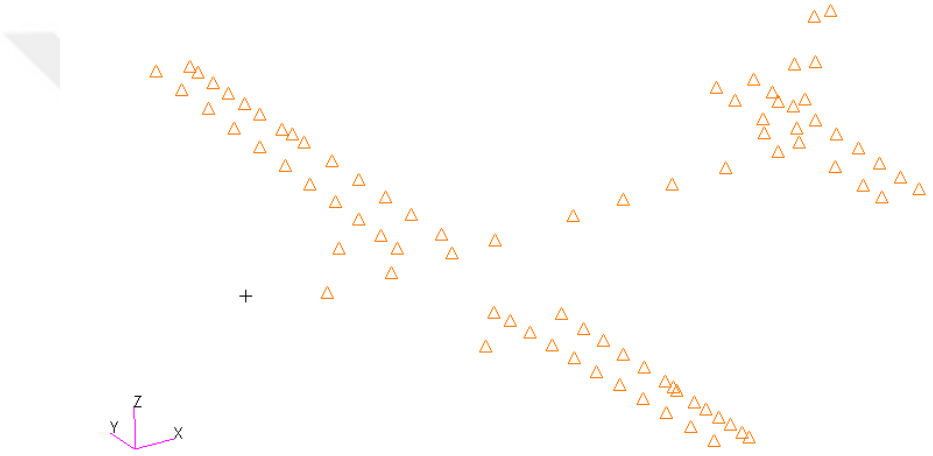

Figure 4.2. Mass Model of the VLA in the GFEM

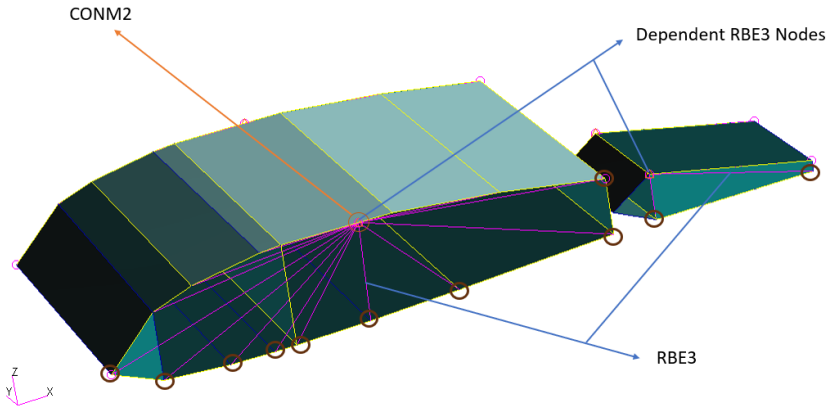

Figure 4.3. Lump Mass Distribution with the use of RBE3 Element

Table 4.1 Elements Used in the GFEM

Element Type	Element Name in MSC Nastran	Element Description	Number of Elements
1-D Bar	CBAR	Simple Beam Element	40
1-D Bar	CBEAM	Beam Element	32
0-D Bar	CBUSH	Spring/Damper Element	13
0-D Bar	CELAS1	Scalar Spring Element	12
0-D Mass	CONM2	Concentrated Mass Element	86
1-D Rigid	RBE3	Interpolation Constraint Element	96
2-D Shell	CQUAD4	Quadrilateral Plate Element	1502
1-D Bar	CROD	Rod Element	1399
2-D Shell	CTRIA3	Triangular Plate Element	90
1-D Rigid	RBE2	Rigid Link Element	140

4.1.1 Connections of Control Surfaces

In aeroelastic analysis, total rotational stiffness around the hinge line refers to the stiffness of the control system that determines the reaction of a control surface to aerodynamic forces. Total rotational stiffness affects the flutter characteristics of an aircraft such as flutter speed and mode shapes. A higher rotational stiffness increases the flutter speed, making the aircraft less prone to flutter, whereas a lower stiffness might result in lower flutter speeds and increased flutter vulnerability.

The structural features of the control surface, such as material stiffness, geometry and actuator properties must be considered when designing the suitable rotational

stiffness. To get the ideal stiffness, rigorous study and design adjustments are required.

The total rotational stiffness of a control surface depends on the control surface attachments. If the aileron is considered as an example, it is attached to the wing with hinges. In the actual design, the movement of the aileron is controlled by an actuator or the stick base flight control system. This actuator is also attached to a specific area of the wing and with the rod attachments to the aileron itself. Representative modelling of the aileron is given in Figure 4.4. The model shown in Figure 4.4 can be presented with a spring analogy. For this purpose, the system is considered as three serially connected linear springs representing “actuator stiffness”, “stiffness of the wing backup structure” and “stiffness of the aileron backup structure”. These definitions are shown in Figure 4.5 and Figure 4.6. The spring modelling of the control surface actuation system is given in Figure 4.7. The stiffness of all parts of the system is considered as linear springs. Therefore, the lines shown in Figure 4.7 are presented as infinitely stiff representation of the control surface and the main surface. The springs are serially connected. Therefore, total rotational stiffness around the hinge line can be found from Equation 4.1. It should be noted that the total rotational stiffness, or the control loop stiffness, should have the unit of N.mm/rad. Therefore, before using Equation 4.1, the linear springs should be converted into rotational ones around the hinge line. The example calculation of the conversion of a linear spring to a rotational spring can be formulated by using Figure 4.8. The linear spring is connected to the aileron at a distance “r”. This spring represents the linear stiffness of the actuator. The moment around the hinge line is given as “M”. The linear spring constant is “k”. The stretch on the linear spring can be calculated as $r \cdot \theta$ with the small angle assumption. Therefore, the moment equilibrium equation around the hinge line can be written as given in Equation 4.2. The main aim is to find an equivalent rotational spring for the linear one. Therefore, the moment can be assumed as $k_{equivalent\ rotational} \cdot \theta$. After substituting the given moment term into Equation 4.2, the equivalent rotational spring can be found as given in Equations 4.3 and 4.4.

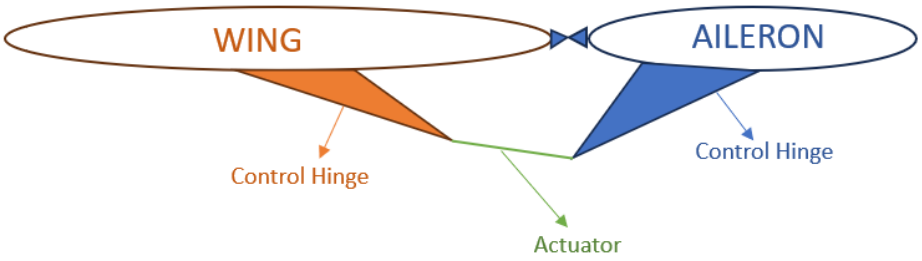

Figure 4.4. Aileron-Wing Representative Modelling

Figure 4.5. Wing Back-up Structure Modelling

Figure 4.6. Aileron Back-up Structure Modelling

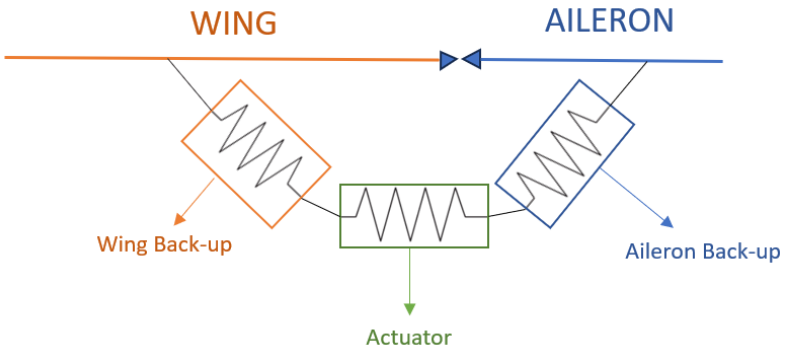

Figure 4.7. Spring Modelling of the Control Surface Actuation System

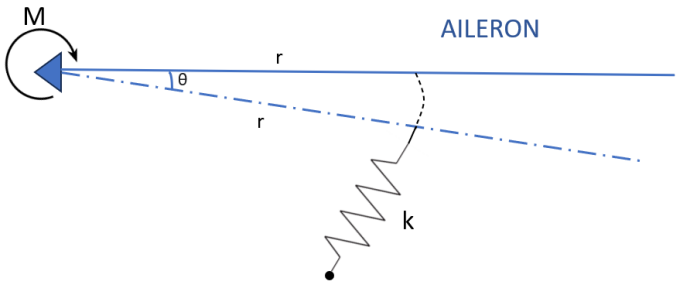

Figure 4.8. Linear to Rotational Spring Calculation Model

$$\frac{1}{CL\ Stiffness\ of\ the\ Aileron} = \frac{1}{Actuator\ Stiffness} + \frac{1}{\substack{Stiffness\ of\ the\ Wing \\ Backup\ Structure}} + \frac{1}{\substack{Stiffness\ of\ the\ Aileron \\ Backup\ Structure}} \tag{4.1}$$

$$k * r * \theta * r = M \tag{4.2}$$

$$k * r * \theta * r = k_{equivalent\ rotational} * \theta \tag{4.3}$$

$$k * r^2 = k_{equivalent\ rotational} \tag{4.4}$$

Usually, the control surface back-up stiffness affects this equation very slightly, but it should be considered. Since the structural model of VLA is not fully mature during the design phase, the GFEM taken from the VLA structural team does not include a control surface actuation system. As a first step of preparation of the GFEM model for aeroelastic analysis, representative actuator systems are modeled in the finite

element model as rod elements using CROD element in Nastran. In this case, the stiffness of the actuator in terms of the rotational effect around the hinge line can be calculated by using Equation 4.5,

$$K_{rod} = \frac{EA}{L} r^2 \tag{4.5}$$

where $\frac{EA}{L}$ is the linear stiffness of the actuator (k in Equations 4.2-4.4) and "r" is the perpendicular distance to the hinge line. E, A and L are the elastic modulus, area of the rod element and length of the rod element, respectively.

In addition to this, the hinges are not modelled in VLA GFEM. Therefore, the hinges are assumed to be rigid in this analysis. The hinges in the GFEM model are modeled using RBE2 elements as shown in Figure 4.10 for the aileron-wing actuator modeling. All actuators are modeled with ROD elements and their axis with hinge axis are arranged to be 90^o. Then, the actuator is connected to the main surface with RBE2 elements at hard points such as the spar-rib intersection in the wing. The control surface actuator modeling for the aileron, elevator and the rudder are given in Figure 4.10-Figure 4.12, respectively. It should be noted that for flutter analysis, flap is assumed as locked. It means that the actuator system implementation or total stiffness calculation around the hinge line study is not performed. The modelling of the flap flight control system implementation is given in Figure 4.9. In this model, the total rotational stiffness around the hinge line is given to the CBUSH of the root hinge. The value of the rotational stiffness is assumed as 1000 times of the aileron control loop stiffness, and this value is directly given to the rotational stiffness of the bush element. Therefore, an actuator model is not used for the flap. It should be noted that actuator stiffness values of the control surfaces are given such that these values do not cause flutter in the envelope.

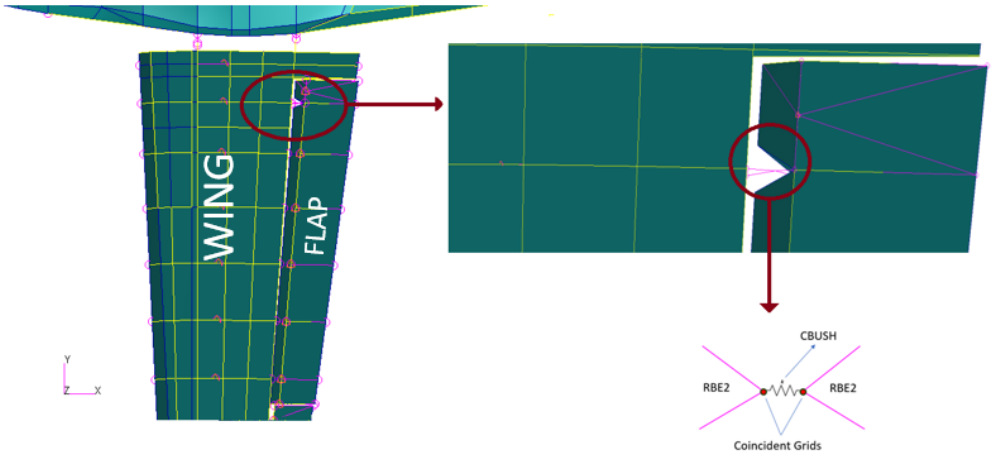

Figure 4.9. Modelling of the Flap FCS Implementation

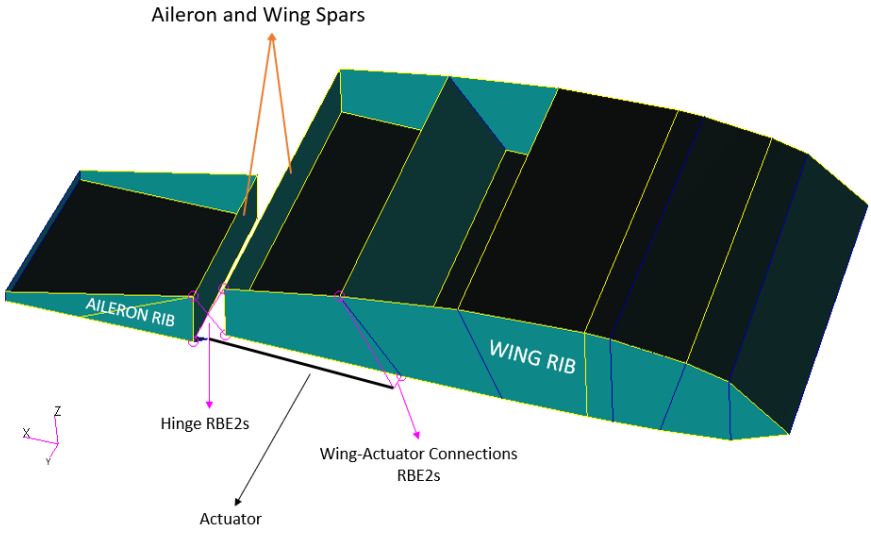

Figure 4.10. Aileron-Wing Actuator Modelling

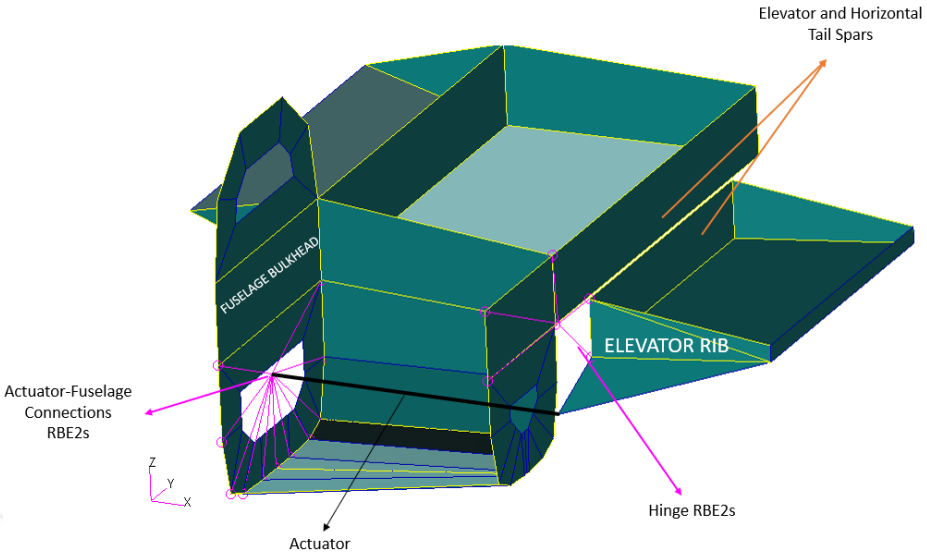

Figure 4.11. Elevator-Fuselage Actuator Modelling

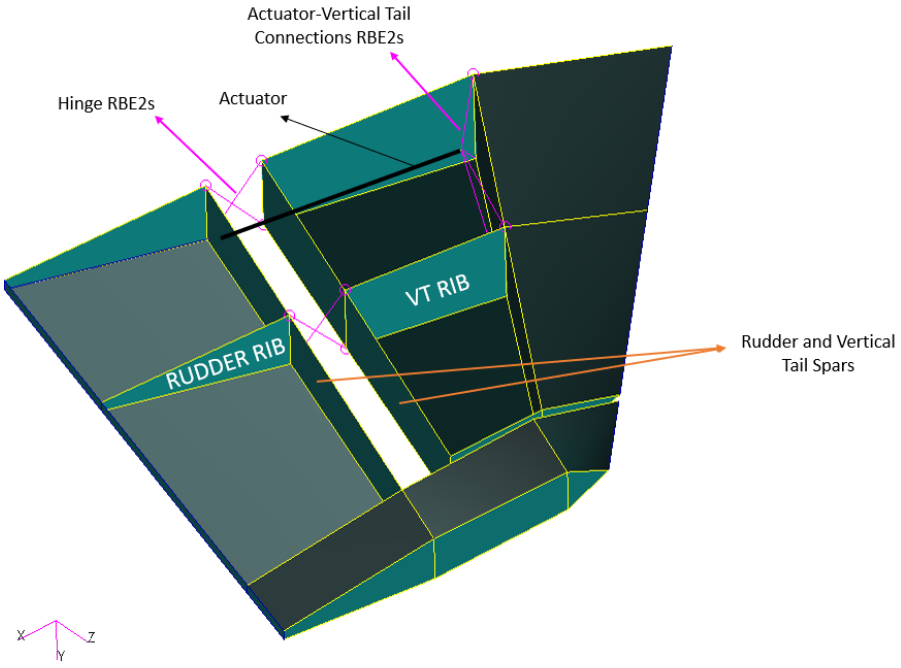

Figure 4.12. Rudder-VT Actuator Modelling

4.1.2 Calculations of Total Rotational Stiffness' of the Control Surfaces Around the Hinge Line

As explained previously, "Total Rotational Stiffness" is the rigidity of the control system that determines the reaction of a control surface to aerodynamic forces in the context of aeroelastic analysis. For each control surface, total rotational stiffness' are calculated. In this section, aileron total rotational stiffness calculations are shown as an example. The model used for the aileron rotational stiffness calculation is given in Figure 4.13. The wing is clamped from its wing-fuselage connection points for calculations. A unit force is applied to the control surface. Then, a static analysis performed and the displacement in the direction perpendicular to the hinge line is determined at specific grid points on both the aileron rib and the wing rib. Since the distance between selected grid points is known, rotation angle can be calculated by using the displacement difference. For the aileron, the selected grid points from the hard points are shown in Figure 4.14. Figure 4.15 shows the displacement result at the selected grid points for the aileron control loop stiffness calculation. The 0.01 Newton force in the direction perpendicular to the hinge line is applied to the aileron. The hinge moment which is created by the applied force is calculated by multiplying the applied force with the perpendicular distance to hinge line. For the aileron example, the resulting moment around the hinge line becomes 1.7 N.mm.

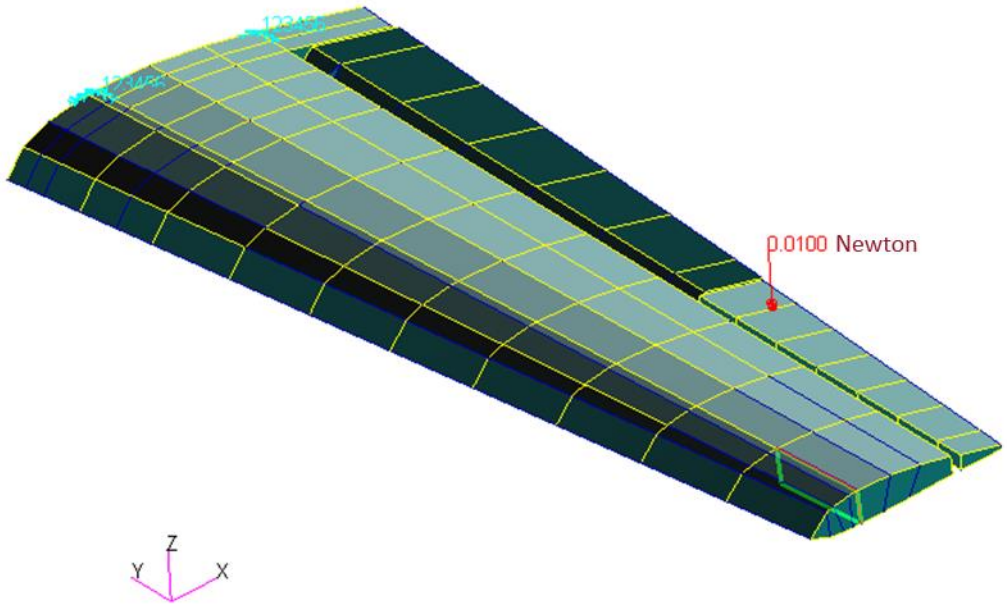

Figure 4.13. Aileron Control Loop Stiffness Model

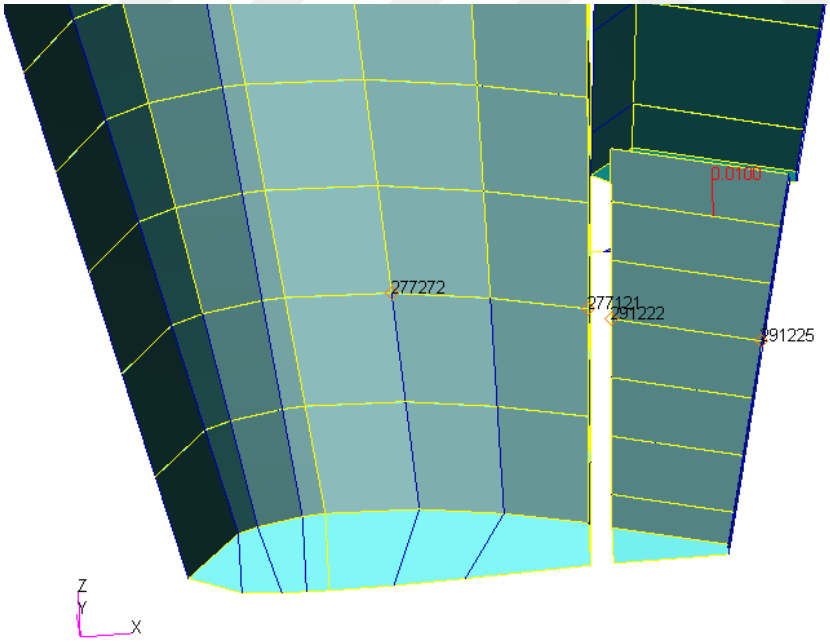

Figure 4.14. Selected Grid Points for the Aileron Control Loop Stiffness Calculation

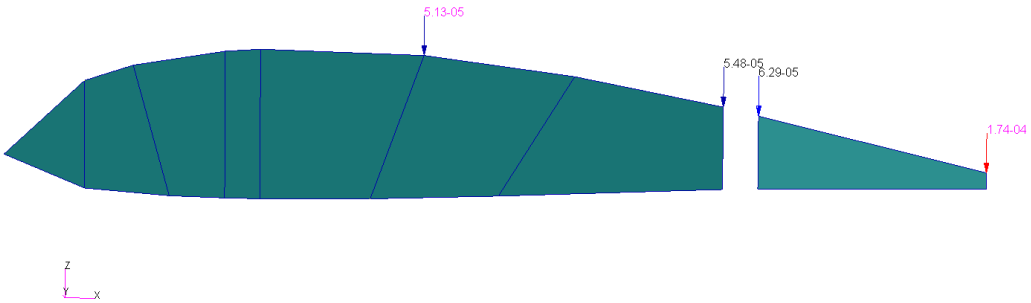

Figure 4.15. The Displacements for the Selected Grids on the Aileron and the Wing Rib

Then, the rotation angle is calculated as,

$$\tan\left(\begin{matrix}Rotation\ angle\ on\\ the\ Wing\ Side\end{matrix}\right) = \frac{Displacement_{Grid\ 1} - Displacement_{Grid\ 2}}{Distance\ Between\ Grids\ 1\ and\ 2} \quad (4.6)$$

where Grid 1 in Equation 4.6 corresponds to grid 277121 and Grid 2 corresponds to grid 277272 in Figure 4.14.

In the aileron total rotational stiffness calculation case, distance between the selected grids on the wing (Grid-1 and Grid-2) is 297 mm. Using Equation 4.6, rotation angle on the wing side is calculated as $1.20\text{x}10^{-8}$ degrees. The rotation of the aileron side can also be calculated in the same manner. In this case, Grid 1 in Eqn. 4.6 corresponds to grid 291225 and Grid 2 corresponds to grid 291222 in Figure 4.14. The distance between the selected grids (Grid-1 and Grid-2) is 226 mm. Then, the rotation angle on the aileron side becomes $4.91\text{x}10^{-7}$ degrees. The actual control surface rotation is calculated by subtracting the wing surface rotation from the aileron rotation. The reason is that when the wing is twisted after applying a force to the aileron, this twist creates a rotation on the control surface. However, this rotation is a rigid body rotation. Therefore, it will not strain the control surface. Hence, for the aileron case the actual aileron rotation becomes $4.79\text{x}10^{-7}$ degrees. Finally, the total rotational stiffness of the aileron is calculated as,

$$\begin{matrix}Total\ Rotational\ Stiffness\\ of\ the\ Aileron\end{matrix} = \frac{Applied\ Moment\ Around\ the\ Hinge\ Line}{The\ real\ aileron\ rotation} \quad (4.7)$$

The total rotational stiffness of the aileron is then calculated as 3.55×10^6 N.mm/rad.

In the following, actuator stiffness is calculated. The actuator length is 258.77 mm for the aileron. The distance between the aileron actuator and hinge line is 44 mm. Also, the elastic modulus of the actuator is 65500 N/mm^2. The rotational stiffness of the actuator modeled as rod element is calculated by using Equation 4.5.

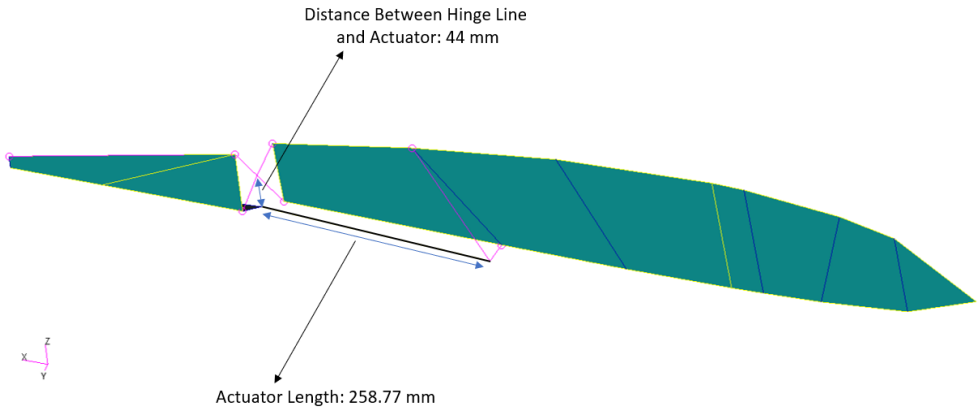

Figure 4.16. Distance and Length Definition for Aileron Actuator

The area of the actuator rod is taken as 500 mm^2 for the calculation of the actuator stiffness. In that case, actuator rod stiffness becomes 2.45×10^8 N.mm/rad. In Equation 4.1, the actuator stiffness, and the total rotational stiffness of the aileron (control loop stiffness) are known values now, and the wing back-up stiffness and the aileron back-up stiffness are the two unknowns. If same analysis is performed by increasing the elastic and shear modulus of all control surface elements several times such as 10 times, and the total rotational stiffness is calculated for the new model, two equations and two unknowns will be obtained as shown in Equations 4.8 and 4.9. It should be noted that when elastic modulus and shear modulus are increased 10 times, poison ratio is not changing.

$$\frac{1}{\begin{matrix}Total\ Rotational\ \ Stiffness \\ for\ Original\ Aileron\end{matrix}} - \frac{1}{Actuator\ Stiffness} = \frac{1}{Wing\ Backup\ Stiffness} + \frac{1}{Aileron\ Backup\ Stiffness} \tag{4.8}$$

$$\frac{1}{Total\ Rotational\ \ Stiffness\ for\ 10x\ Aileron} - \frac{1}{Actuator\ Stiffness} = \frac{1}{Wing\ Backup\ Stiffness} + \frac{1}{10xAileron\ Backup\ Stiffness} \quad (4.9)$$

If Equation 4.9 is subtracted from Equation 4.8, aileron back-up stiffness can be found. In addition to this, wing back-up stiffness can be determined after the calculation of the aileron back-up stiffness. The calculation results are shown in Table 4.2.

Table 4.2 Aileron Control Loop Stiffness Calculations (Actuator cross-sectional area=500 mm^2)

Aileron Stiffness	Actuator Stiffness [N.mm/rad]	Rotation of the Wing [Degree]	Rotation of the Aileron [Degree]	Real Aileron Rotation [Degree]	Control Loop Stiffness [N.mm/rad]
Original	2.45E+08	1.20E-08	4.91E-07	4.79E-07	3.55E+06
10xOriginal	2.45E+08	1.20E-08	4.71E-07	4.59E-07	3.70E+06

The aileron back-up stiffness' and wing backup stiffness' can be calculated by using Equation 4.8 and 4.9 resulting in an aileron back-up stiffness and a wing back-up stiffness of $7.74x10^7$ N.mm/rad and $3.78x10^6$ N.mm/rad, respectively. After the stiffnesses are calculated, a validation study is needed. The validation can be done by performing the same analysis with different actuator stiffness. If there is no any other term which affects the control loop stiffness, the wing back-up and the aileron back-up stiffnesses should be consistent. Therefore, the same analysis is performed for an actuator area of 5 mm^2. The calculation results for an actuator cross-sectional area of 5 mm^2 is shown in Table 4.3.

Table 4.3 Aileron Control Loop Stiffness Validation Calculations (Actuator cross-sectional area=5 mm^2)

Aileron Stiffness	Actuator Stiffness [N.mm/rad]	Rotation on The Wing [Degree]	Rotation on the Aileron [Degree]	Real Aileron Rotation [Degree]	Control Loop Stiffness [N.mm/rad]
Original	2.45E+06	1.20E-08	1.18E-06	1.17E-06	1.46E+06
10xOriginal	2.45E+06	1.20E-08	1.16E-06	1.15E-06	1.48E+06

Again, by using Equation 4.8 and 4.9, the aileron back-up stiffness and wing back-up stiffness can be calculated. The calculated values for the aileron back-up stiffness and the wing backup stiffnesses are $7.74x10^7$ N.mm/rad and $3.78x10^6$ N.mm/rad, respectively. Results match perfectly. The total rotational stiffness can then be calculated for any actuator stiffness by using Equation 4.1. Same calculation procedure is followed for the rudder and the elevator. Table 4.4 and Table 4.5 shows the total rotational stiffness calculation results of the rudder and the elevator, respectively.

Table 4.4 Rudder Back-up, VT Back-up, and Total Rotational Stiffness of the Rudder (Actuator cross-sectional area=500 mm^2)

Rudder Back-up Stiffness [N.mm/rad]	VT Back-up Stiffness [N.mm/rad]	Total Rotational Stiffness of the Rudder [N.mm/rad]
3.77E+08	5.28E+08	1.20E+08

Table 4.5 Elevator Back-up, Fuselage Back-up, and Total Rotational Stiffness of the Elevator (Actuator cross-sectional area=500 mm^2)

Elevator Stiffness [N.mm/rad]	Backup Stiffness [N.mm/rad]	Total Rotational Stiffness of the Elevator [N.mm/rad]
9.47E+09	4.01E+09	7.89E+08

After the determination of the total rotational stiffnesses of control surfaces, actuator areas should be determined to make the envelope flutter free. In this study, the envelope of the VLA is not used. The operational envelope of the VLA is given in Figure 4.17. When the matched point flutter analyses are performed for aileron, rudder and elevator with zero rotational stiffness, the results show that the minimum Mach number in which flutter occurs is 0.37 Mach for elevator, 0.1 Mach for aileron and there is not any flutter mechanism for rudder. The damping and frequency behaviors of the flutter mode of elevator with zero rotational stiffness (Mode Number=6) for sea level are shown in Figure 4.18 and Figure 4.19, respectively. The aim of this study is investigating the freeplay effects of multiple control surfaces by using the equivalent stiffness methodology. As Kholodar [25] claims, there should be an instability point (flutter point) inside the envelope for zero rotational stiffness of the control surface to get LCO behavior due to freeplay. Therefore, the envelope shown in Figure 4.20 is used. This envelope is taken from the paper of Kholodar [25]. Then, the altitudes of the envelope are modified by considering the VLA.

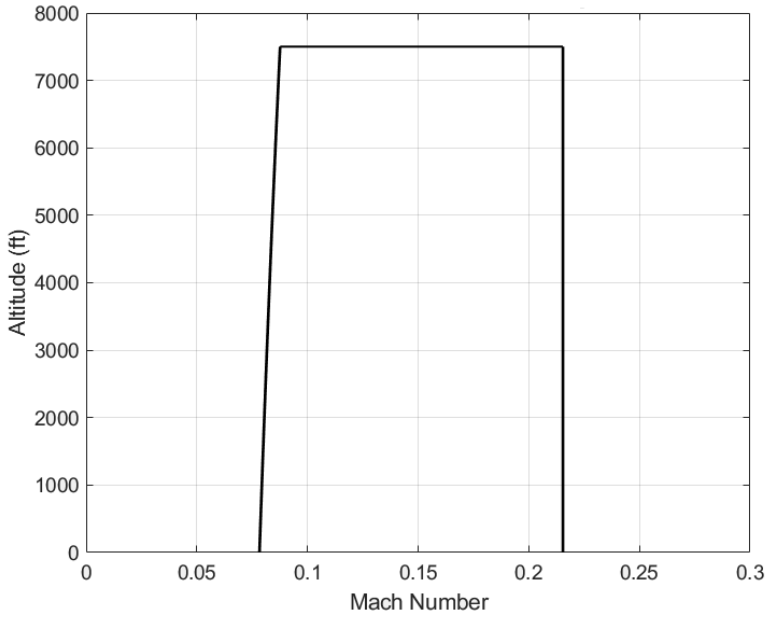

Figure 4.17. Operational Flight Envelope of the VLA

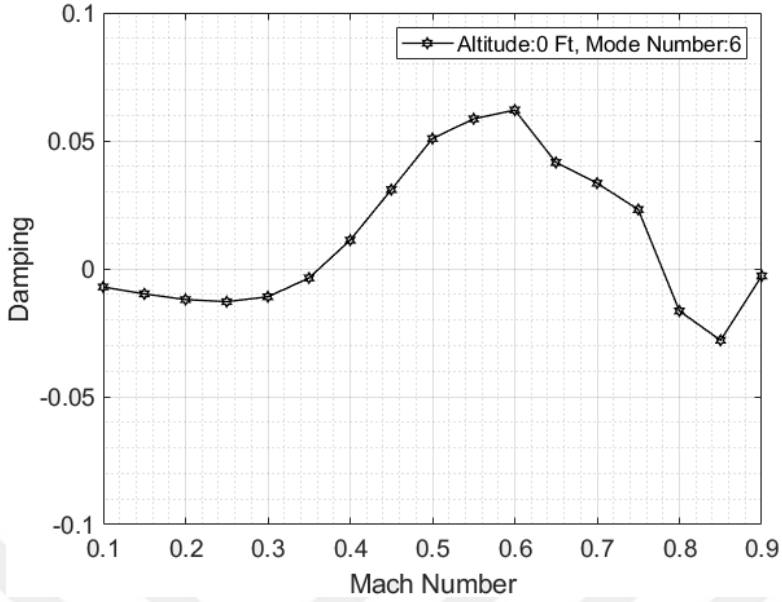

Figure 4.18. Mach Number vs Damping Curve of the Elevator with Zero Rotational Stiffness

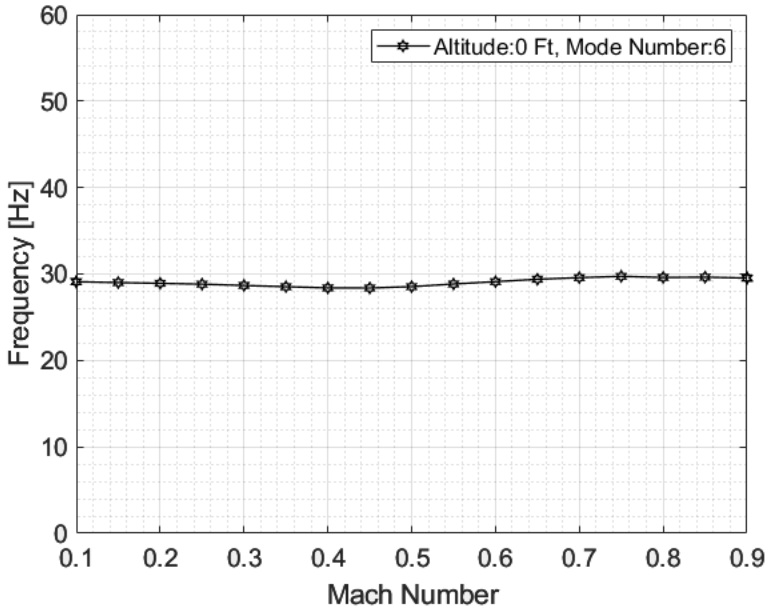

Figure 4.19. Mach Number vs Frequency Curve of the Elevator with Zero Rotational Stiffness

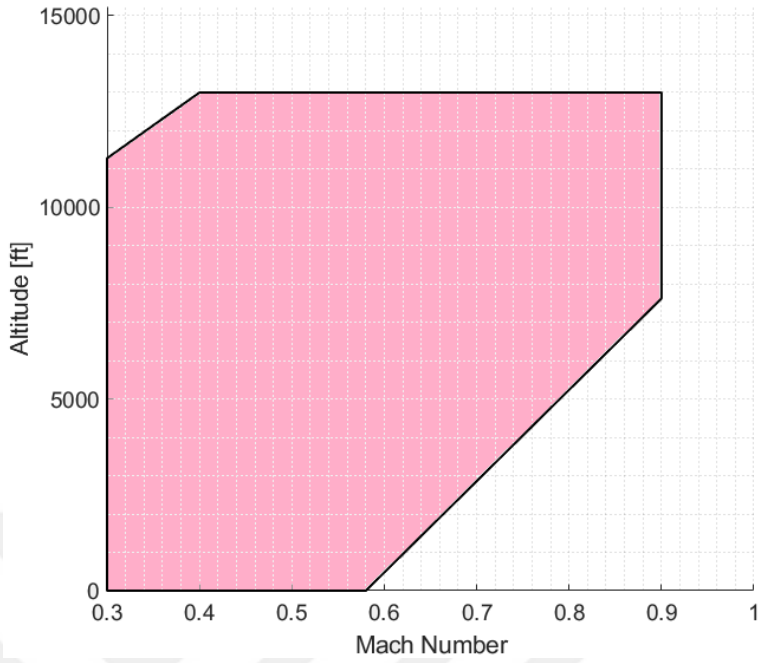

Figure 4.20. Updated Flight Envelope of VLA

A set of flutter analysis is performed for different actuator areas. The actuator areas should be determined to make the envelope flutter free. The analyses are performed by starting the actuator areas from 1 mm^2 for the rudder, aileron, and the elevator. The damping vs Mach Number and frequency vs Mach Number curves of the sea level flutter analysis are given in Figure 4.21 and Figure 4.22. The flutter modes are plotted on these graphs. There are two flutter mechanisms: Mode 6 and Mode 8. Mode 8 is an aileron related flutter mechanism and mode 6 is an elevator related flutter mechanism. Then, the actuator areas are increased to 5 mm^2 for the rudder, aileron, and the elevator. In this case, the aileron related flutter mechanism disappears. A new flutter mechanism which is related to the elevator arises. For the 5 mm^2 actuator area case, the damping vs Mach Number and frequency vs Mach Number curves of the sea level flutter analysis are given in Figure 4.23 and Figure 4.24. The damping value is low for this flutter mechanism. Normally, it is not that critical. However, this instability can cause a problem in time domain analysis. The solution can diverge due to the instability inside the envelope. Therefore, it should be pushed out of the envelope. The analysis shows that 5 mm^2 actuator area is enough

for the aileron. Rudder has no effect on any flutter mechanism. Therefore, the actuator area of rudder is assumed to be the same as aileron. For the next step, only the elevator actuator area is increased to 20 mm^2. The results show that no flutter mechanism is found in the envelope. The damping vs Mach Number and frequency vs Mach Number curves of the sea level flutter analysis are given in Figure 4.25 and Figure 4.26. The antisymmetric HT bending mode is shown and tracked. The same aeroelastic mode is tracked to show the behavior change due to the actuator area difference. It should be noted that the decided actuator areas may not be physical in terms of structural considerations such as buckling. These areas are the minimum areas to make the envelope flutter free. In this study, the decided actuator areas are used ignoring any other structural consideration. The selected actuator areas and total rotational stiffness of the components are summarized in Table 4.6.

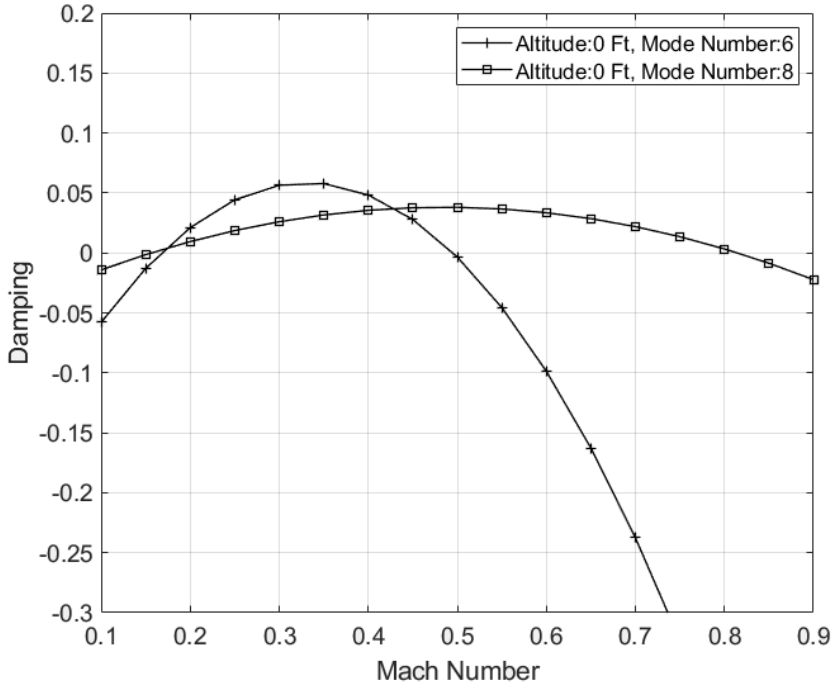

Figure 4.21. Mach Number vs Damping Curve Corresponding to 1 mm^2 Actuator Areas

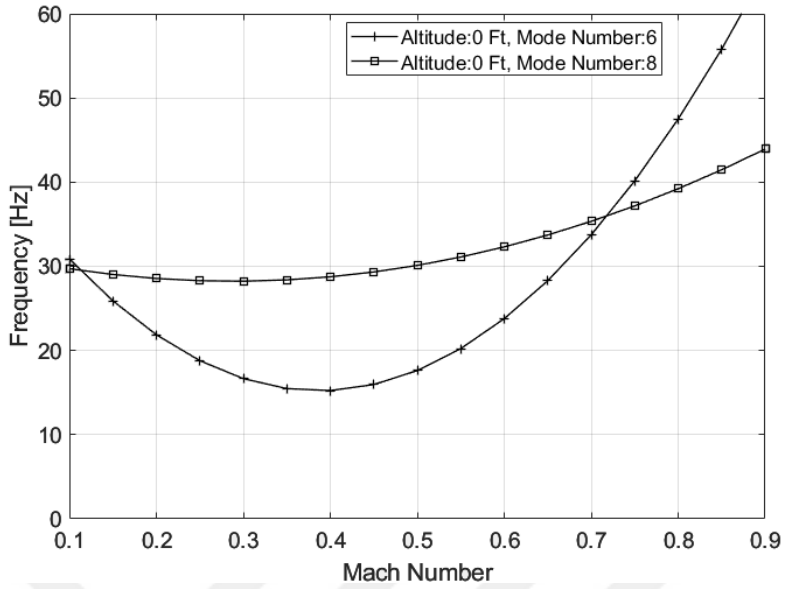

Figure 4.22. Mach Number vs Frequency Curve Corresponding to 1 mm^2 Actuator Areas

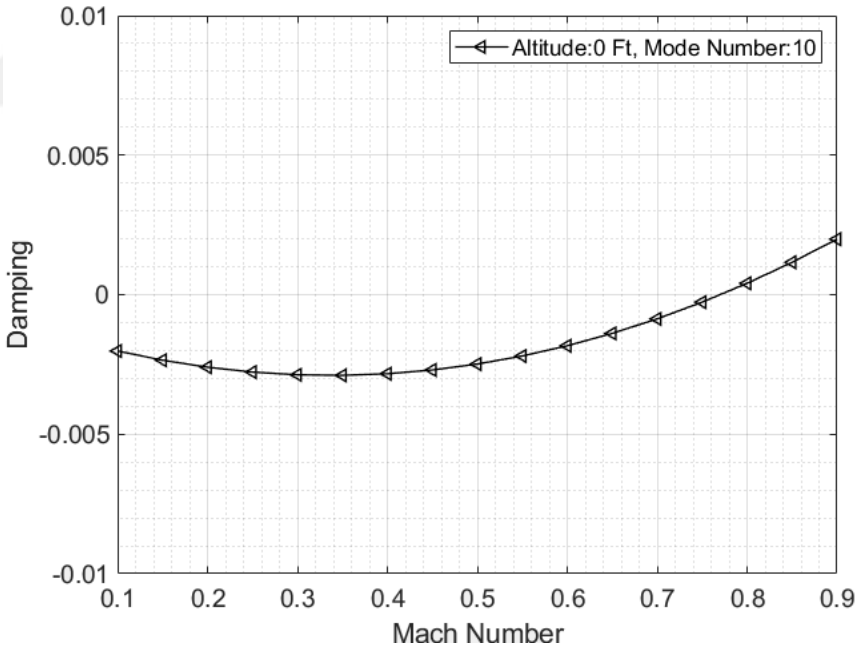

Figure 4.23. Mach Number vs Damping Curve of 5 mm^2 Actuator Areas

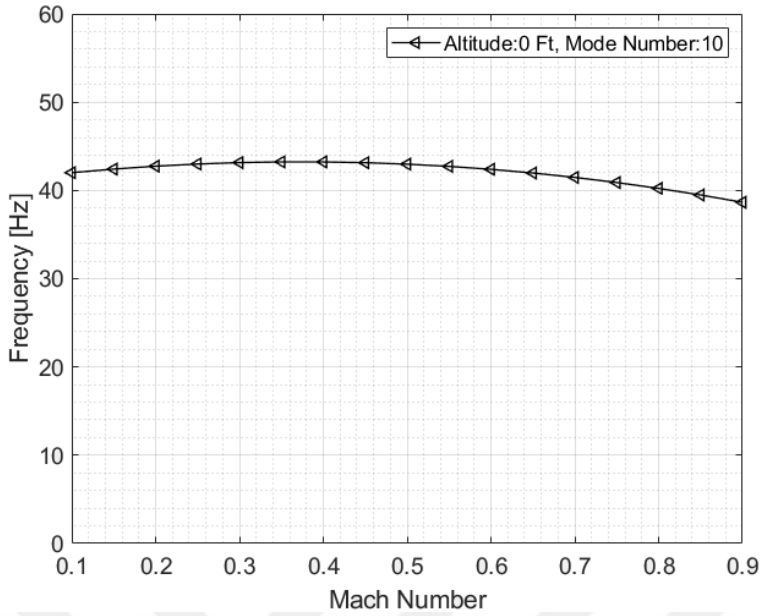

Figure 4.24. Mach Number vs Frequency Curve Corresponding to 5 mm^2 Actuator Areas

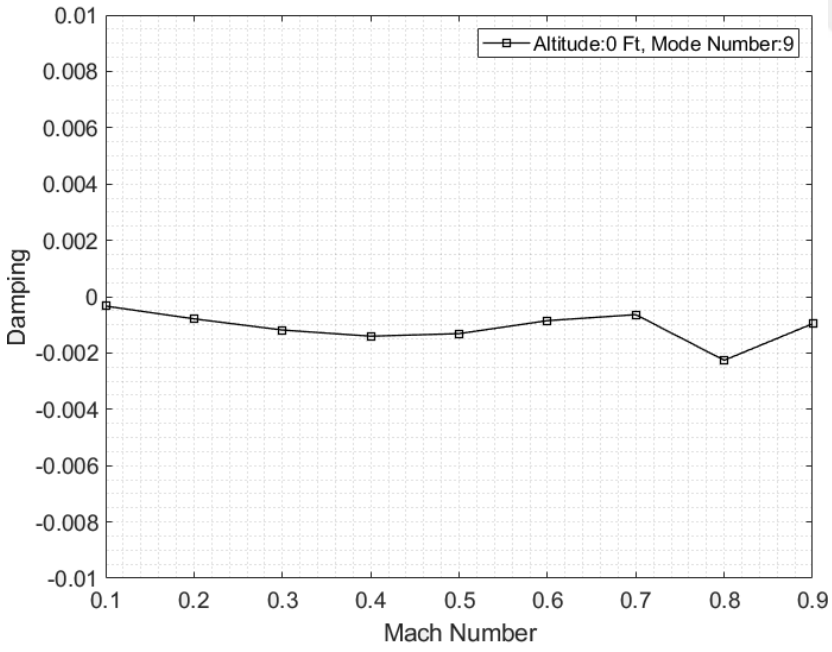

Figure 4.25. Mach Number vs Damping Curve Corresponding to 5 mm^2 Rudder and Aileron and 20 mm^2 Elevator Actuator Areas

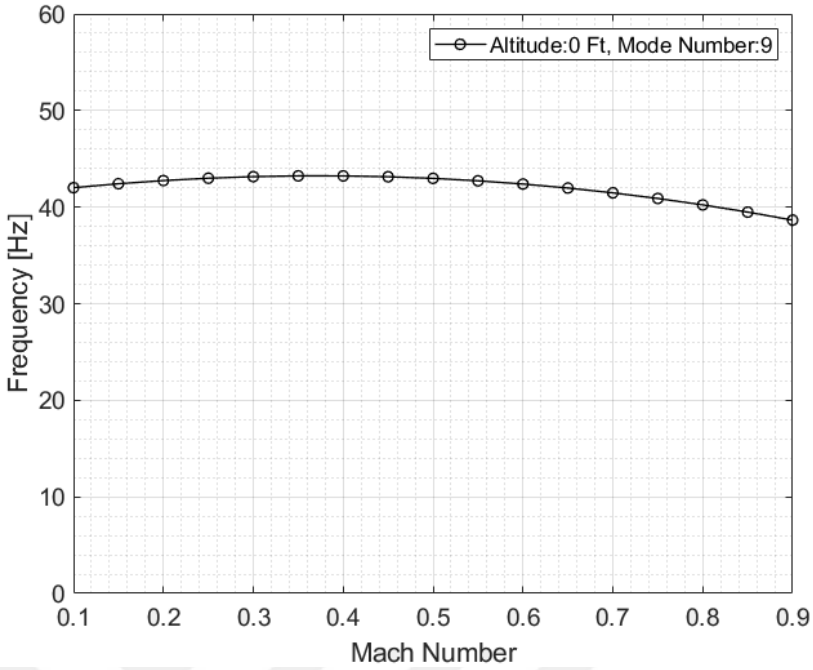

Figure 4.26. Mach Number vs Frequency Curve Corresponding to 5 mm^2 Rudder and Aileron and 20 mm^2 Elevator Actuator Areas

Table 4.6 Actuator Areas and Total Rotational Stiffness of the Control Surfaces

Component	Actuator Area [mm^2]	Total Rotational Stiffness [N.mm/rad]
Aileron	5	1.46E+06
Elevator	20	4.32E+07
Rudder	5	2.61E+06

4.1.3 Conversion of the Total Rotational Stiffness to the Bush Model

As mentioned before, the offset moment method needs concentrated stiffness which can be achieved by using the CBUSH element in MSC Nastran. For this, the control surface is connected to the main surface with the CBUSH element. In MSC Nastran, the stiffness of the connection is defined in PBUSH cards. The hinge between the control surface and the main surface is modelled using an RBE2 element. In the

PBUSH cards, rotational stiffness around the hinge axis for the hinge which is close to the actuator connection point is replaced with the total rotational stiffness which is just determined. An example connection of the control and main surfaces is shown in Figure 4.27 for elevator-horizontal tail connection.

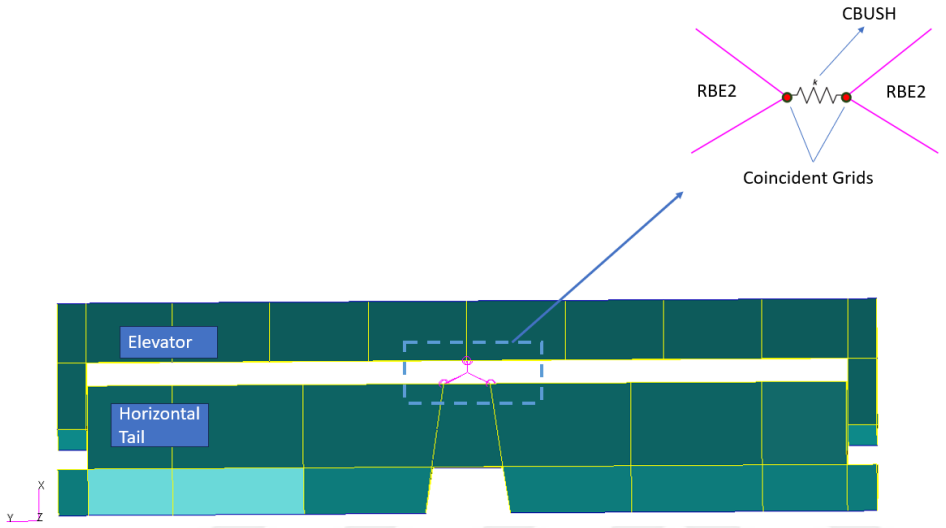

Figure 4.27. Control Surface Connection Modelling in GFEM

4.1.4 Modal Analysis Results

Normal modes analysis is a mathematical approach used to examine the dynamic behavior of a physical system. It is also known as modal analysis or mode shape analysis. In the modal analysis, the system's fundamental frequencies and mode shapes are determined. When the system is given an initial disturbance, the natural frequencies are the frequencies at which the system naturally oscillates. Each natural frequency is associated with a mode shape, which describes the spatial distribution of the system's motion at that frequency. Mode shapes reveal essential information on how the system deforms and vibrates in distinct vibration modes. The importance of normal modes analysis resides in its capacity to give insight into the dynamic properties of a system. Resonance occurs when the stimulation frequency coincides with the system's inherent frequency, resulting in excessive vibrations or structural

collapse. Also, by using normal modes analysis, engineers may forecast how a system will react to various excitations. By understanding the mode shapes, one can determine the locations that will experience the most severe displacements or stresses during vibration. By examining the mode shapes, engineers can discover parts of the system that display undesirable or excessive vibrations. This data may be used to improve the system's dynamic performance by modifying the design, such as adjusting stiffness or inserting damping features.

The governing equation of motion of a system without force excitation is written as,

$$[M]\ddot{x} + [C]\dot{x} + [K]x = 0 \tag{4.10}$$

where [M], [C] and [K] are the mass, damping and stiffness matrices respectively. For a lumped mass system, masses are assumed to oscillate harmonically with the same frequency and phase angle but with different amplitudes. So, harmonic motion at the same frequency and phase angle is conceivable. As a definition, the natural frequency is the frequency at which a body vibrates when it is disturbed without being driven or exposed to any damping force so that the damping matrix can be neglected. If the displacement of the system is assumed as,

$$x(t) = X_1 \cos(\omega t + \emptyset) \tag{4.11}$$

substituting it into Equation 4.10 yields,

$$-[M]X_1\omega^2 \cos(\omega t + \emptyset) + [K]X_1 \cos(\omega t + \emptyset) = 0 \tag{4.12}$$

$$X_1 \cos(\omega t + \emptyset)\,(-[M]\omega^2 + [K]) = 0 \tag{4.13}$$

where in Equation 4.13, $X_1 \cos(\omega t + \emptyset)$ is factored out. The determinant of the coefficient matrix must be zero for a nontrivial solution of $x(t)$.

$$\det|(-[M]\omega^2 + [K]| = 0 \tag{4.14}$$

By setting the determinant to zero produces eigenvalues and eigenvectors are then determined via Equation 4.14. In this study “Normal Modes Analysis” is performed in MSC Nastran to check whether the GFEM of the VLA has modelling problems

and to determine the dynamic characteristics of the VLA. Mode shapes and frequencies of the VLA determined utilizing the GFEM are given in Table 4.7. Normal modes analysis has been performed for the Free-Free structure and for the actuator implemented GFEM model. Because of the Free-Free structural model, the first six natural frequencies are zero. These rigid body modes are not given in Table 4.7.

Table 4.7 Natural Frequencies and Mode Shapes of the Actuator Implemented GFEM of the VLA

Mode Number	Mode Shape	Frequency [Hz]
7	The Wing First Symmetric Bending	12.42
8	Rudder Rotation	14.56
9	The Wing First Antisymmetric Bending + Antisymmetric HT Bending	22.18
10	Antisymmetric HT Bending + Antisymmetric Aileron Rotation	27.78
11	Symmetric HT Bending	29.03
12	Symmetric Aileron Rotation	32.95
13	Antisymmetric Aileron Rotation	33.77
14	Wing Symmetric In-plane Bending + Symmetric Aileron Rotation	37.05
15	Wing Antisymmetric In-plane Bending + HT In-Plane Rotation	42.72
16	Wing 2nd Symmetric Bending + Symmetric Aileron Rotation	50.1
17	Rudder Rotation + Rudder Bending +HT In plane	50.35
18	Elevator Rotation	52.07
19	Rudder Bending	53.69

Also, the normal modes analysis is performed for the CBUSH implemented GFEM of the VLA. Natural frequencies and the modal assurance criteria (MAC) with respect to the actuator implemented model is shown in Table 4.8. As can be seen from the Table 4.8, dynamic behavior of the actuator implements and the CBUSH implement models are similar.

Table 4.8 Natural Frequencies of the Bush and the Actuator Implemented GFEM Models and MAC Between Them

Mode	Frequency of Actuator Implemented GFEM [Hz]	Frequency of Bush Implemented GFEM [Hz]	Frequency Difference %	MAC
7	12.42	12.42	0.01%	1.00
8	14.56	14.51	0.32%	1.00
9	22.18	22.19	0.02%	1.00
10	27.78	27.78	0.00%	1.00
11	29.03	29.08	0.17%	1.00
12	32.95	32.86	0.29%	1.00
13	33.77	33.65	0.36%	1.00
14	37.05	37.04	0.03%	1.00
15	42.72	42.72	0.01%	1.00
16	50.10	50.09	0.02%	1.00
17	50.35	50.34	0.01%	1.00
18	52.07	51.51	1.07%	1.00
19	53.69	53.69	0.00%	1.00

4.1.5 Implementation and Verification of the Fictitious Mass Concept

In this study, two different GFEM models exist in terms of modelling of total rotational stiffness of control surfaces. Therefore, implementation of the fictitious mass concept is different for the actuator and the CBUSH implemented models in the current study. The fictitious mass technique is now widely used to describe large stiffness changes such as freeplay. First, the actuator implemented GFEM model is considered. The implementation of the fictitious mass to the aileron actuator is given

in Figure 4.28. For this, first a local coordinate system indicated by the orange arrows is created. A huge fictitious mass indicated by the yellow triangle is added (10^6 kg) in the axial direction to all control surface actuators at both ends via the CONM1 card. CONM1 card allows to define a 6x6 symmetric mass matrix at a given grid point. The given fictious mass is added to M11 term given in CONM1 card structure by defining the local coordinate system.

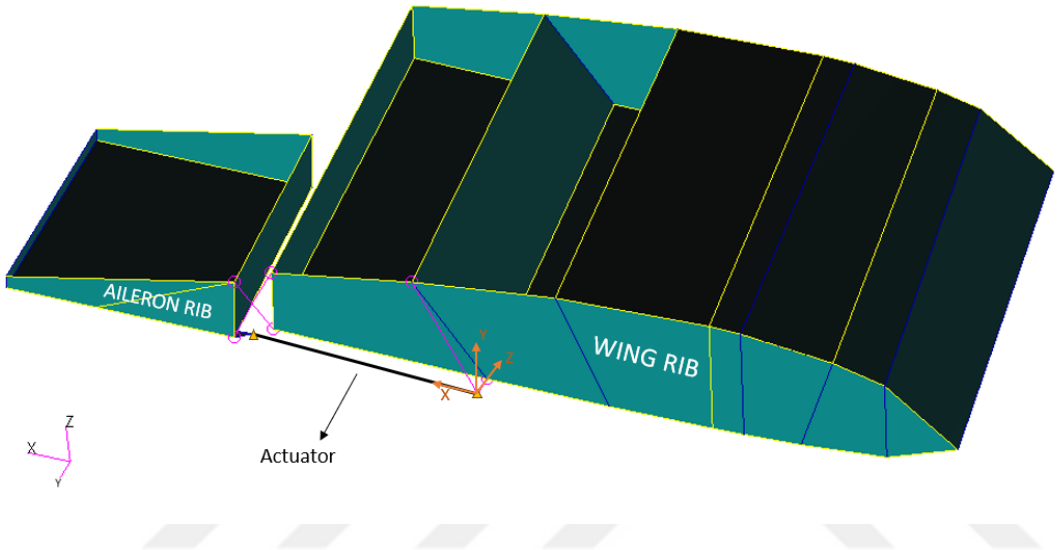

Figure 4.28. Fictitious Mass Implementation for the Aileron Actuator

In addition to this, the fictitious mass is also added to the bush implemented GFEM of the VLA. For this, a local coordinate system indicated by the orange arrows is created as shown in Figure 4.29. The y axis of this local coordinate system refers to the hinge axis. A huge fictitious mass which has mass moment of inertia indicated by the yellow triangle is added (10^{10} kg.mm^2) in the rotational direction to the end of CBUSHs of all control surfaces via the CONM1 card. Fictitious inertia is added to the rotational direction of the CBUSH element corresponding to the total rotational stiffness.

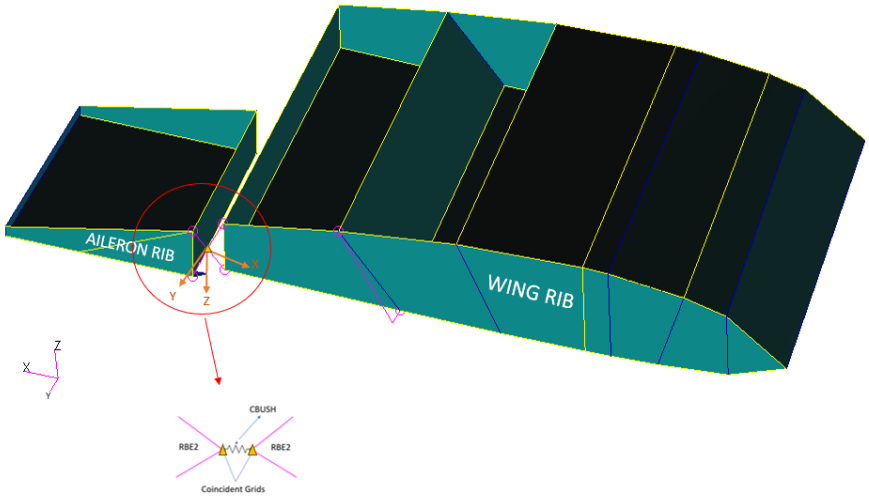

Figure 4.29. Fictitious Mass Implementation of the Aileron for the Bush Implemented GFEM of the VLA

The value of the fictitious mass is a trial-and-error process. The Karpel [26] uses a fictitious mass with six orders of magnitude larger than the overall structural component. In this study, the added fictitious mass is approximately four orders of magnitude larger than the aircraft mass for actuator implemented GFEM of the VLA and two orders of magnitude larger than the aircraft mass moment of inertia about the CG for the bush implemented one. The natural frequency and mode shape comparison results, given in Table 4.9-Table 4.12 for the actuator implemented GFEM of the VLA and in Table 4.13-Table 4.16 for the bush implemented GFEM of the VLA, show that the assigned fictitious masses are sufficient. The frequency and MAC errors are acceptable. The procedure mentioned in Karpel et al. [39] is followed to implement the fictitious mass concept. After the addition of fictitious masses to the respective locations in the GFEMs (actuator and CBUSH implemented) of the VLA, the equation of motion becomes,

$$\left[M_{nominal} + M_f\right]\ddot{x} + [K_{nominal}]x = 0 \qquad (4.15)$$

where $[M_{nominal}]$ and $[K_{nominal}]$ are the mass and stiffness matrices of the VLA which has no freeplay. The fictitious masses, M_f are added to the DOFs where the

stiffness changes occur which are the actuator elements in the actuator implemented GFEM of the VLA and CBUSH elements in the CBUSH implemented GFEM of the VLA. After the implementation of fictitious masses, a modal analysis is performed by using MSC Nastran, yielding a mass normalized mode shape matrix $[\phi_f]$.Then, the generalized mass and stiffness matrices are given as,

$$\left[GM_f\right] = \left[\phi_f\right]^T \left[M_{nominal} + M_f\right][\phi_f] \tag{4.16}$$

$$\left[GK_f\right] = \left[\phi_f\right]^T [K_{nominal}][\phi_f] \tag{4.17}$$

where $\left[\phi_f\right]^T$ is the eigenvector matrix of the VLA including fictitious masses, $\left[GM_f\right]$ and $\left[GK_f\right]$ are the generalized mass and stiffness matrices of the fictitious mass implemented structure. The fictitious masses are then removed. In this case, the generalized mass and stiffness matrices then become,

$$[GM] = \left[\phi_f\right]^T [M_{nominal}][\phi_f] \tag{4.18}$$

$$[GK] = \left[\phi_f\right]^T [K_{nominal}][\phi_f] \tag{4.19}$$

where the mass and the stiffness matrices are again generalized with respect to the modal matrix including the fictitious masses. The eigenvalues and eigenvectors can be calculated by using Equation 4.20.

$$[GM]\{\ddot{\xi}_f\} + [GK]\{\xi_f\} = 0 \tag{4.20}$$

where ξ_f is the fictitious mass modal coordinates given by $x = [\phi_f]\{\xi_f\}$.

The resultant eigenvalues are the natural frequencies of the nominal structure calculated after generalizing the system with the fictitious mass eigenvectors. In addition to this, eigenvectors are also calculated from Equation 4.20. These eigenvectors which are calculated by using Equation 4.20 is called as actual “basic” case eigenvectors (x_b) . The mode shapes of the nominal structure can be written as linear combination of the fictitious mass eigenvectors [39] as shown in Equation 4.21,

$$[\phi_b] = [\phi_f] * [x_b] \tag{4.21}$$

where $[\phi_b]$ is the modal matrix of the nominal "actual" structure. Then, the mode shapes $[\phi_b]$ which are calculated by using the fictitious mass approach can be compared with direct mode shapes of the nominal structure. The direct means that the modal analysis is performed by using MSC Nastran without adding fictitious mass. The eigenvectors and eigenvalues are directly obtained from MSC Nastran for direct results. It should be noted that Equations 4.18-4.21 can be used for any local structural stiffness change where a fictitious mass is added. In this case, Equation 4.19 can be modified as,

$$[GK] = \left[\phi_f\right]^T [K_{desired}][\phi_f] \tag{4.22}$$

where $[K_{desired}]$ is the stiffness matrix of the structural model that is analyzed such as the VLA with elevator-free, but aileron-rudder fixed etc. Again, by using Equation 4.20-4.21, the mode shapes and frequencies of the desired structural model can be calculated by using the fictitious mass.

In this study, fictitious masses are added at the same time for the aileron, elevator, and the rudder. Modal analysis of both fictitious masses implemented models are performed by using MSC Nastran, and 40 natural frequencies and mode shapes are taken from the fictious mass implemented modal analysis. Before deciding the 40 fictious mass eigenvectors and frequencies, trade-off analyses are performed. When 20 and 30 fictious mass eigenvectors and frequencies are used, the maximum frequency differences are around %10 and %4, respectively. Then, 40 fictious mass eigenvectors and frequencies are used, the maximum frequency difference is around %1. Equations 4.16-4.21 are used to calculate the mode shapes and frequencies of the desired structural model by using MATLAB. The desired structural model means that when aileron-free frequencies and mode shapes are calculated, the stiffness matrix will have elevator and rudder rotational stiffness, but aileron rotational stiffness will be zero. These matrixes are calculated to get each case frequencies and eigenvectors. Then, the calculated eigenvectors and frequencies are compared with

MSC Nastran SOL 103 results (Direct Results) for the 19 modes. The first 19 modes are selected, because flutter analyses are performed up to 54 Hz. The reason for this maximum frequency decision is that, after 54 Hz, the structure has local modes which may contaminate the aeroelastic analysis. Therefore, 54 Hz is selected as the maximum frequency. The results are presented in Table 4.9-Table 4.12 for the actuator implemented GFEM and Table 4.13-Table 4.16 for the bush implemented GFEM. In these tables, "Nominal Natural Frequencies" refers to the structure which has rotational stiffness for all the control surfaces. In addition to this, "Elevator Free", "Rudder Free" and "All Ailerons Free" cases have zero rotational stiffness around the hinge line. For all cases, first six modes are aircraft rigid-body modes. In control surface zero rotational stiffness cases, 7^{th} mode is rigid control surface rotation mode for elevator and rudder and 7^{th} and 8^{th} modes are symmetric and antisymmetric rigid rotation modes of aileron. These rigid body modes frequencies are less than 1 Hz. Therefore, the MACs are checked, and frequency difference percentages are not calculated.

Table 4.9 Nominal Natural Frequency and Mode Shape Comparisons for the Actuator Implemented GFEM

Mode	Direct Frequencies (MSC Nastran) [Hz]	Calculated Frequencies by Using the Fictitious Mass Method (Eq. 4.20-4.22) [Hz]	Frequency Difference %	MAC (Nastran Direct vs Eq. 4.21 $[\phi_b]$ Eigenvectors)
7	12.42	12.42	-0.02	1.00
8	14.56	14.57	-0.07	1.00
9	22.18	22.18	0.00	1.00
10	27.78	27.78	-0.01	1.00
11	29.03	29.03	0.00	1.00
12	32.95	33.05	-0.30	1.00
13	33.77	33.86	-0.26	1.00
14	37.05	37.12	-0.18	1.00
15	42.72	42.81	-0.20	1.00
16	50.10	50.11	-0.02	1.00

Table 4.9 continued

17	50.35	50.38	-0.07	1.00
18	52.07	52.07	0.00	1.00
19	53.69	53.79	-0.19	1.00

Table 4.10 Elevator Free Natural Frequency and Mode Shape Comparisons for the Actuator Implemented GFEM

Mode	Direct Frequencies (MSC Nastran) [Hz]	Calculated Frequencies by Using the Fictitious Mass Method (Eq. 4.20-4.22) [Hz]	Frequency Difference %	MAC (Nastran Direct vs Eq. 4.21 $[\phi_b]$ Eigenvectors)
7	0.06	0.00	-	1.00
8	12.42	12.42	-0.02	1.00
9	14.56	14.57	-0.07	1.00
10	22.18	22.18	0.00	1.00
11	27.78	27.78	-0.01	1.00
12	29.46	29.47	0.00	1.00
13	32.95	33.05	-0.30	1.00
14	33.77	33.86	-0.26	1.00
15	37.06	37.12	-0.18	1.00
16	42.72	42.81	-0.20	1.00
17	50.11	50.12	-0.03	1.00
18	50.35	50.38	-0.07	1.00
19	53.69	53.79	-0.19	1.00

Table 4.11 Rudder Free Natural Frequency and Mode Shape Comparisons for the Actuator Implemented GFEM

Mode	Direct Frequencies (MSC Nastran) [Hz]	Calculated Frequencies by Using the Fictitious Mass Method (Eq. 4.20-4.22) [Hz]	Frequency Difference %	MAC (Nastran Direct vs Eq. 4.21 $[\phi_b]$ Eigenvectors)
7	0.03	0.25	-	1.00
8	12.42	12.42	-0.02	1.00
9	22.15	22.15	0.00	1.00
10	27.77	27.77	-0.01	1.00
11	29.03	29.03	0.00	1.00
12	32.95	33.05	-0.30	1.00
13	33.77	33.86	-0.26	1.00
14	37.05	37.12	-0.18	1.00
15	42.65	42.73	-0.20	1.00
16	50.09	50.11	-0.02	1.00
17	50.17	50.21	-0.08	1.00
18	52.07	52.07	0.00	1.00
19	53.27	53.35	-0.15	1.00

Table 4.12 All Ailerons Free Natural Frequency and Mode Shape Comparisons for the Actuator Implemented GFEM

Mode	Direct Frequencies (MSC Nastran) [Hz]	Calculated Frequencies by Using the Fictitious Mass Method (Eq. 4.20-4.22) [Hz]	Frequency Difference %	MAC (Nastran Direct vs Eq. 4.21 $[\phi_b]$ Eigenvectors)
7	0.09	0.21	-	1.00
8	0.09	0.30	-	1.00
9	12.91	12.91	-0.02	1.00
10	14.56	14.57	-0.07	1.00
11	22.80	22.80	0.00	1.00
12	28.15	28.15	0.00	1.00
13	29.03	29.03	0.00	1.00

Table 4.12 continued

14	36.93	37.03	-0.25	1.00
15	42.70	42.80	-0.22	1.00
16	49.98	49.99	-0.02	1.00
17	50.34	50.38	-0.07	1.00
18	52.07	52.07	0.00	1.00
19	53.69	53.79	-0.19	1.00

Table 4.13 Nominal Natural Frequency and Mode Shape Comparisons for the Bush Implemented GFEM

Mode	Direct Frequencies (MSC Nastran) [Hz]	Calculated Frequencies by Using the Fictitious Mass Method (Eq. 4.20-4.22) [Hz]	Frequency Difference %	MAC (Nastran Direct vs Eq. 4.21 $[\phi_b]$ Eigenvectors)
7	12.42	12.42	-0.02	1.00
8	14.51	14.52	-0.07	1.00
9	22.19	22.19	0.00	1.00
10	27.78	27.78	-0.01	1.00
11	29.08	29.08	0.00	1.00
12	32.86	33.03	-0.53	1.00
13	33.65	33.81	-0.47	1.00
14	37.04	37.05	-0.03	1.00
15	42.72	42.72	-0.01	1.00
16	50.09	50.11	-0.03	1.00
17	50.34	50.37	-0.05	1.00
18	51.51	51.52	-0.01	1.00
19	53.69	53.80	-0.20	1.00

Table 4.14 Elevator Free Natural Frequency and Mode Shape Comparisons for the Bush Implemented GFEM

Mode	Direct Frequencies (MSC Nastran) [Hz]	Calculated Frequencies by Using the Fictitious Mass Method (Eq. 4.20-4.22) [Hz]	Frequency Difference %	MAC (Nastran Direct vs Eq. 4.21 $[\phi_b]$ Eigenvectors)
7	0.06	0.64	-	1.00
8	12.42	12.42	-0.02	1.00
9	14.56	14.52	0.22	1.00
10	22.18	22.19	-0.03	1.00
11	27.78	27.78	-0.03	1.00
12	29.46	29.47	0.00	1.00
13	32.95	33.03	-0.26	1.00
14	33.77	33.81	-0.10	1.00
15	37.06	37.05	0.01	1.00
16	42.72	42.72	0.00	1.00
17	50.11	50.13	-0.03	1.00
18	50.35	50.37	-0.05	1.00
19	53.69	53.80	-0.20	1.00

Table 4.15 Rudder Free Natural Frequency and Mode Shape Comparisons for the Bush Implemented GFEM

Mode	Direct Frequencies (MSC Nastran) [Hz]	Calculated Frequencies by Using the Fictitious Mass Method (Eq. 4.20-4.22) [Hz]	Frequency Difference %	MAC (Nastran Direct vs Eq. 4.21 $[\phi_b]$ Eigenvectors)
7	0.03	0.26	-	1.00
8	12.42	12.42	-0.02	1.00
9	22.15	22.16	-0.03	1.00
10	27.77	27.78	-0.03	1.00
11	29.03	29.08	-0.17	1.00
12	32.95	33.03	-0.26	1.00
13	33.77	33.80	-0.10	1.00

Table 4.15 continued

14	37.05	37.05	0.01	1.00
15	42.65	42.65	0.00	1.00
16	50.09	50.11	-0.03	1.00
17	50.17	50.21	-0.06	1.00
18	52.07	51.52	1.06	1.00
19	53.27	53.36	-0.16	1.00

Table 4.16 All Ailerons Free Natural Frequency and Mode Shape Comparisons for Bush Implemented GFEM

Mode	Direct Frequencies (MSC Nastran) [Hz]	Calculated Frequencies by Using the Fictitious Mass Method (Eq. 4.20-4.22) [Hz]	Frequency Difference %	MAC (Nastran Direct vs Eq. 4.21 $[\phi_b]$ Eigenvectors)
7	0.09	0.25	-	0.74
8	0.09	0.11	-	0.74
9	12.91	12.91	-0.03	1.00
10	14.56	14.53	0.22	1.00
11	22.80	22.81	-0.01	1.00
12	28.15	28.15	0.00	1.00
13	29.03	29.08	-0.17	1.00
14	36.93	36.94	-0.01	1.00
15	42.70	42.71	-0.01	1.00
16	49.98	49.98	-0.01	1.00
17	50.34	50.37	-0.05	1.00
18	52.07	51.51	1.06	1.00
19	53.69	53.79	-0.20	1.00

The comparisons which are given in Table 4.9-Table 4.16 shows that the stiffness change in the structural model can be represented accurately by using the fictitious mass method. The fictitious mass method allows to represent the local stiffness change in a structure with a set of fictious mass eigenvectors $[\phi_f]$.

4.2 Aerodynamic Modelling of the Very Light Aircraft

For aerodynamic modelling of the aircraft, MSC NASTRAN is used to model the lifting surfaces. The doublet lattice method (DLM) is a computational method for analyzing and forecasting the aerodynamic behavior of lifting surfaces. It entails simulating the airflow around an airfoil or wing with a lattice structure comprising doublet sources and sinks. Derivation of the doublet lattice method for lifting surfaces is mentioned in the article by Sudiana [29].

The airfoil or wing is separated into panels in the doublet lattice approach. Each panel represents the vorticity distribution along the panel as a source or sink of doublet strength. These doublet sources and sinks provide a flow field that meets the criterion of no flow through the airfoil or wing's surface. Satisfying the specified boundary criterion, such as the Kutta condition, which provides a smooth and realistic flow around the trailing edge, intensities of doublet sources and sinks are determined. The intensities of the doublets may be found by solving a set of linear equations based on the boundary conditions and flow equations.

After determining the doublet strengths, the aerodynamic forces and moments acting on the airfoil or wing may be determined. Integrating the pressure distribution along the surface of the airfoil or the wing yields the lift, drag, and pitching moment coefficients. Compared to more sophisticated numerical approaches, such as computational fluid dynamics (CFD) simulations, the doublet lattice method is more straightforward and time friendly. It has good accuracy for wings with low-to-moderate aspect ratios and moderate angles of attack.

However, it is crucial to note that the doublet lattice approach has limits. It is based on the assumption of an inviscid (frictionless) and incompressible flow, ignoring the effects of viscosity and compressibility. Furthermore, it is limited to two-dimensional flow and does not account for three-dimensional flow phenomena.

It is necessary to pay attention to some rules when performing DLM aerodynamic modeling in MSC NASTRAN [28] or other commercial tools such as ZAERO [30]. These are,

1. The coplanar surface mesh should be aligned in the stream direction. The example wing-tail modelling can be seen in Figure 4.30.

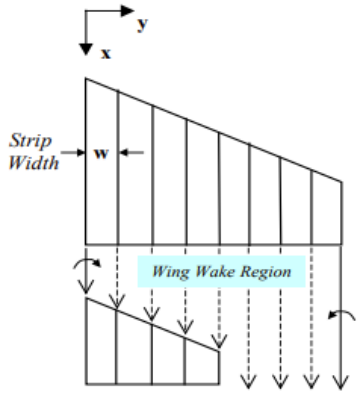

Figure 4.30. Alignment of Spanwise Divisions of a Wing-Tail Configuration [30]

2. Minimum chord length should be calculated for maximum frequency and 12 boxes per minimum wavelength is suggested. However, no less than four boxes per chord should be used. For this reason, each segment contains at least 12 aerodynamic elements. The sine-wave representation of aerodynamic elements is shown in Figure 4.31.

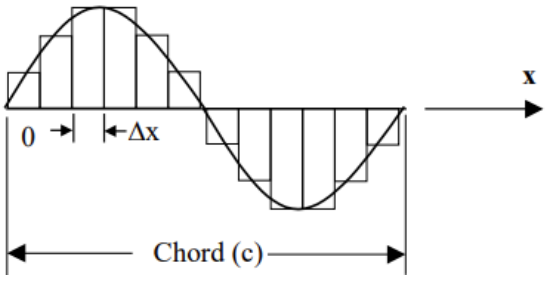

Figure 4.31. Convergence Criterion of the Minimum Number of Boxes Along the x-Direction (Flow Direction) [30]

3. Suppose a lifting surface is far from the symmetry axis. In that case, an additional lifting surface should be added to the model to overcome the unrealistic strong vortex at the root of the lifting surface. The example modeling is given in Figure 4.32.

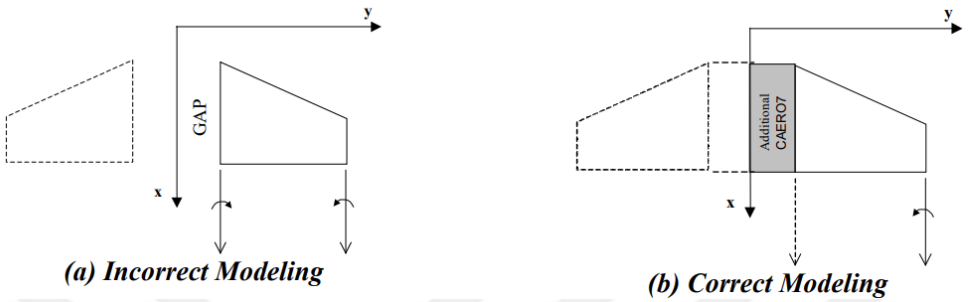

Figure 4.32. Additional Aerodynamic Elements Between the Right and Left Wings to Avoid a Gap [30]

4. The aspect ratio of aerodynamic boxes close to 1 and less than three for subsonic flow is not mandatory but recommended.

Paying attention to the rules stated above, the METU VLA aerodynamic model that is generated is given in Figure 4.33. The fuselage is not modeled as a lifting surface in the METU VLA Aerodynamic model. Control surfaces, wings, and other surfaces where aerodynamic effects are relevant are modeled in depth in this research. However, in flutter analysis, other structural elements like the fuselage (body) are often less problematic since they are not aerodynamically considered. In general, the fuselage is a less aerodynamically effective component with less impact than control surfaces, wings, or other surfaces. As a result, whole fuselage aerodynamic modeling may not be required for flutter analysis. In addition to this, fuselage is a very stiff component. Therefore, flutter which is directly related to fuselage is not expected. Modal analysis results also show this. The fuselage does not have significant elastic modes. However, like with every rule, there are exceptions. For unusual design constraints or structural elements, the influence of the fuselage in flutter analysis may need to be studied. For example, in fighter aircraft or more complicated

structural arrangements, the aerodynamic effects of the fuselage may be more prominent, necessitating extensive modeling. In this study, due to the lack of modeling of the fuselage, a bridge is implemented between two wings to prevent the surfaces from a strong vortex formation for the METU VLA aerodynamic model. Modeling of the bridge is shown in Figure 4.34.

The minimum element size of the aerodynamic box can be calculated by using Equation 4.23 [28].

$$\Delta x < 0.08\frac{V}{f} \tag{4.23}$$

In Equation 4.23, V is the minimum velocity and f is the maximum frequency which is used in aeroelastic analysis. Δx is the minimum chord length of the aerodynamic element. As mentioned before, the normal operational envelope of the VLA is not used in this study. The purpose of this research is to investigate the freeplay effects on multiple components using the equivalent stiffness approach. According to Kholodar [25], there should be an instability point (flutter point) inside the envelope for the control surface for zero rotational stiffness to get an LCO behavior due to freeplay. Hence, the envelope given in Figure 4.20 is used. The maximum Mach number considered in aeroelastic analysis is Mach 0.9 and maximum reduced frequency is 3. The reduced frequency is defined by Equation 4.24,

$$k = \frac{\omega c}{2V} \tag{4.24}$$

where, V, c and ω are the freestream velocity, reference chord length and harmonic frequency in rad/sec, respectively.

The flutter analyses of VLA are carried out at frequencies of up to 54 Hz. The rationale for this maximum frequency choice is that the structure contains local modes after 54 Hz and they might contaminate the aeroelastic analysis. As a result, 54 Hz is chosen as the maximum frequency. The minimum velocity is achieved at Mach 0.3 and at an altitude of 15000 ft. Utilizing these values in Equation 4.23 one gets the following constraint.

$$0.08\frac{0.3 * 322200\ mm/s}{54\ Hz} = 143.2\ mm \qquad (4.24)$$

The maximum chord length of the aerodynamic elements should be less than 143.2 mm to perform aeroelastic analysis accurately for the created aerodynamic model. The METU VLA aerodynamic model includes a maximum element length of 115 mm.

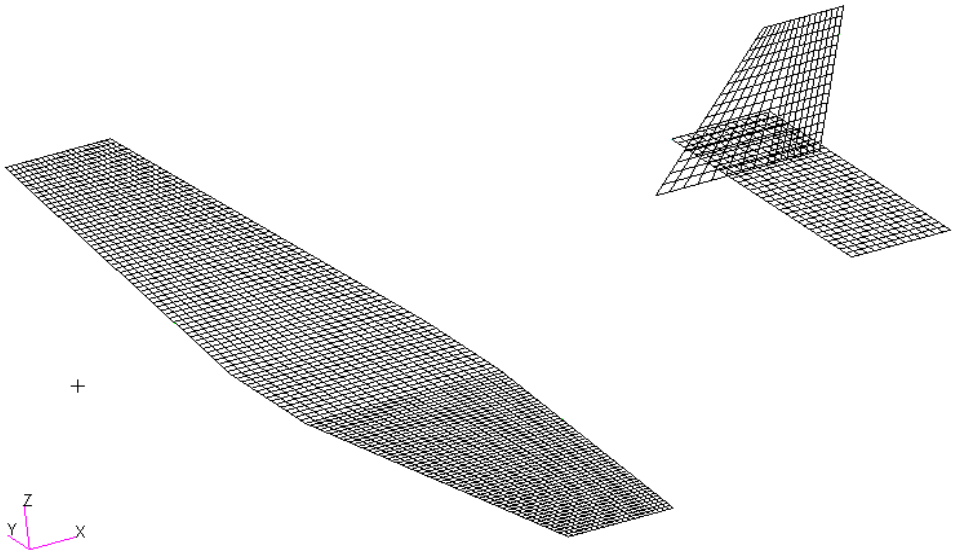

Figure 4.33. METU VLA Aerodynamic Model

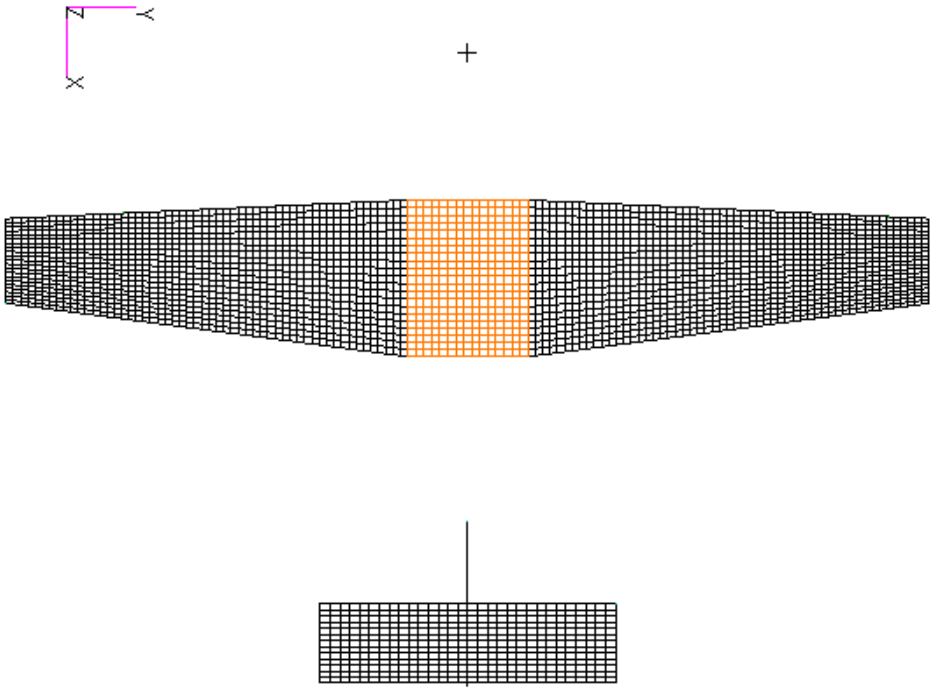

Figure 4.34. Modelling of the Bridge in the METU VLA Aerodynamic Model

4.2.1 Approximation of Frequency Domain Unsteady Forces to the Time Domain by Using the Rational Function Approximation (RFA)

MSC Nastran computes steady and unsteady pressures on aerodynamic panels at discrete Mach numbers and reduced frequencies with appropriate boundary conditions based on element type and steady/unsteady circumstances, and then saves AIC matrices.

The AIC matrix in MSC NASTRAN only depends on the reduced frequency and Mach Number for the given aerodynamic model. In this study, AIC matrices are calculated for several reduced frequencies and Mach numbers. Then, Generalized Aerodynamic Forces (GAFs) are extracted from MSC NASTRAN. The equation of motion of an aeroelastic system in generalized coordinates can be written as [40],

$$[GM]\{\ddot{\xi}\} + [GK]\{\xi\} = q[Q(ik)]\{\xi\} \tag{4.26}$$

where; $[GM]$, $[GK]$ and $[Q(ik)]$ are generalized mass, stiffness and generalized aerodynamic force (GAF) matrix with respect to the modal matrix $[\phi]$, respectively. GAFs ($[Q(ik)]$) can be formulated as,

$$[Q(ik)] = [\phi]^T[G]^T[AIC][G][\phi] \tag{4.27}$$

where, $[G]$ refers to the spline matrix. The DOF number (n_{aero}) of the aerodynamic model and the DOF ($n_{structure}$) of the structural model (modal matrix) are not compatible. Therefore, a spline is required to transfer the structural mode shapes to the aerodynamic panels. It should be noted that the AIC matrix is a matrix of order n_{aero}x n_{aero}. The DOF number of AIC is equal to the number of aerodynamic elements. The generalized aerodynamic force matrices are obtained for discrete reduced frequencies. In non-linear aeroelastic analysis, such as the freeplay nonlinearity studied in this thesis, conversion of generalized aerodynamic forces to the time domain is required using Rational Function Approximation (RFA). This phase requires converting the GAF matrices from the frequency domain to the Laplace (s) domain. It should be noted that the GAF matrices are initially computed for discrete reduced frequencies. However, because the Laplace domain is continuous, a particular expression is assumed during this transformation procedure. In this context, the assumption in Equation 3.17 is made [40]. The transformation requires introducing aerodynamic lag roots on the negative axis, aligning with the negative real axis in the Laplace domain, facilitating a smooth transition to the time domain using Inverse Fourier Transform methods and resolving discontinuity by strategically placing lag roots, as shown in Figure 3.2 [40]. The determination of the aerodynamic lag roots is a trial-error process. Several iterations are required to find the best roots.

When a structure oscillates in a steady and uniform wind field, it experiences a time varying aerodynamic load due to the relative motion between the structure and the wind field. This unsteady loading may be divided into two components: one in phase with the displacement of the structure, which accounts for aerodynamic stiffness, and another in phase with the velocity, which can be interpreted as aerodynamic damping

[34]. The approximation of the aerodynamic forces in Laplace domain is given in Equation 3.17.

The Laplace variable 's' can be written as given in Equation 4.28 by using Equation 3.2 and the g=0 assumption [40].

$$s = \frac{jk2V}{c} \tag{4.28}$$

After the substitution of the Equation 4.28 into 3.3, the resultant equation is shown in Equation 4.29 [33].

$$Q(k) = A_0 + (jk)A_1 + (jk)^2 A_2 + \sum_{n=1}^{M} \frac{jkA_{n+2}}{(jk + \beta_n)} \tag{4.29}$$

where, M is the partial fractions which is equal to the order of the overall denominator of polynomial. The main aim is to fit the discreate frequency domain forces to the Equation 4.29.

Let us assume one lag root for the system. Then, the M is 1 for this case. In this case, the equation can be divided into real and imaginary parts as [33],

$$Q_{real}(k) = A_0 - k^2 A_2 + \frac{k^2 A_3}{k^2 + {\beta_1}^2} \tag{4.30}$$

$$Q_{imaginary}(k) = A_1 k + \frac{\beta_1 k A_3}{k^2 + {\beta_1}^2} \tag{4.31}$$

The real and imaginary parts of the generalized aerodynamic force matrix are calculated for discrete reduced frequencies and have error functions (E) as defined in Equation 4.32 and 4.33 [33],

$$E_{R,i} = Q_{R,i} + [B_{R,i}]\{C\} \tag{4.32}$$

$$E_{I,i} = Q_{I,i} + [B_{I,i}]\{C\} \tag{4.33}$$

$$[B_{R,i}] = \left[-1, 0, {k_i}^2, \frac{-{k_i}^2}{{k_i}^2 + {\beta_1}^2}\right]_{1x4} \quad (4.34)$$

$$[B_{I,i}] = \left[0, -1, 0, \frac{-\beta_1 k_i}{{k_i}^2 + {\beta_1}^2}\right]_{1x4} \quad (4.35)$$

$$\{C\} = \{[A_0], [A_1], [A_2], [A_3]\}^T \quad (4.36)$$

where, matrices B_R , B_I and C are defined by Equations 4.34-4.36. Subscript *'i'* refers to a particular reduced frequency (k_i) at which Q is calculated. $Q_{R,i}$ and $Q_{I,i}$ are known data from frequency domain. Moreover, $[B_{R,i}]$ and $[B_{I,i}]$ are the real and imaginary constants of the complex Equation 4.29 for reduced frequency *'i'*, respectively. $Q_{R,i}$ and $Q_{I,i}$ are the real and the imaginary parts of the GAF matrix. Hence, the overall complex error function becomes [33],

$$E_i = E_{R,i} + jE_{I,i} \quad (4.37)$$

Then the least square fit can be generated for 'N' reduced frequency as,

$$\frac{\partial}{\partial C}\sum_{i=1}^{N}(E_i \times E_i') = 0 \quad (4.38)$$

where, E_i' represents the complex conjugate. By solving the Equation 4.38, the coefficients of the fit ($\{C\}$) can be calculated as follows [33],

$$\{C\} = -\left[\sum_{\mathrm{i}=1}^{\mathrm{N}}\left([B_{R,i}]^{\mathrm{T}}[B_{R,i}] + [B_{I,i}]^{\mathrm{T}}[B_{I,i}]\right)\right]^{-1}\sum_{\mathrm{i}=1}^{\mathrm{N}}\left(Q_{R,i}[B_{R,i}]^{\mathrm{T}} + Q_{I,i}[B_{I,i}]^{\mathrm{T}}\right) \quad (4.39)$$

Having calculated $A_0, A_1, A_2\ and\ A_3$ from Equation 4.39, then the final Laplace domain approximated aerodynamic forces can be calculated by using Equation 4.29.

4.2.2 Verification of the RFA

The modal approach to structural dynamics is based on the idea that structural displacements may be appropriately described as a linear combination of certain baseline modes and modal displacement vectors.

$$\{x\} = [\phi]\{\xi\} \tag{4.40}$$

where $\{x\}$ is the structural displacements vector, $\{\xi\}$ is the modal displacements vector and $[\phi]$ is the modal matrix. VLA structural model contains 13500 degrees of freedom (DOF) for each mode. In this study, 13 modes are included in the aeroelastic analysis. It is critical to recognize that the 6 rigid-body modes are omitted from aeroelastic analysis. Therefore, the included modes are 7 to 19.

If zero structural damping is assumed, equation of motion in generalized coordinates becomes as [40],

$$[GM]\{\ddot{\xi}\} + [GK]\{\xi\} = q[\phi]^T[G]^T[AIC][G][\phi]\{\xi\} \tag{4.41}$$

In Equation 4.41, $[G]$ refers to spline matrix. The aerodynamic model consists of 3255 aerodynamic elements and the size of the AIC matrix is 3255x3255. Therefore, the spline matrix $[G]$ matrix size becomes 3255x13500.

It is critical to emphasize that the generalized aerodynamic force matrices (GAF) are non-dimensional in terms of mode shapes and are computed at specified Mach numbers and reduced frequencies. In this study, a MATLAB code is generated to implement the RFA. Real and imaginary parts of GAF matrices corresponding to, mode 9 (Wing's First Antisymmetric Bending & Antisymmetric HT Bending) and mode 16 (Wing's 2nd Symmetric Bending + Symmetric Aileron Rotation at 0.3 Mach are compared across all reduced frequencies in Figure 4.35 and Figure 4.36. The orange circles refer to discrete reduced frequency data of the frequency domain generalized aerodynamic forces. It can be concluded that RFA approximation of the generalized aerodynamic forces match quite well with the discrete frequency domain generalized aerodynamic forces.

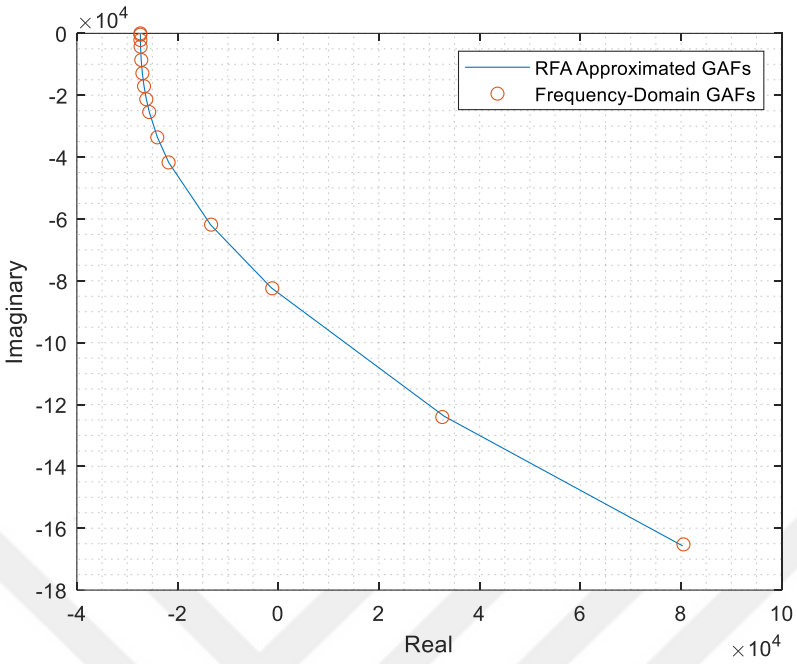

Figure 4.35. Comparison of the RFA Approximation of Mode 9 (Q_{99}) for Mach 0.3

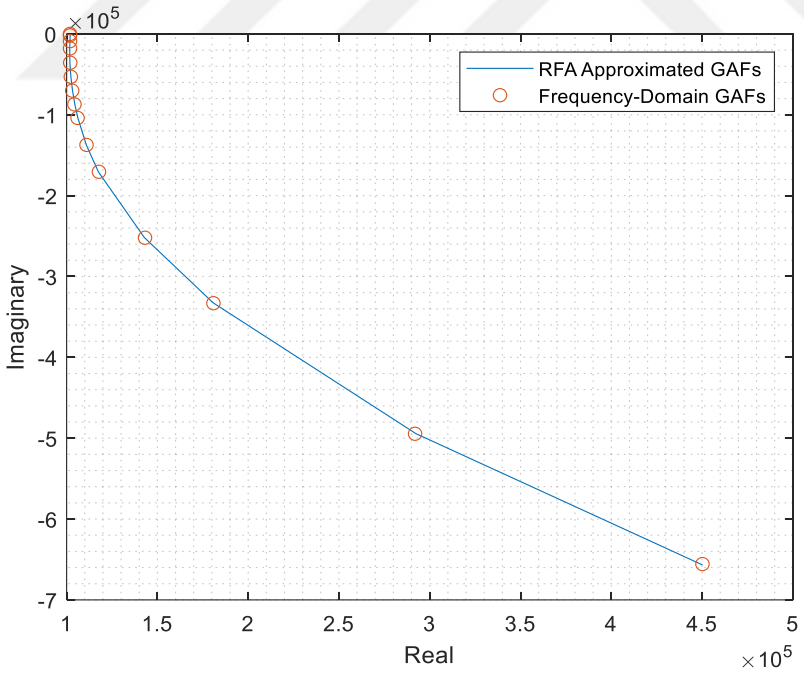

Figure 4.36. Comparison of the RFA Approximation of Mode 16 (Q_{1616}) for Mach 0.3

4.3 Aeroelastic Modelling of the Very Light Aircraft

Aeroelasticity is a field that necessitates a thorough knowledge of the interaction of structural and aerodynamic models. The assessment of changes in aerodynamic forces and moments caused by structural displacements is a critical part of this interaction. The creation of a spline is required to ease the transition of modal displacements into the aerodynamic model. This procedure entails carefully selecting appropriate structural grids and aligning them with related aerodynamic panels. It is critical to remember that the structural grids used should predominantly reflect the aircraft's hard points to minimize any negative interaction between local mode shapes and the aerodynamic model [28].

Grids located along the aircraft frames, ribs, and spars of the aircraft structure are common candidates for spline points. The structural and aerodynamic models may be efficiently integrated by creating this relationship via the spline, allowing for precise and insightful aeroelastic assessments.

In this study, Infinite Plate Spline (IPS) [28] is used for the aeroelastic analysis of the METU VLA. IPS is considered as the best spline method for panel plate modelling. Raveh et al. [35] explains the advantage of IPS. They mention that the IPS approach has the benefit of producing a smooth deflected mesh. Another benefit of the IPS technique is that the same spline procedures may be used to represent the deflected control surfaces as well as to map elastic modes from structural nodes to aerodynamic grids.

In this study, hard points of the METU VLA aircraft are selected as shown in Figure 4.37- Figure 4.38. For the wing and control surfaces, the hard points are selected from upper surfaces of the components. In addition to this, the lower surface grids of the pilot seat are selected for spline.

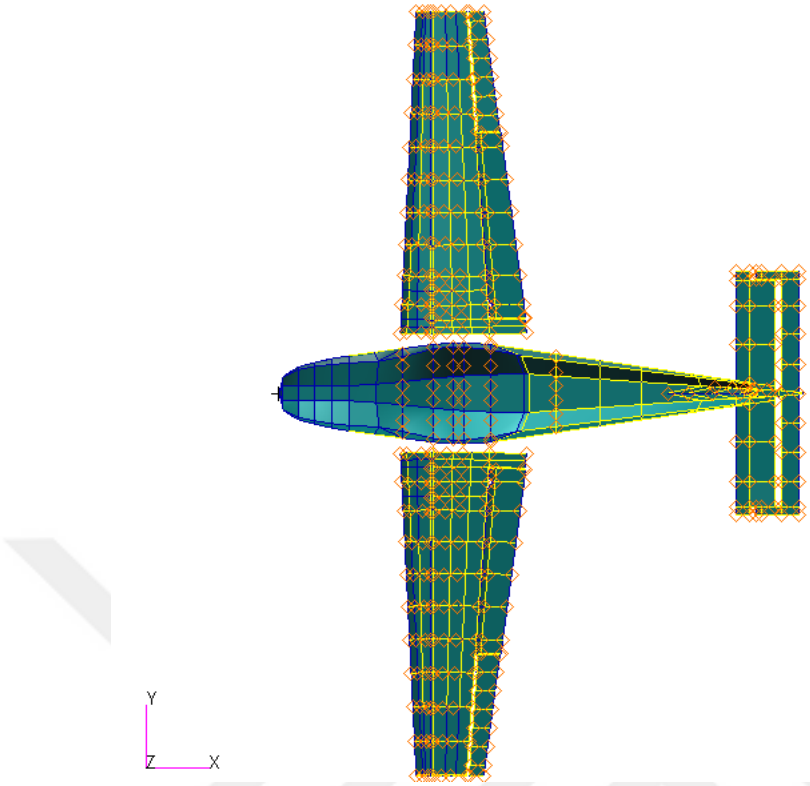

Figure 4.37. Top View of Splined Nodes

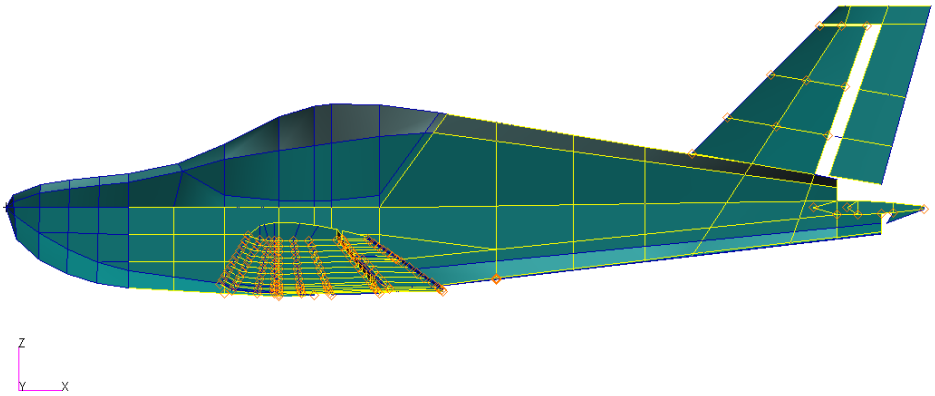

Figure 4.38. Side View of Splined Nodes

4.3.1 Verification of the Selected Spline Configurations

Even if hard points are selected from the structural model to construct the spline matrix, some incorrect interpolation may occur. Hence, performance of the selected spline points should be checked. This check is commonly done visually. In Table 4.17- Table 4.21, some selected modes and their interpolated mode shapes are compared. It is concluded that spline quality is good to perform aeroelastic analysis.

Table 4.17 Spline Verification for Mode 7 in Table 4.7

Structural Mode Shape	Interpolated Mode Shape in Aerodynamic Panels
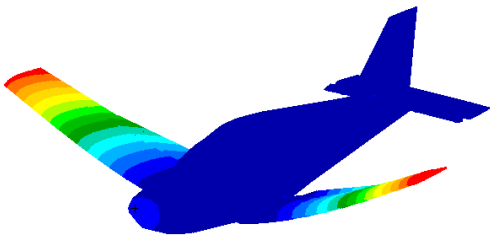	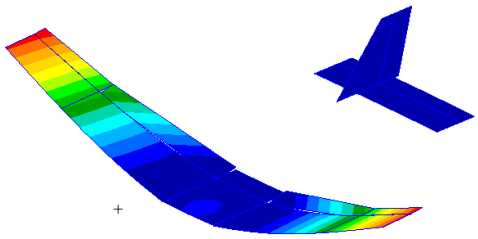

Table 4.18 Spline Verification for Mode 9 in Table 4.7

Structural Mode Shape	Interpolated Mode Shape in Aerodynamic Panels
	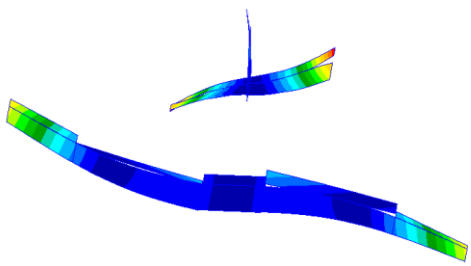

Table 4.19 Spline Verification for Mode 11 in Table 4.7

Structural Mode Shape	Interpolated Mode Shape in Aerodynamic Panels
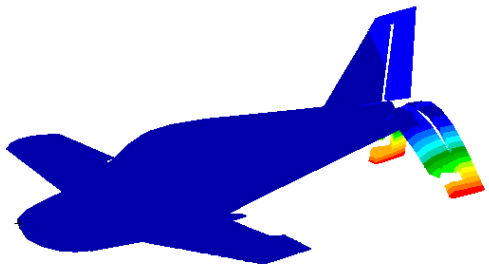	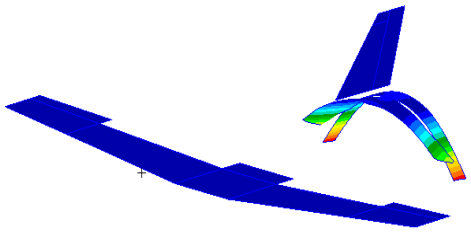

Table 4.20 Spline Verification for Mode 16 in Table 4.7

Structural Mode Shape	Interpolated Mode Shape in Aerodynamic Panels
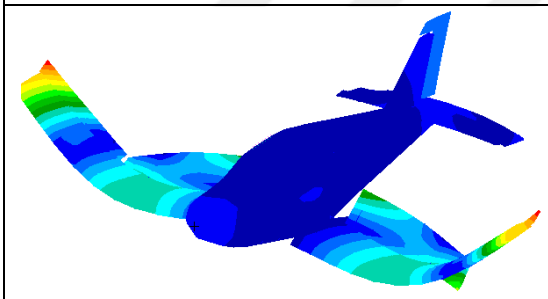	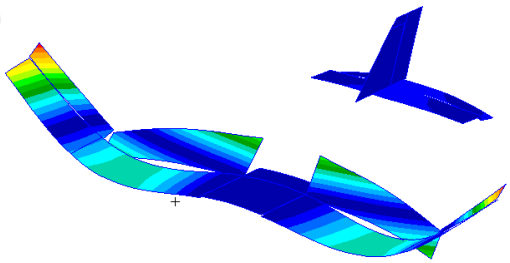

Table 4.21 Spline Verification for Mode 19 in Table 4.7

Structural Mode Shape	Interpolated Mode Shape in Aerodynamic Panels
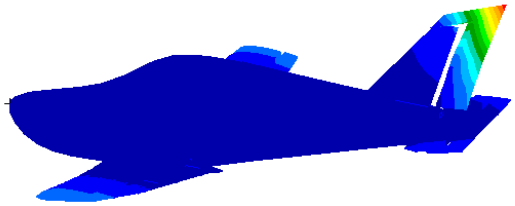	

4.3.2 Linear Flutter Analysis Results of the METU VLA

To prepare the structural model for nonlinear analysis, it is assumed that there is no flutter within the flight envelope is shown in Figure 4.20 for the nominal control loop stiffness values. Also, as Kholodar [25] postulated that there should be instability within the flight envelope for zero rotational stiffness to get LCO behavior due to freeplay. Flight envelope which is used for flutter analysis is given in Figure 4.20. First, the control surface total rotational stiffnesses are assumed to create a flutter free envelope. The total rotational stiffness values, determined in Section 4.1.2, are given again in Table 4.22 and they used for the aeroelastic analysis of the VLA. All flutter analysis is conducted by using solution sequence 145 of MSC NASTRAN. For the flutter solution, the P-K method [28] is used as the solver.

Table 4.22 Control Loop Stiffness of Control Surfaces

Component	Actuator Area [mm^2]	Total Rotational Stiffness [N.mm/rad]
Aileron	5	1.46E+06
Elevator	20	4.32E+07
Rudder	5	2.61E+06

4.3.2.1 PK Method

In aeroelasticity, the p-k technique is commonly used to investigate the flutter behavior of aircraft. The p-k technique is based on one-dimensional unstable airfoil theory, and it is also known as the "British Method". The method is subsequently modified by Rodden to be implemented in NASTRAN [30].

The equation motion in generalized coordinates given in Equation 3.2 which is explained in Chapter 3.1 is recalled in Equation 4.42.

$$[GM]\{\ddot{\xi}(t)\} + [GC]\{\dot{\xi}(t)\} + [GK]\{\xi(t)\} = [Q_{HH}] \tag{4.42}$$

where; $[GM]$,$[GC]$ and $[GK]$ are the generalized mass, damping and stiffness matrices with respect to the modal matrix [ϕ], respectively. Also, $[Q_{HH}]$ is the generalized aerodynamic force matrix.

$$[GM] = [\phi]^T[M][\phi] \tag{4.43}$$

$$[GK] = [\phi]^T[K][\phi] \tag{4.44}$$

$$[GC] = [\phi]^T[C][\phi] \tag{4.45}$$

$$[Q_{HH}] = [\phi]^T\{\mathrm{F_a(t)}\} = q_\infty[\phi]^T[G]^T[AIC][G][\phi]\{\xi(t)\} \tag{4.46}$$

In the implementation of the PK method in Nastran, the aerodynamic forces are represented as real and imaginary components of the generalized aerodynamic forces.

$$[Q_{HH}] = [Q_{HH}]^R + i[Q_{HH}]^I \tag{4.47}$$

Then, equation of motion given in Equation 4.42 can be rewritten as,

$$[GM]\{\ddot{\xi}(t)\} + [GC]\{\dot{\xi}(t)\} + [GK]\{\xi(t)\} - q_\infty[Q_{HH}]^R - q_\infty i[Q_{HH}]^I = 0 \tag{4.48}$$

In PK method, solution of the system assumed to be $\{\xi\} = \{\bar{\xi}\}e^{pt}$. In the assumption, eigenvalue p is defined as,

$$p = \omega(\gamma \mp i) \tag{4.49}$$

The transient decay rate coefficient, abbreviated as γ, is a parameter related to the structural damping coefficient, indicated as g. The transient decay rate coefficient is half the value of the structural damping coefficient g, according to the relationship g = 2 γ. Frequency is also represented in non-dimensional form as the reduced frequency k.

$$k = \frac{\omega c}{2V} = \frac{imag(p)\ c}{2V} \tag{4.50}$$

In Equation 4.50, ω, c and V are the angular frequency, reference chord length and free-stream velocity, respectively. The modes of major importance in an aeroelastic system are those with low damping, whereas areas with high damping are not critical. Because the decay parameter is much smaller than the angular frequency (ω). Then, Equations 4.51 and 4.52 can be written.

$$\frac{p}{i\omega} = \frac{\omega\gamma + \omega i}{i\omega} \tag{4.51}$$

$$\frac{p}{i\omega} \approx 1 \tag{4.52}$$

Then, the imaginary part of the generalized aerodynamic force matrix, which is given in Equation 4.48, can be written as by using Equation 4.53,

$$q_\infty i[Q_{HH}]^I \approx q_\infty \frac{p}{i\omega} i[Q_{HH}]^I \tag{4.53}$$

After some manipulations, the fundamental equation of the PK method becomes,

$$\left[p^2[GM] + \left([GC] - \frac{\rho cV}{4k}[Q_{HH}]^I\right)p + ([GK] - \frac{\rho V^2}{2}[Q_{HH}]^R)\right]\{\bar{\xi}\}e^{pt} = 0 \tag{4.54}$$

The stages for solving the flutter speed and frequency by the PK Method are summarized as follows:

- Define the speed range that the aircraft will experience during flight and the air density.
- Execute the following steps for each speed within the provided range:

1. Select the reduced frequency.
2. Calculate the aerodynamic forces corresponding to the selected reduced frequency and the Mach number.
3. Determine the frequency and damping values by solving the eigen value problem in Equation 4.54.
4. Calculate the reduced frequency by using the eigenvalue p which is determined in step 3.
5. Compare the calculated reduced frequency and the assumed reduced frequency in step 1. If these values do not match, go back to step 1, and assume a new reduced frequency until the convergence is achieved.
6. If the calculated reduced frequency and the given reduced frequency matched, save the frequency, damping and speed values.

- Repeat all the steps for each speed.

4.3.3 Zero Control Loop Stiffness Flutter Results

As mentioned before, there should be instability within the flight envelope for zero control surface stiffness to get a LCO behavior due to freeplay. The flutter boundaries for the zero-control loop stiffness of the aileron and the elevator are presented in Figure 4.39 and Figure 4.40, respectively. It should be noted that the same flutter boundaries are obtained for the actuator and the bush implemented GFEMs since both models are similar in terms of dynamic characteristics. The shaded area in figures refers to flutter regions in the envelope for zero rotational stiffness cases. It means that there is flutter inside this shaded region. In addition to this, these shaded areas are possible LCO regions in the envelope. For rudder zero rotational stiffness case, no flutter is observed inside the flight envelope.

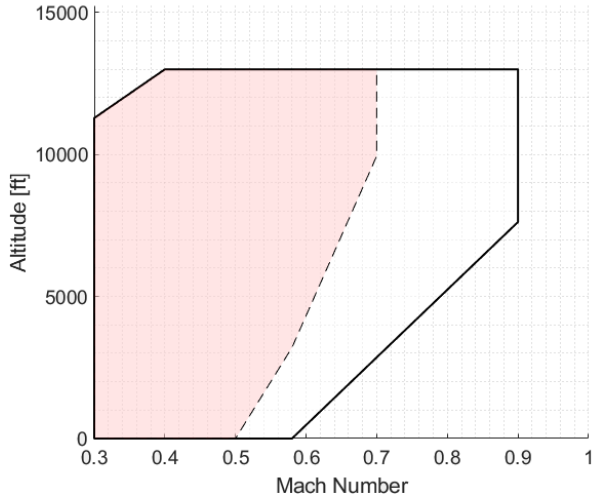

Figure 4.39. Flutter Boundary for Zero-Rotational Stiffness of the Aileron

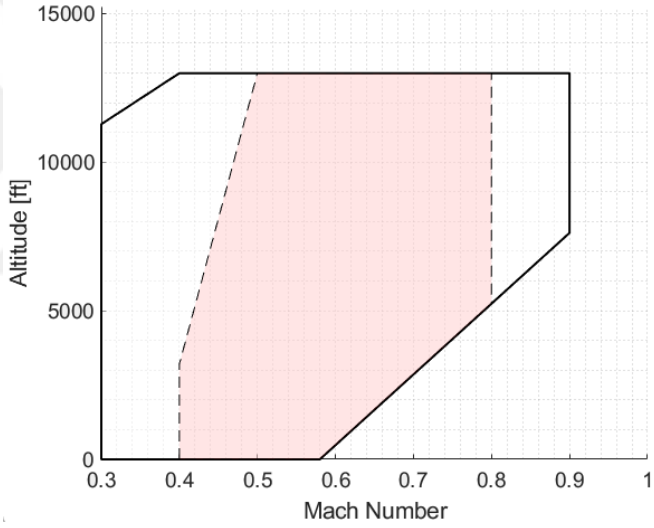

Figure 4.40. Flutter Boundary for Zero-Rotational Stiffness of the Elevator

CHAPTER 5

CONTROL SURFACE FREEPLAY ANALYSIS OF THE VLA THROUGH THE EQUIVALENT STIFFNESS APPROACH

In this chapter, control surface freeplay analysis of the VLA is performed using the equivant stiffness approach. By using the equivalent stiffness methodology, for both actuator and bush imlemented GFEM, METU VLA aircraft is analyzed for different flight conditions and different freeplay angles to determine the maximum allowable freeplay limits. Freeplay analysis results of the VLA are examined and compared with the pilot seat acceleration restriction, which is specified as ±0.12g [15].

The aim of the study is to determine the maximum freeplay limits of the control surfaces by using the equivalent stiffness methodology. Anderson et al. [15] defines some criteria for maximum freeplay limits. The first criterion is that the moment which is produced by the LCO should not exceed %10 of the hinge moment corresponding to the design limit loads. The second criterion is related to the pilot's comfort. Acceleration should not exceed $\pm$0.12g at the pilot's seat. In this phase of the VLA design, hinge moment design limit loads are not mature. Therefore, in this study pilot seat acceleration is considered to determine the maximum freeplay limits. RMS values are taken into account in comparing the accelerations at the pilot seat with the $\pm$0.12g acceleration limits specified. The results are also compared with the describing function method.

5.1 Describing Function Method

The describing function approach is a useful methodology for analyzing nonlinear systems with hysteresis and backlash, such as those seen in freeplay systems. When used in freeplay analysis, the describing function approach is a powerful tool for simulating the behavior of a nonlinear system as a linear one around an operational

point in the frequency domain. The method linearizes the freeplay characteristics by describing the frequency domain relation between the input and output signals [7]. If preload is assumed as zero, sinusoidal deflection of the control surface can be defined as $\beta = \beta_{max}\cos(\omega t)$.The torque due to freeplay can be defined as in Equation 5.1,

$$Torque = \begin{cases} K_a(\beta - \delta_0), & \beta > \delta_0 \\ 0, & \delta_0 \geq \beta \geq -\delta_0 \\ K_a(\beta + \delta_0), & \beta < -\delta_0 \end{cases} \tag{5.1}$$

where β is the rotational deflection of the control surface and δ_0 is the freeplay angle. K_a is the nominal control surface stiffness around the hinge axis. The variable y is defined as the ratio of the freeplay angle to the maximum rotation of the control surface [7].

$$y = \frac{\delta_0}{\beta_{max}} \tag{5.2}$$

For any freeplay analysis, the maximum oscillation of the control surface should be greater than freeplay angle ($\beta_{max} > \delta_0$) and $\delta_0 \geq 0$ to consider the oscillation as LCO. Therefore, y will be in the range of [0,1). When $\beta = \delta_0$, $\beta = \delta_0 = \beta_{max}\cos(\omega t)$ and if this equation is solved for ωt, one gets ωt as,

$$\omega t = \pm acos(y) + 2\pi n \tag{5.3}$$

If $\beta = -\delta_0$,

$$\omega t = \pi \pm acos(y) + 2\pi n \tag{5.4}$$

Putting back the expressions for β in terms of ωt by substituting Equation 5.2,5.3 and 5.4 into Equation 5.1, we get the new form of the torque relation [7].

$$Torque = \begin{cases} K_a\beta_{max}(cos(\omega t) - y), -acos(y) \leq \omega t \leq acos(y) \\ 0, \quad acos(y) < \omega t < \pi - acos(y) \\ K_a\beta_{max}(cos(\omega t) - y), \pi - acos(y) \leq \omega t \leq \pi + acos(y) \\ 0, \quad \pi + acos(y) \leq \omega t \leq 2\pi - acos(y) \end{cases} \tag{5.5}$$

The torque can be represented as a sum of sinusoids if the input is assumed as sinusoidal,

$$Torque = \frac{a_0}{2} + \sum_{n=1}^{m} a_n e^{in\omega t} \tag{5.6}$$

where a_n are the Fourier coefficients.

$$a_n = \frac{1}{\pi} \int_{-\pi}^{\pi} Torque * e^{in\omega t}\, d(\omega t) \tag{5.7}$$

Then, considering Equation 5.5, the first two Fourier coefficients become,

$$a_0 = 0 \tag{5.8}$$

$$a_1 = \frac{2K_a\beta_{max}}{\pi} (\text{acos}(y) - y\sqrt{1-y^2}) \tag{5.9}$$

If higher order harmonics are neglected, then torque can be expressed as Equation 5.10.

$$Torque \cong a_1 e^{i\omega t} \tag{5.10}$$

Then, the equivalent stiffness can be written as [7],

$$K_{a\_equivalent} = \frac{2}{\pi}\left(\text{acos}(y) - y\sqrt{1-y^2}\right) K_a \tag{5.11}$$

The approach gives an estimated linear solution for different values of a parameter, "y." The technique produces flutter velocity and frequency corresponding to distinct "y" values as "y" varies monotonically. It should be noted that ‘Describing Function Method’ is a frequency domain method. A set of flutter analysis should be performed by using frequency domain flutter methods such as PK Method. For example, let us assume that there is no flutter point for a given Mach number and altitude. Then, the rotational stiffness of the control surfaces is decreased till the flutter point is found. The rotational stiffness where flutter occurs is named as a equivalent stiffness ($K_{a\_equivalent}$). For this equivalent rotational stiffness, the stiffness ratio

($\frac{K_{a_{equivalent}}}{K_a}$) is calculated. Then, 'y' is calculated from Equation 5.11. As defined previously, y is $\frac{\delta_0}{\beta_{max}}$. By using Equation 5.2, the maximum LCO amplitude (β_{max}) for a given freeplay angle (δ_0) is determined.

5.2 Actuator Implemented GFEM Freeplay Analysis

In this study, aileron, rudder, and elevator freeplay are investigated. Actuator stiffness values are selected as adjustable parameters to change the total rotational stiffness' of control surfaces. Hence, the actuator stiffness matrices are isolated from the overall stiffness matrix. The equations of equivalent stiffness method for actuator implemented model are given in Equations 3.48-3.52. Equation 5.12 shows the equation to achieve the overall nominal generalized stiffness matrix $[GK]$ by considering all control surfaces.

$$[GK] = [\phi_f]^T [K_{free}][\phi_f] + [\phi_f]^T [K_{Left\ Aileron\ Actuator}][\phi_f] + [\phi_f]^T [K_{right\ Aileron\ Actuator}][\phi_f] + [\phi_f]^T [K_{Rudder\ Actuator}][\phi_f] + [\phi_f]^T [K_{Elevator\ Actuator}][\phi_f] \quad (5.12)$$

In Equation 5.12, $[K_{free}]$ is the stiffness matrix of the finite element model for zero-actuator stiffness of all control surfaces. $[K]_{(control\ surface)actuator}$ matrices in Equation 5.12 are the matrices which include a full of zeros except for the related portion which belongs to the actuator and $[\phi_f]$ is the modal matrix which is obtained from fictitious mass implementation. In the solution process, the equivalent total rotational stiffness and stiffness ratios are calculated for nonlinear actuator elements by following the Equation 3.49 and 3.50 in each time step. The nonlinear actuator elements mean that the actuator is used to adjust the equivalent rotational stiffness. However, for the actuator implemented case, the actuator stiffness matrix cannot be multiplied with the stiffness ratio (F_S) directly. Because the actuator stiffness does not represent the overall rotational stiffness of the control surfaces directly. Therefore, Equations 3.48-3.52 should be used. For example, for the aileron freeplay

case, first, the equivalent total rotational stiffness should be found from Equation 3.40. Then, in Equation 5.13, Aileron Back-up and Wing Back-up stiffness are known from section 4.1.2. The equivalent actuator stiffness can then be found from Equation 5.13.

$$\frac{1}{Equivalent\ Actuator\ Stiffness} = \frac{1}{\frac{1}{Equivalent\ \ Total\ Rotational\ Stiffness\ of\ Aileron} - \frac{1}{Wing\ Backup\ Stiffness} - \frac{1}{Aileron\ Backup\ Stiffness}} \tag{5.13}$$

$$F_S = \frac{K_{equivalent\ actuator}}{K_{Nominal\ actuator}} \tag{5.14}$$

For the freeplay analysis, Equation 5.12 becomes,

$$\begin{aligned}[GK'] = [\phi_f]^T[K_{free}][\phi_f] + \\ [\phi_f]^T([K_{Left\ Aileron\ Actuator}] * F_{s_{\ Left\ Aileron}})[\phi_f] + \\ [\phi_f]^T([K_{right\ Aileron\ Actuator}] * F_{s_{\ Right\ Aileron}})[\phi_f] + \\ [\phi_f]^T([K_{Rudder\ Actuator}] * F_{s_{\ Rudder}})[\phi_f] + \\ [\phi_f]^T([K_{Elevator\ Actuator}] * F_{s_{\ Elevator}})[\phi_f]\end{aligned} \tag{5.15}$$

Finally, $[\ -[M_s]^{-1}[K_s]]$ term appearing in the state-space equation given by Equation 3.27, is updated in each time step as follows.

$$[K_s] = [GK'] - \frac{1}{2}\rho V^2[A_0] \tag{5.16}$$

5.2.1 Aileron Freeplay Analysis

Aileron freeplay analysis is performed for various Mach numbers and various freeplay angles. LCO amplitudes and accelerations are compared. Acceleration is considered as a resultant acceleration of three components. The node which is located on the pilot seat is connected to the aircraft fuselage section with RBE3

element and pilot seat acceleration is calculated at the reference point which is dependent node of the RBE3 element. Figure 5.1 shows the connection of the acceleration calculation point to the fuselage frame. All analysis results are not presented in this thesis. Results of the one of the selected case studies are shown in Figure 5.2 and Figure 5.3. This is the case which is performed at 0.5 Mach at the sea level for $\pm 0.4^{o}$ freeplay. Figure 5.2 and Figure 5.3 shows the rotation angle of the aileron and pilot's seat acceleration history for a duration of 3 seconds in the converged solution. Figure 5.4 and Figure 5.5 shows the phase-portrait of the aileron rotation and pilot seat grid. Figure 5.4 shows that the aileron LCO is harmonic motion. However, the pilot seat oscillation characteristic is chaotic in Figure 5.5. The rest of the analysis results are presented as a line chart as shown in Figure 5.6 and Figure 5.7. Initial condition dependency trade-offs are performed and shown in Table 5.1. The symmetric and antisymmetric rotation modes of the aileron are excited by giving an initial condition to the displacement modal coordinates. Kholodar [25] states in his article that, in the author's experience, a variation of the initial conditions leads to small alterations in the values of the LCO onset. A small value of initial conditions is usually sufficient to observe all possible LCOs. In addition to this, as Kholodar [25] states in his paper, when the freeplay angle is increased to twice the original value for the same model, the resulting magnitude of oscillation and acceleration are twice the previous value. Hence, one analysis is sufficient to determine the maximum allowable freeplay angle. Result given in Figure 5.6 and Figure 5.7 also show that oscillation and acceleration amplitudes linearly scale with the freeplay angle. In this section, the time domain freeplay analysis results are compared with the describing function results in Figure 5.8. Time domain and describing function results show good agreement in Figure 5.8.

Table 5.1 Initial Condition Dependency Trade-off

Mach	Altitude [ft]	Initial Modal Displacement	Angle of Freeplay [Degree]	Acceleration at the Pilot Seat [g]	Amplitude of LCO [Degree]
0.5	0	0.001	0.4	0.005	0.57
0.5	0	0.1	0.4	0.005	0.56
0.5	0	1	0.4	0.005	0.57

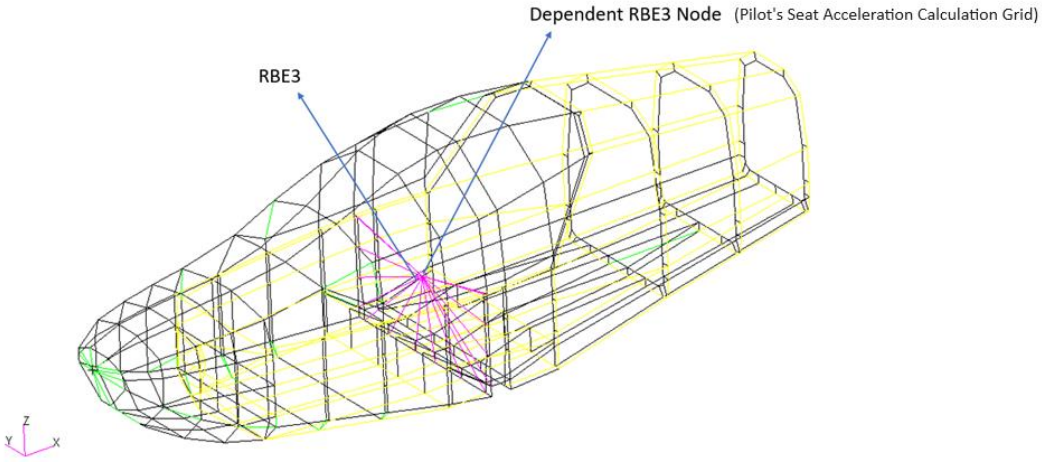

Figure 5.1. Connection of the Pilot Seat Acceleration Nodes

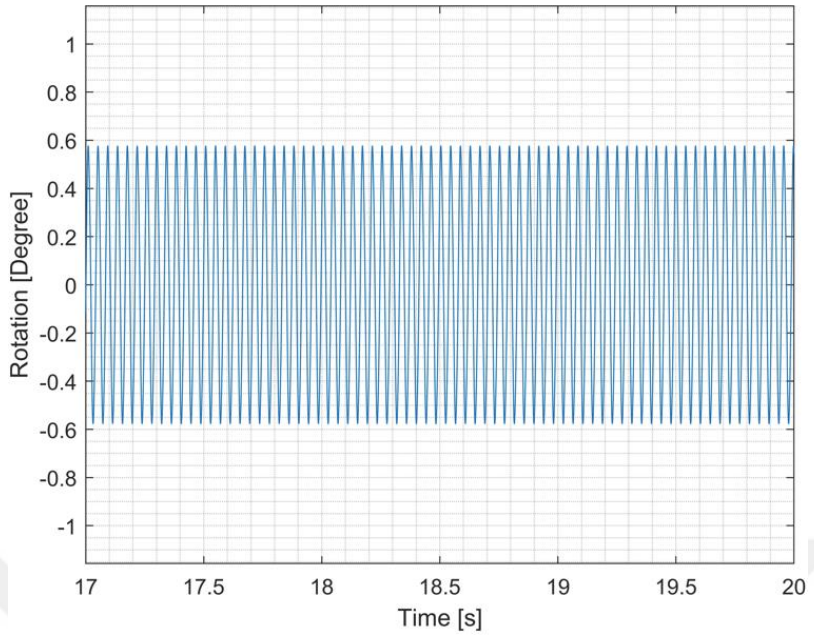

Figure 5.2. Aileron Rotation vs Time for M=0.5 and ±0.4º Freeplay

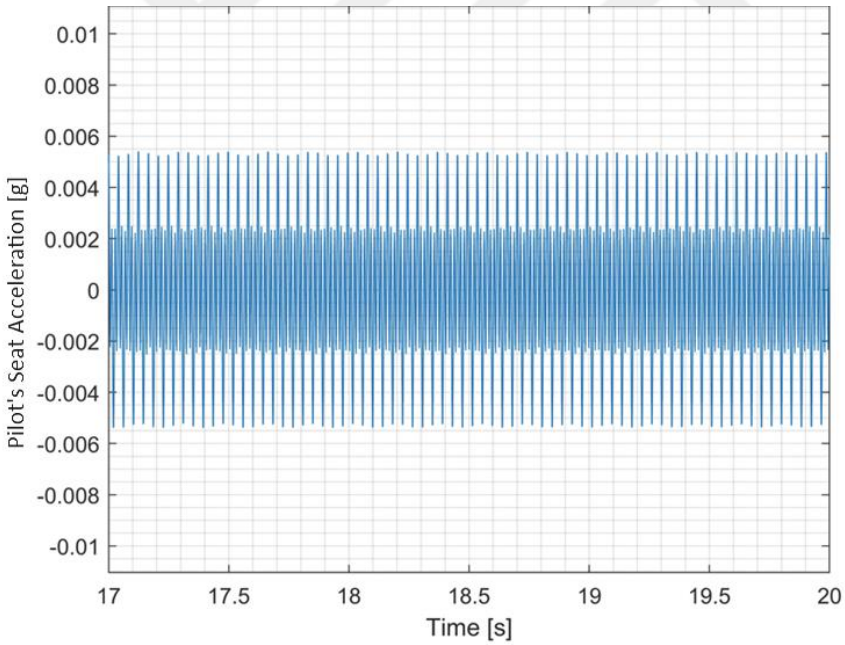

Figure 5.3. Pilot seat acceleration vs Time for M=0.5 and ±0.4º Freeplay

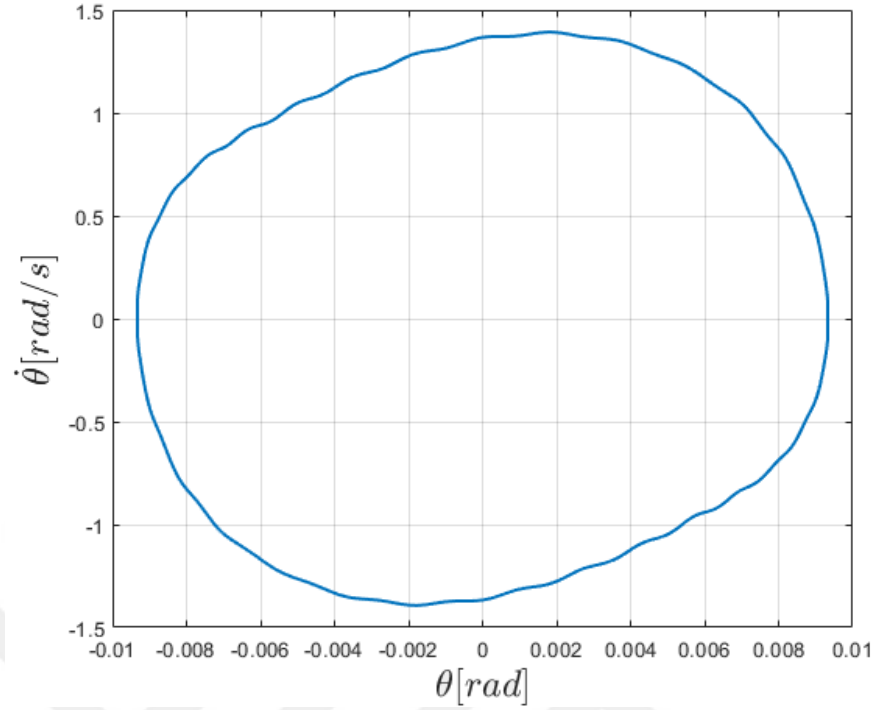

Figure 5.4. Phase-Portrait Plot for Aileron Rotation M=0.5 and ±0.4º Freeplay

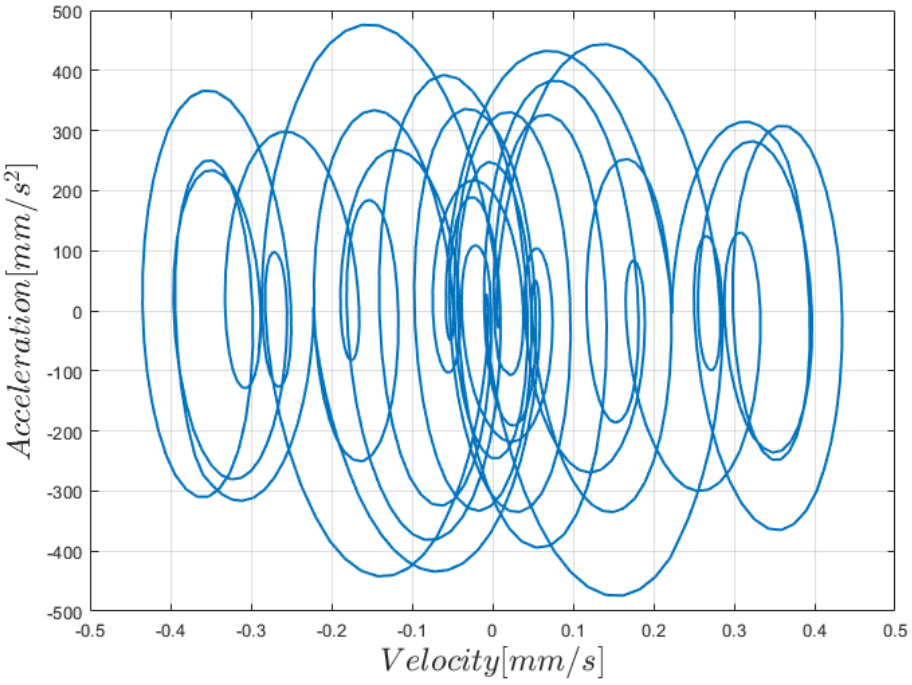

Figure 5.5. Phase-Portrait Plot for Pilot Seat M=0.5 and ±0.4º Freeplay

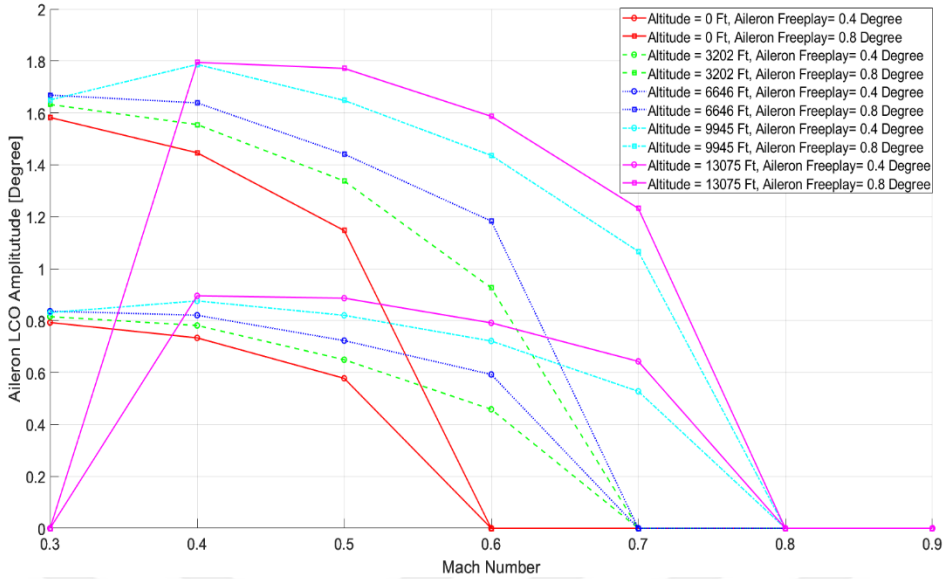

Figure 5.6. Aileron LCO Amplitudes for Different Freeplay Angles of the Aileron

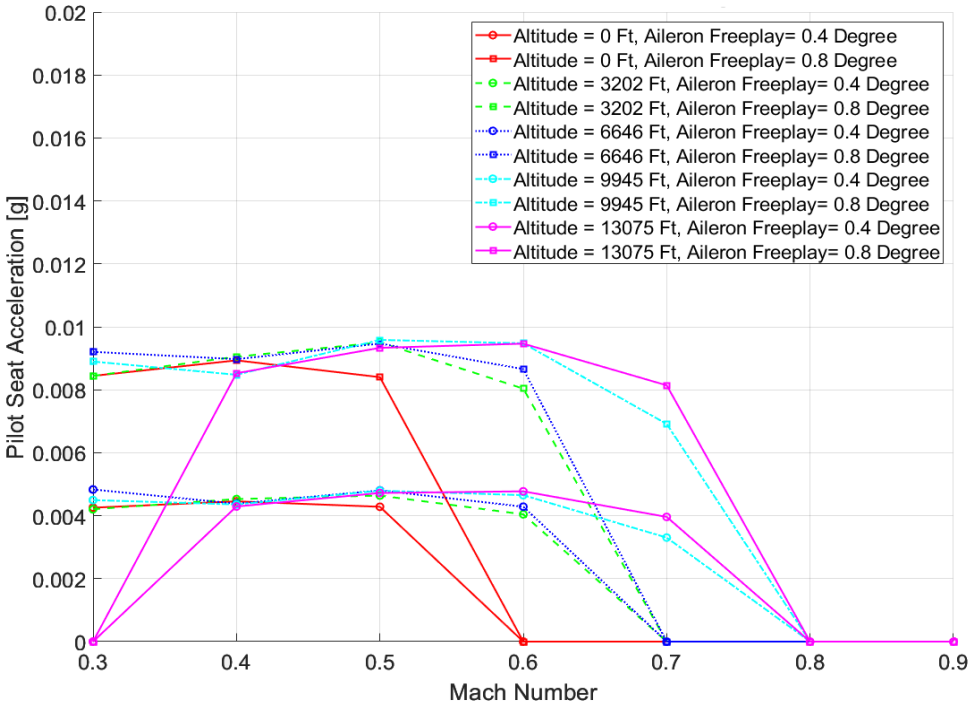

Figure 5.7. Pilot Seat Acceleration for Different Freeplay Angles of the Aileron

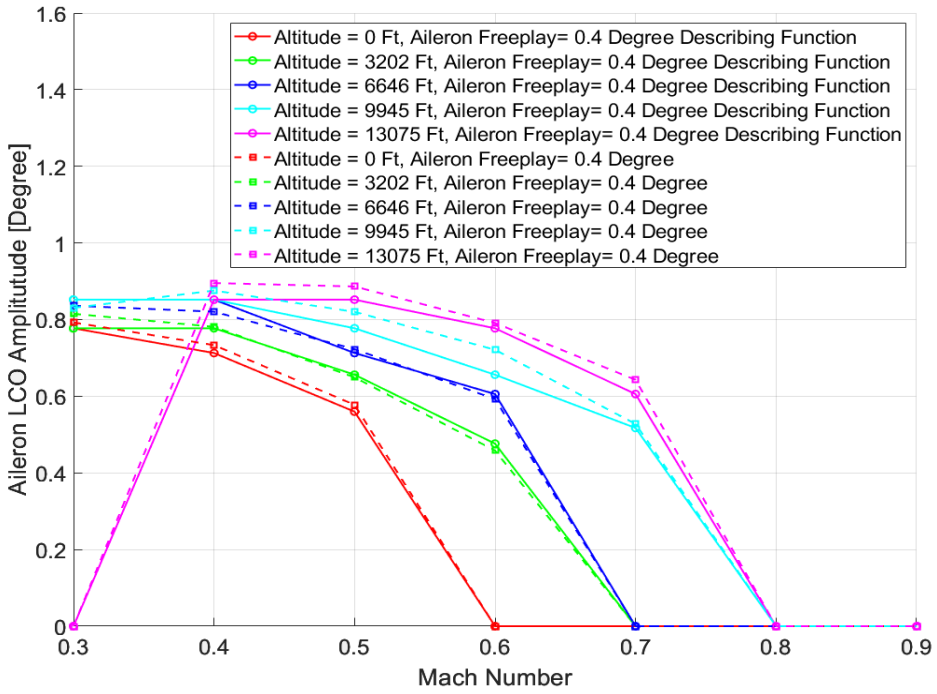

Figure 5.8. Comparison of Time Domain LCO Amplitude Results and Describing Function Results

The pilot seat accelerations are strongly related to the flutter mechanism at the relevant Mach number. There are two flutter mechanisms for the zero-rotational stiffness of the ailerons. The flutter frequencies for zero-rotational stiffness of the ailerons are around 14 Hz (Mode 3) and 22 Hz (Mode 5). The matched point flutter analysis results for zero-rotational stiffness of the ailerons are shown in Figure 5.9 and Figure 5.10.

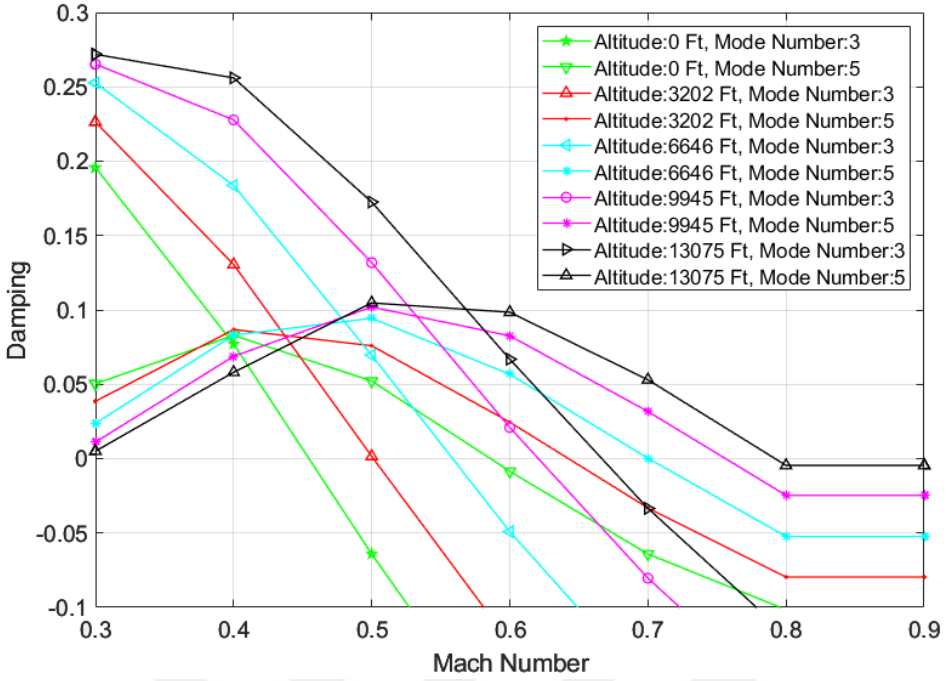

Figure 5.9. Damping vs Mach Number Curve of the Zero-Rotational Stiffness of the Ailerons

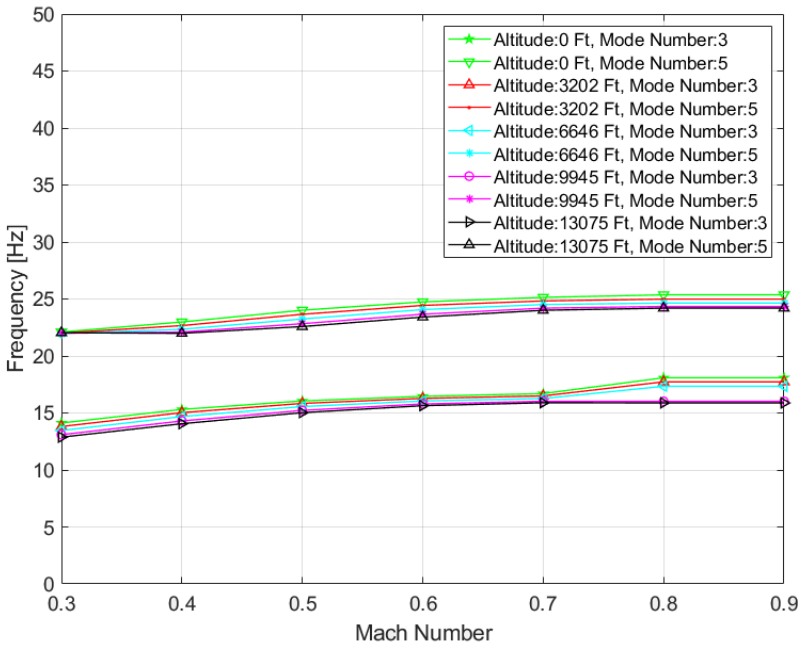

Figure 5.10. Frequency vs Mach Number Curve of the Zero-Rotational Stiffness of the Ailerons

The maximum allowable freeplay limits can be determined from Figure 5.7. The maximum acceleration occurs at 0.5 Mach and at an altitude of 9945 ft. As mentioned before, acceleration and the freeplay angles are proportional. Therefore, if the acceleration at 0.5 Mach and 0.8^o freeplay is 0.0096g, the freeplay angle at which the pilot seat acceleration does not exceed 0.12g becomes $\pm 10.00^o$. For the VLA, since the wing and the fuselage are very stiff, LCO cannot cause a very large acceleration at the pilot seat location. These results show that aileron is not critical in terms of its acceleration effects on the pilot seat. Since the allowable limit of aileron freeplay angle is very high ($\pm 10.00^o$), on the production phase of the aircraft, it can be reduced easily. It means that the allowable freeplay limit is above today's production capability. The produced aileron freeplay limit will be below this maximum allowable limit. As a recommendation, for future studies, %10 limit hinge moment restriction should be considered.

5.2.2 Rudder Freeplay Analysis

The flutter is not observed inside the flight envelope for rudder free case. In this case, there is flutter mechanism (Mode 9) at sea level and 0.9. Its damping vs Mach Number and frequency vs Mach Number figures are given in Figure 5.11 and Figure 5.12. The flutter frequency is around 41 Hz. However, this flutter point is outside envelope. The analysis will damp down if rudder only freeplay analysis performed. Because there is no instability inside the envelope for the zero-rotational stiffness.

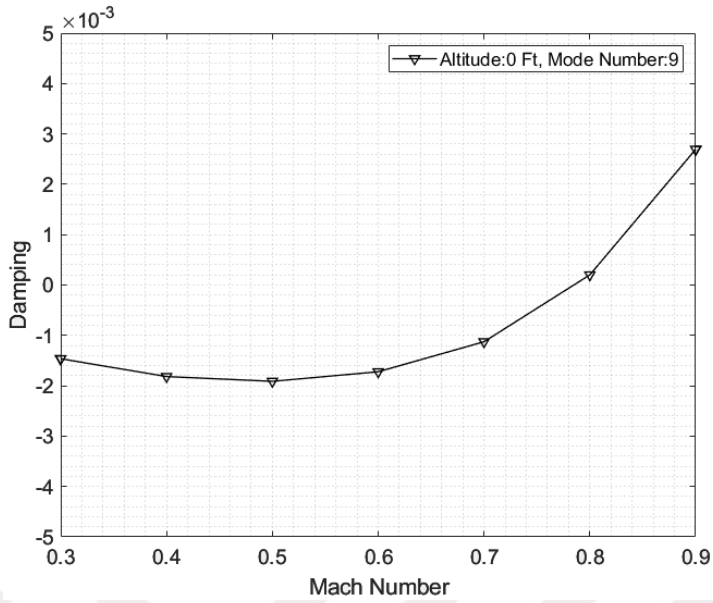

Figure 5.11. Damping vs Mach Number Curve for the Zero-Rotational Stiffness of the Rudder

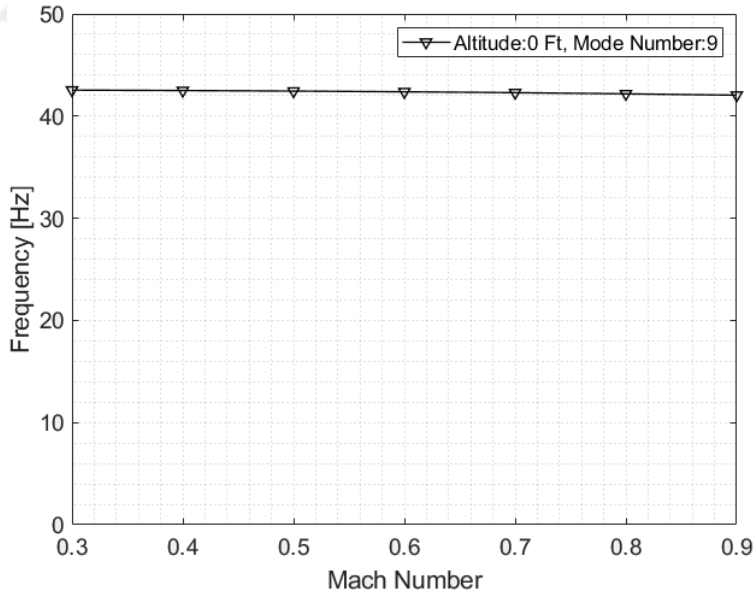

Figure 5.12. Frequency vs Mach Number Curve for the Zero-Rotational Stiffness of the Rudder

5.2.3 Elevator Freeplay Analysis

The elevator freeplay analysis is performed for different freeplay values. There is only one flutter mechanism for the zero-rotational stiffness of elevator and its frequency is around 29 Hz. The matched point flutter analysis damping and frequency vs Mach Number curves are given in Figure 5.13 and Figure 5.14. The flutter behavior of the elevator is hump mode flutter. As in the aileron freeplay case, one of the results is selected to show the behavior of the elevator rotation and the pilot seat acceleration. Figure 5.17 and Figure 5.18 shows the phase-portrait of the elevator rotation and pilot seat grid. The elevator LCO and the pilot seat oscillation characteristics are nearly harmonic motions. However, the pilot seat acceleration is chaotic in Figure 5.5. For the elevator freeplay analysis, 0.5 Mach sea level altitude and $\pm 0.4^{o}$ freeplay angle is selected as an example and time response results of the elevator rotation and the pilot seat acceleration are shown in Figure 5.15 and Figure 5.16. The rest of the analysis results are shown as a graph in Figure 5.19 and Figure 5.20. Figure 5.21 shows that time domain analysis results are well correlated with the describing function method.

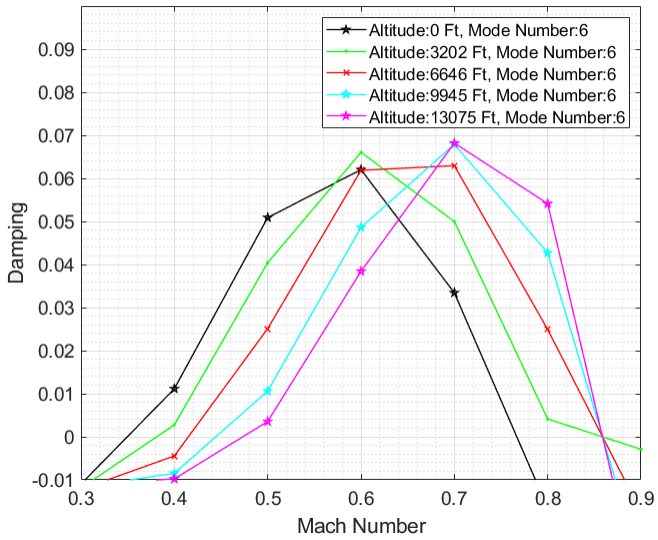

Figure 5.13. Damping vs Mach Number Curve for the Zero-Rotational Stiffness of the Elevator

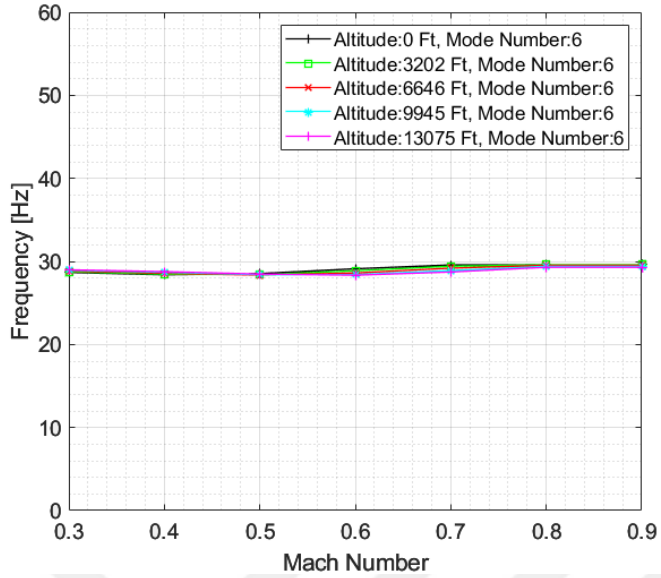

Figure 5.14. Frequency vs Mach Number Curve for the Zero-Rotational Stiffness of the Elevator

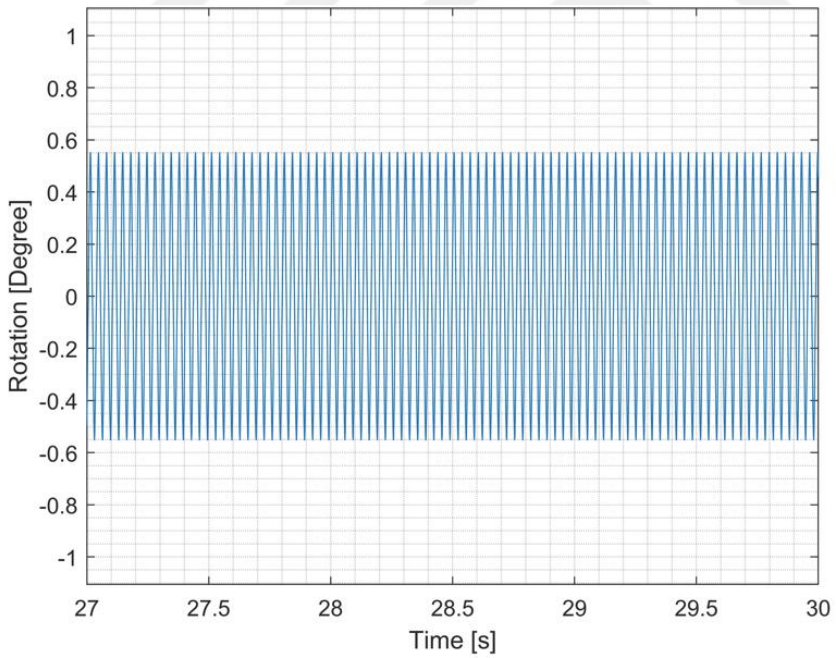

Figure 5.15. Elevator Rotation vs Time for Mach 0.5 and ±0.4^{o} Freeplay

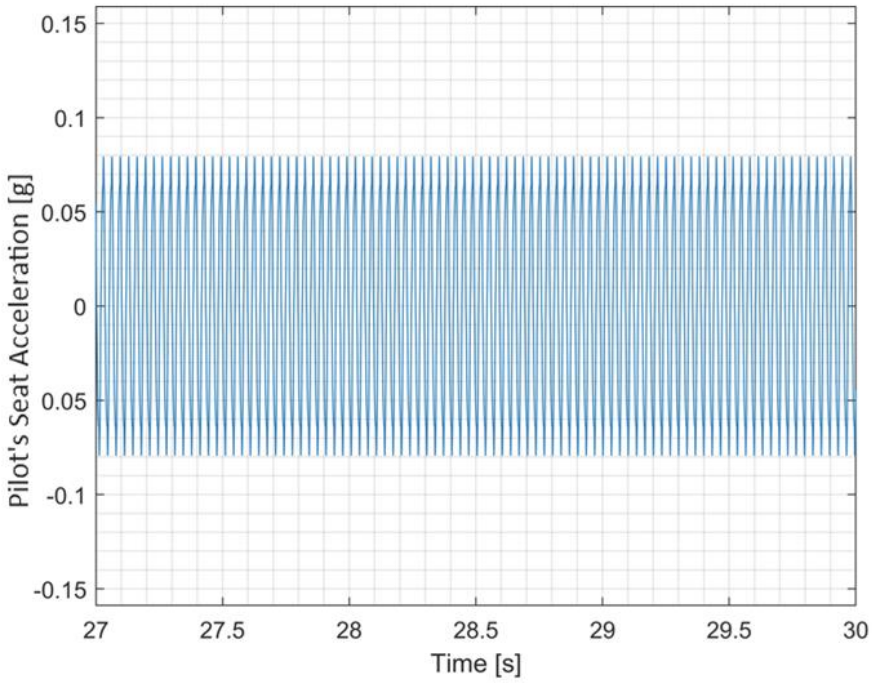

Figure 5.16. Pilot seat Acceleration vs Time for Mach 0.5 and ±0.4º Freeplay

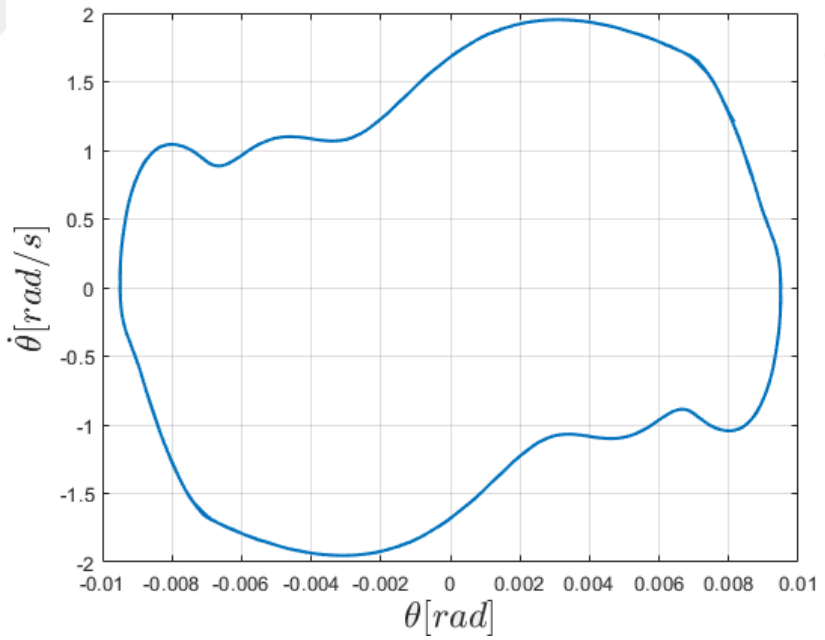

Figure 5.17. Phase-Portrait Plot for Aileron Rotation M=0.5 and ±0.4º Freeplay

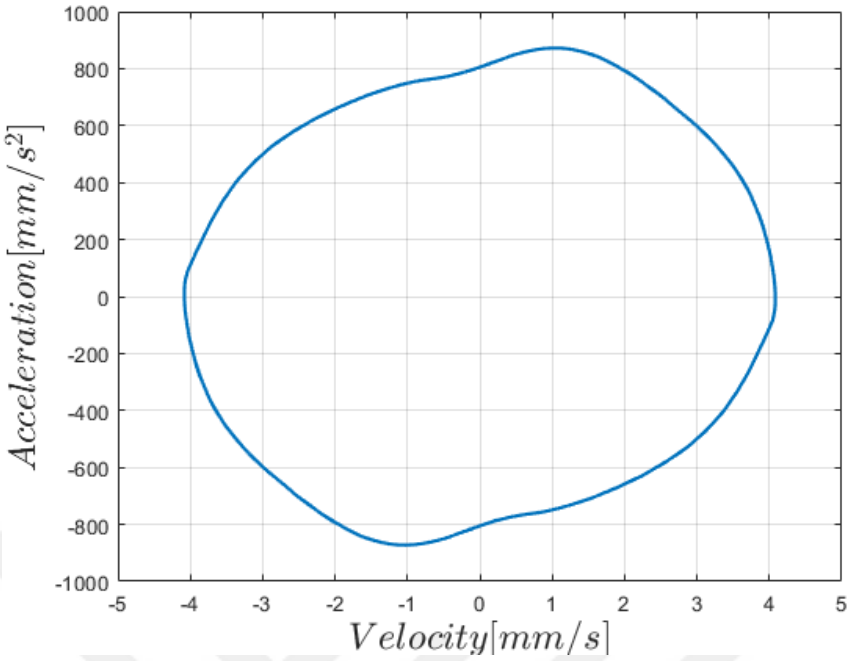

Figure 5.18. Phase-Portrait Plot for Pilot Seat M=0.5 and ±0.4° Freeplay

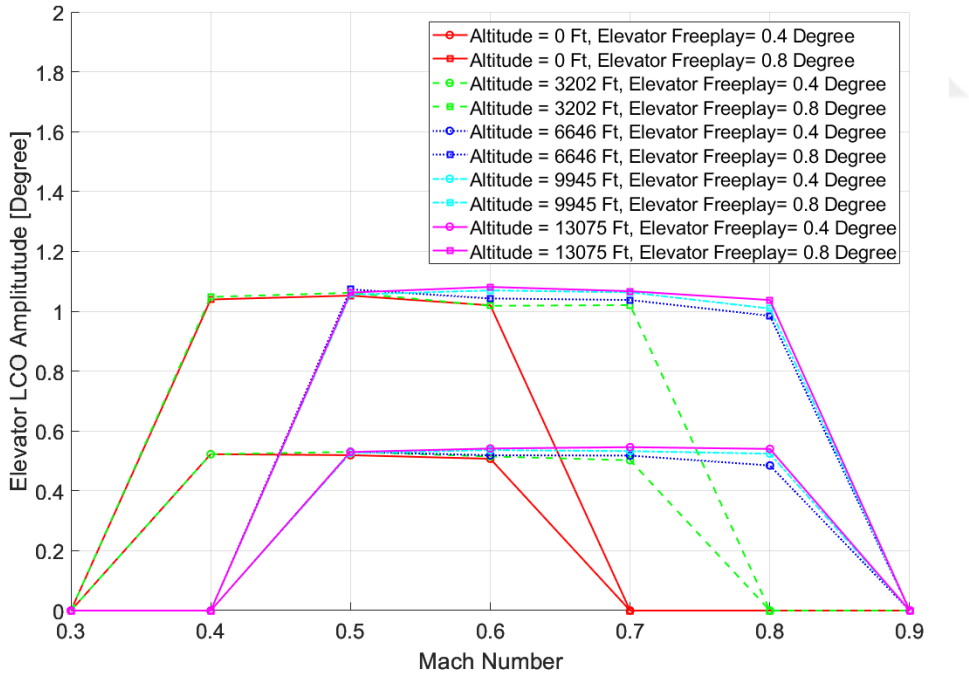

Figure 5.19. Elevator LCO Amplitudes for Different Freeplay Angles of the Elevator

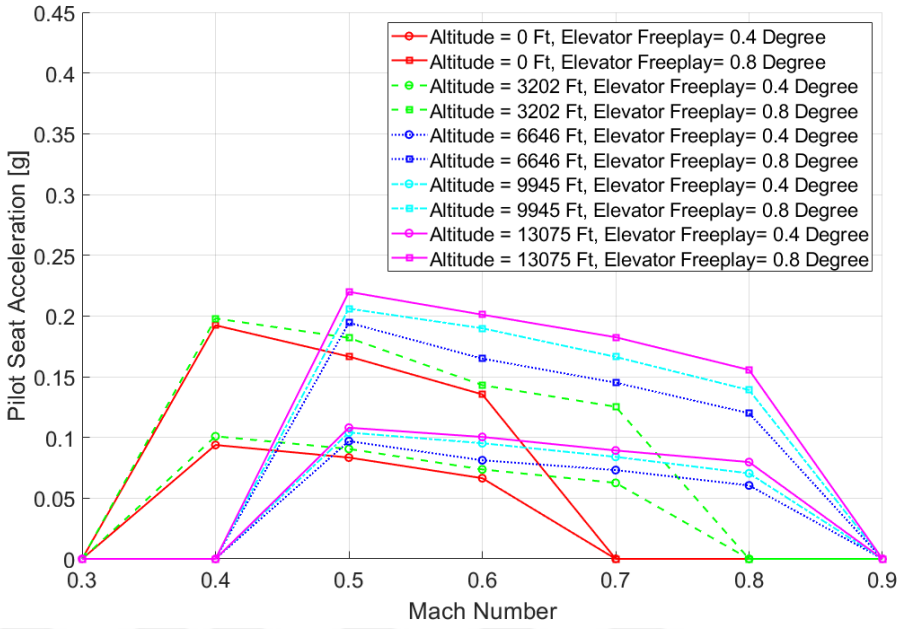

Figure 5.20. Pilot Seat Acceleration for Different Freeplay Angles of the Elevator

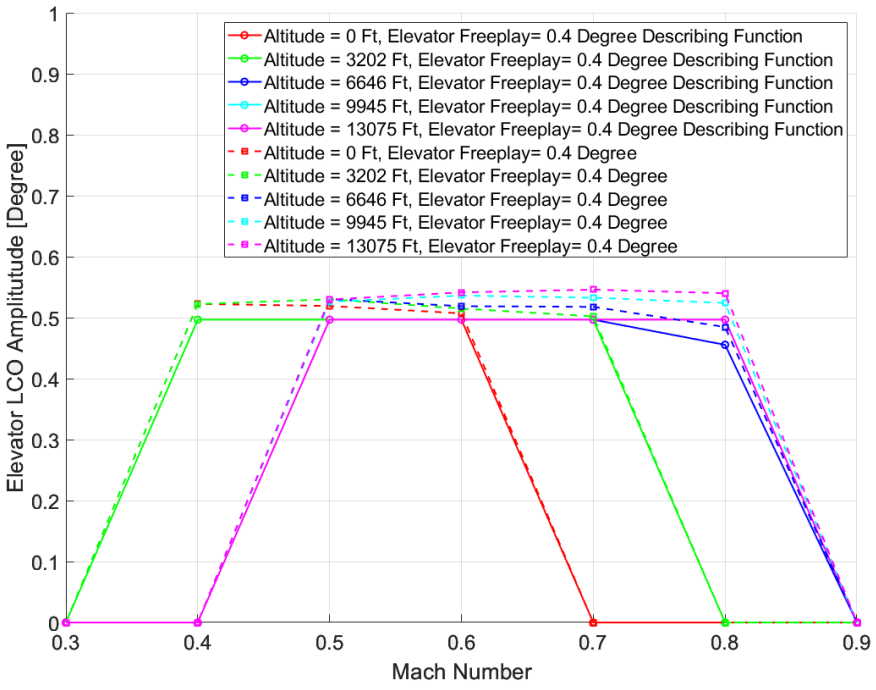

Figure 5.21. Comparison of Time Domain LCO Amplitude Results and Describing Function Results

In this case, the maximum pilot seat acceleration occurs at Mach 0.5 and at an altitude of 13075 ft as 0.22g for the 0.8° freeplay case. The results show that maximum allowable freeplay for the elevator should not exceed ±0.44^{o} in order to not to exceed the allowable pilot seat acceleration of 0.12g.

5.2.4 Simultaneous Elevator, Rudder, and Aileron Freeplay Analysis

The individual freeplay limits are determined from single control surface only freeplay analysis. However, in flight all the control surfaces affect the pilot seat acceleration. The combined freeplay analysis should be performed to be sure about the maximum limits. In the previous sub-sections, allowable freeplay values are determined considering freeplay in individual control surfaces only. Results show that critical cases occur at Mach 0.5 and altitude 13075 ft. In the present study, based on the analyses performed, it is observed that individual maximum LCO amplitude does not change significantly when the freeplay cases are combined. Also, there is no significant LCO for the rudder even if it has a high freeplay value. However, the resultant acceleration at the pilot seat is higher than the limits. Different combinations of control surface freeplays are analyzed. The elevator allowable freeplay is already tight. Therefore, the elevator freeplay value is taken as ±0.44^{o} for the combined analysis and aileron maximum allowable freeplay limits are checked. The combined analysis shows that the maximum allowable freeplay limits for ailerons should be updated as ±2.90^{o} to make pilot seat acceleration less than the maximum allowable 0.12g. As mentioned before, the RMS values of the acceleration responses are compared in this study. The critical pilot acceleration of the combined freeplay case analysis is show in Figure 5.22. The RMS of the pilot seat acceleration which is given in Figure 5.22 is 0.12g. The pilot seat characteristic of the motion is not harmonic as seen in Figure 5.23.

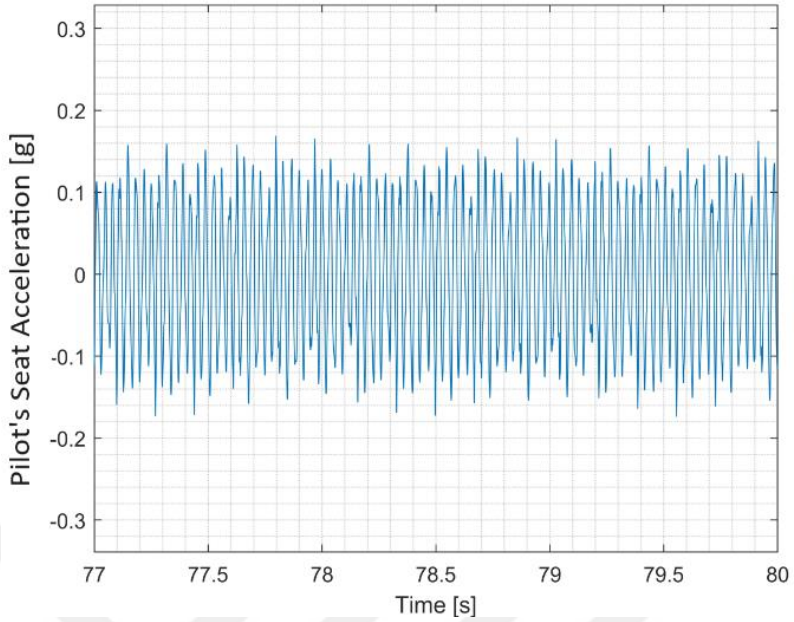

Figure 5.22. Time Responses at the Pilot Seat Acceleration Based on Simultaneous Freeplay Analysis

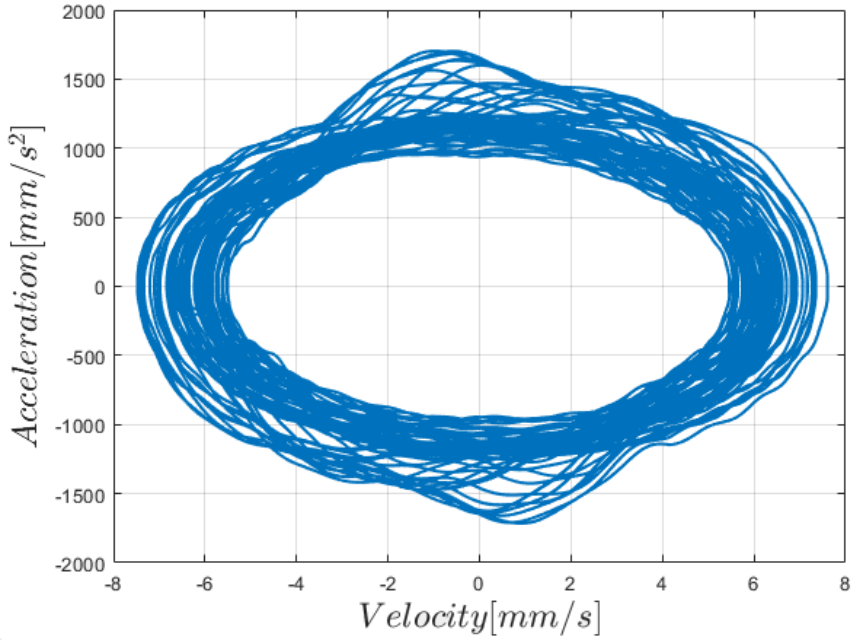

Figure 5.23. Phase-Portrait Plot for Pilot Seat for Simultaneous Freeplay Analysis

5.3 Bush Implemented GFEM Freeplay Analysis of the VLA

The procedure which is followed for the actuator implemented GFEM freeplay analysis is also followed for the bush implemented freeplay analysis of the VLA. In this case, bush stiffness values are selected as adjustable parameters to change control loop stiffness' of the control surfaces. The bush stiffness matrices are again isolated from the overall stiffness matrix for this reason. Equation 5.17 shows the equation to achieve the overall modal stiffness matrix $[GK]$ by considering all control surfaces.

$$[GK] = [\phi_f]^T [K_{free}][\phi_f] + [\phi_f]^T [K_{Left\ Aileron\ Bush}][\phi_f] + [\phi_f]^T [K_{right\ Aileron\ Bush}][\phi_f] + [\phi_f]^T [K_{Rudder\ Bush}][\phi_f] + [\phi_f]^T [K_{Elevator\ Bush}][\phi_f] \quad (5.17)$$

In Equation 5.17, $[K_{free}]$ is the stiffness matrix of the finite element model for zero-actuator stiffness of all control surfaces. Also, $[K]_{(control\ surface)Bush}$ matrices in Equation 5.17 are the matrices which include a full of zeros except the related portion which belongs to the bush element and $[\phi_f]$ is the modal matrix which is obtained from fictitious mass implementation. In the solution process, the equivalent total rotational stiffness and stiffness ratios are calculated for nonlinear bush elements by following the Equation 3.40 and 3.47 in each time step. The nonlinear bush element implies that the bush is used to adjust the equivalent rotational stiffness.

$$[GK'] = [\phi_f]^T [K_{free}][\phi_f] + [\phi_f]^T ([K_{Left\ Aileron\ Bush}] * F_{s\ Left\ Aileron\ Bush})[\phi_f] + [\phi_f]^T ([K_{right\ Aileron\ Bush}] * F_{s\ Right\ Aileron\ Bush})[\phi_f] + [\phi_f]^T ([K_{Rudder\ Bush}] * F_{s\ Rudder\ Bush})[\phi_f] + [\phi_f]^T ([K_{Elevator\ Bush}] * F_{s\ Elevator\ Bush})[\phi_f] \quad (5.18)$$

Then, $[-[M_s]^{-1}[K_s]]$ term appearing in the state-space equation given by Equation 3.27, can be updated in each time step as follows.

$$[K_s] = [GK'] - \frac{1}{2}\rho V^2 [A_0] \tag{5.19}$$

5.3.1 Aileron Freeplay Analysis

Aileron freeplay analysis is performed for different Mach numbers and freeplay angles. It should be noted that the actuator implemented GFEM model and bush implemented GFEM model flutter results are same since their dynamic characteristics are similar. The results at 0.5 Mach and at the sea level for the ±0.4° freeplay analysis are shown in Figure 5.24 and Figure 5.25. Figure 5.28 and Figure 5.29 show the aileron rotation LCO and pilot's seat acceleration history for a duration of 3 seconds in converged solution. Again, acceleration is calculated as RMS of the resultant acceleration. Figure 5.26 and Figure 5.27 shows the phase-portrait of the aileron rotation and pilot seat grid. Figure 5.26 shows that the aileron LCO is harmonic motion. However, the pilot seat oscillation characteristic is chaotic in Figure 5.27. The time domain freeplay analysis results are also compared with describing function results in Figure 5.30. Time domain and describing function results show good agreement in Figure 5.30.

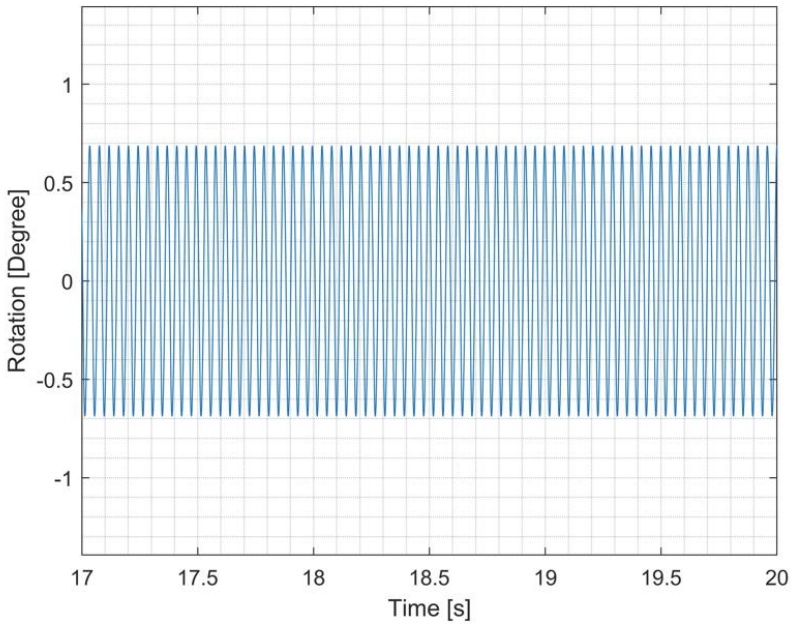

Figure 5.24. Aileron Rotation vs Time at 0.5 Mach and for ±0.4° Freeplay Angle

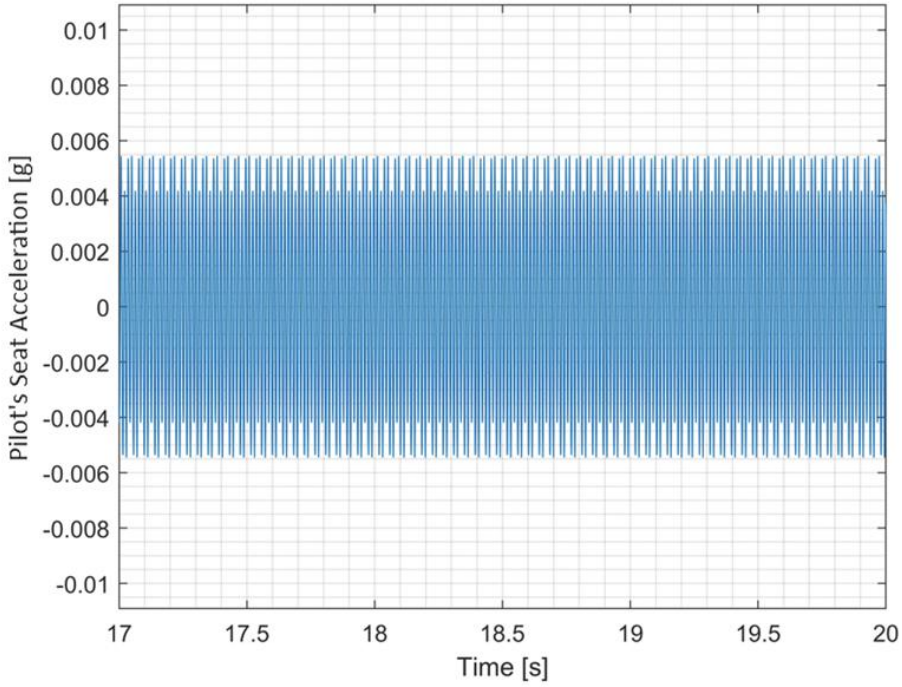

Figure 5.25. Pilot seat Acceleration vs Time at 0.5 Mach and for ±0.4º Freeplay Angle

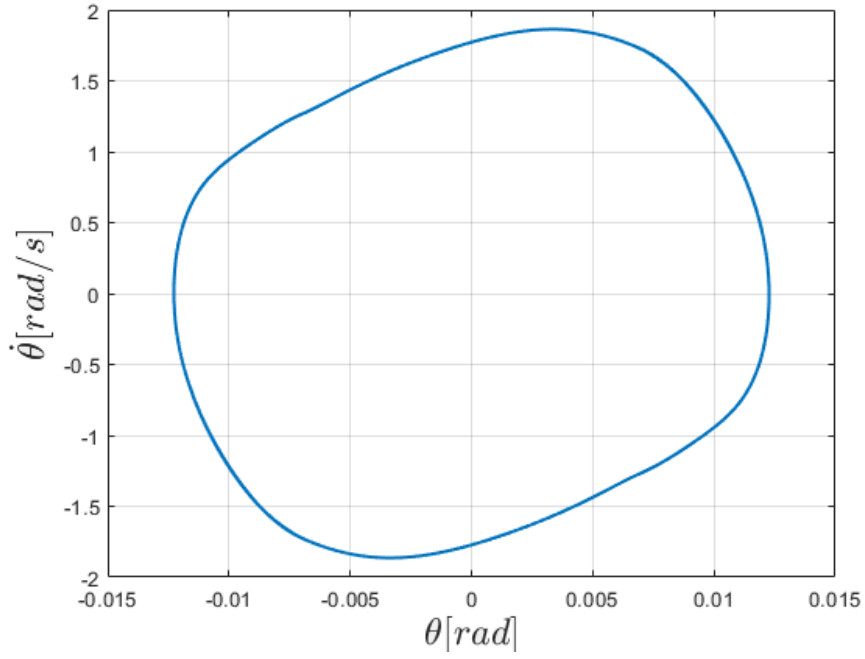

Figure 5.26. Phase-Portrait Plot for Aileron Rotation M=0.5 and ±0.4º Freeplay

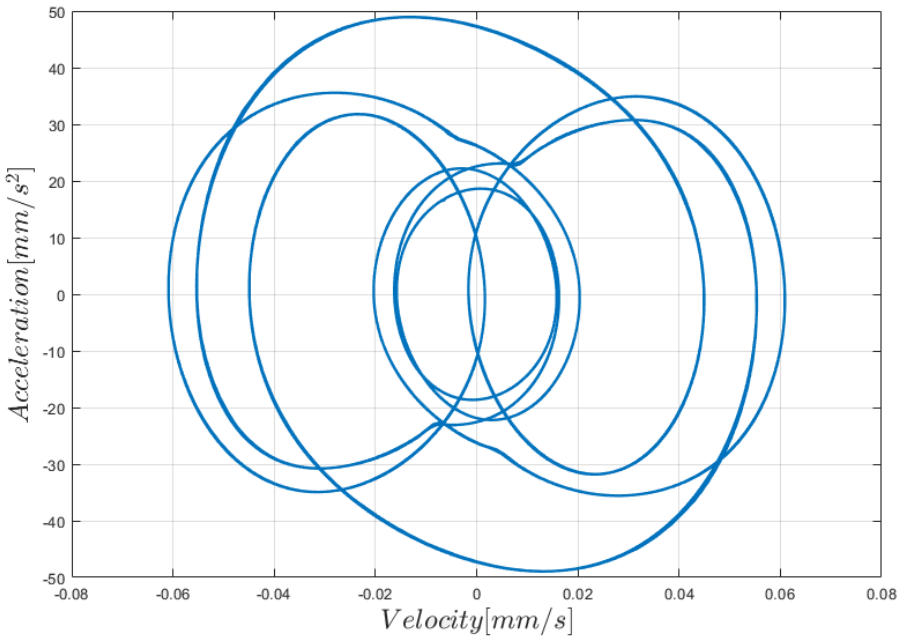

Figure 5.27. Phase-Portrait Plot for Pilot Seat Acceleration M=0.5 and ±0.4º Freeplay

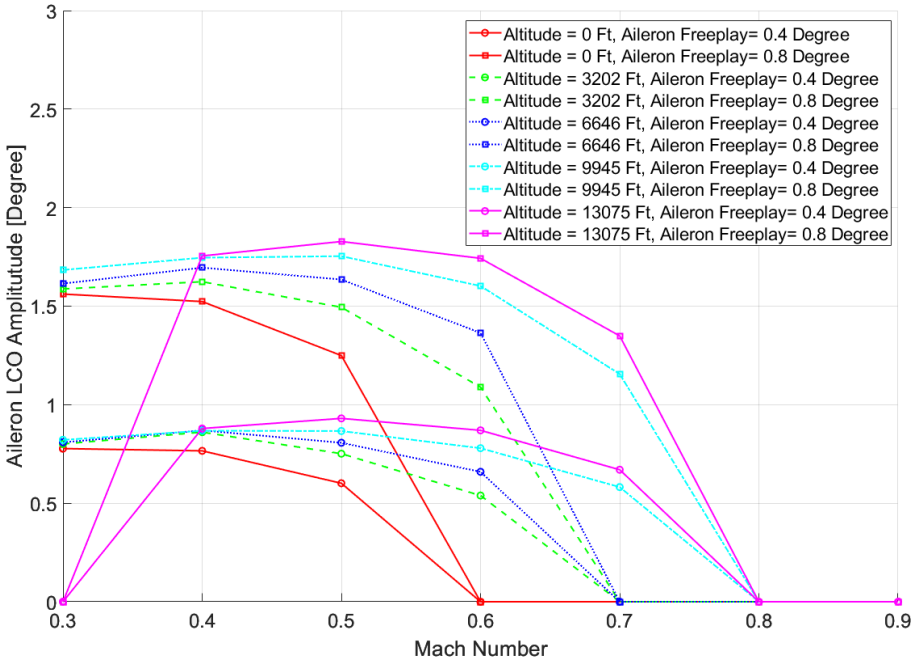

Figure 5.28. Aileron Oscillation Amplitude for Different Freeplay Angles

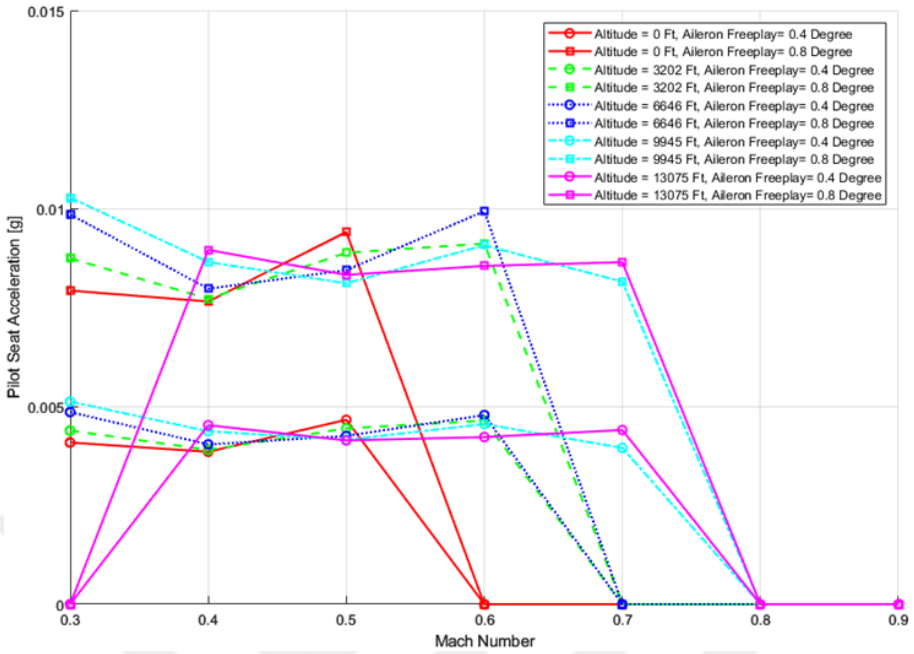

Figure 5.29. Pilot Seat Acceleration for Different Freeplay Angle

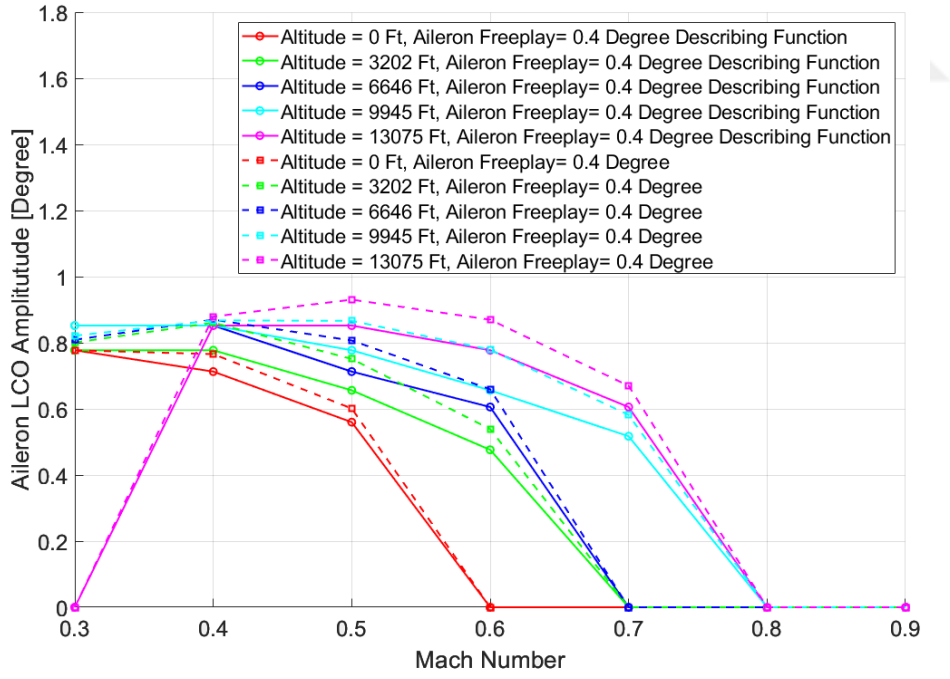

Figure 5.30. Comparison of Time Domain LCO Amplitude and Describing Function Results

The maximum allowable freeplay limits can be determined from Figure 5.29. The maximum acceleration occurs at 0.3 Mach and 9945 ft. As mentioned before, acceleration and the freeplay values are proportional. Therefore, if the acceleration for 0.3 Mach and 0.8^o freeplay is 0.011g, the freeplay angle at which the acceleration does not exceed 0.12g becomes $\pm 8.72^o$which is a very high limit freeplay angle.

5.3.2 Rudder Freeplay Analysis

As mentioned before, flutter characteristics of the bush implemented, and actuator implemented of VLA are the same. Therefore, flutter is not observed inside the envelope for the zero-rotational stiffness of the rudder. The matched point flutter analysis results are presented in Figure 5.11 and Figure 5.12.

5.3.3 Elevator Freeplay Analysis

For the bush implemented GFEM freeplay case, the elevator freeplay analysis is performed for different freeplay values. In this section 0.5 Mach, sea Level with $\pm 0.4^o$ freeplay angle is selected as an example and elevator rotation and pilot seat acceleration responses are shown in Figure 5.31 and Figure 5.32. Figure 5.33 and Figure 5.34 shows the phase-portrait of the elevator rotation and pilot seat grid. The elevator LCO is not harmonic motion. The pilot seat oscillation characteristics are nearly harmonic. The rest of the analysis results in terms of LCO amplitude and pilots seat acceleration are shown as a graph in Figure 5.35 and Figure 5.36. Figure 5.37 shows that time domain results are again well correlated with the describing function method.

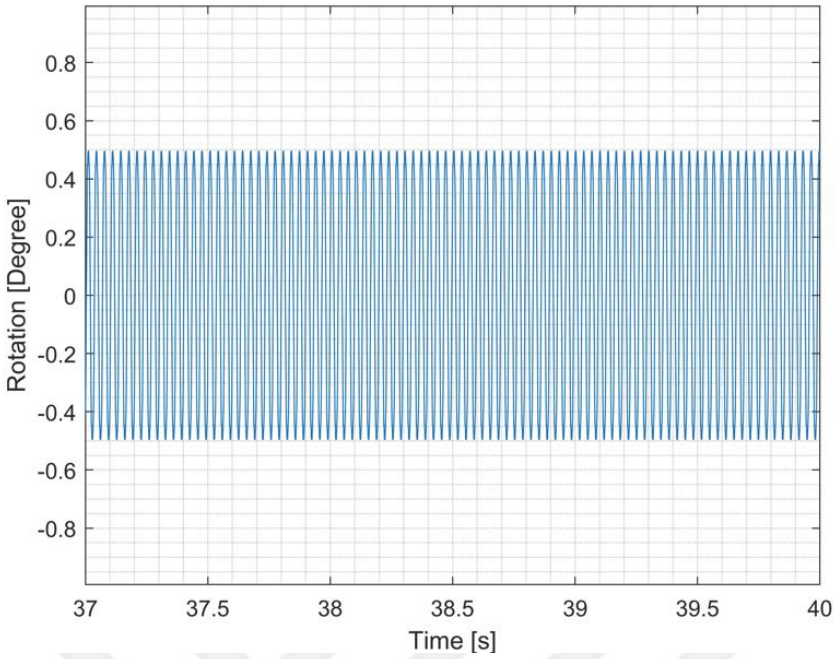

Figure 5.31. Elevator Rotation vs Time for M=0.5 and ±0.4^{o} Freeplay Angle

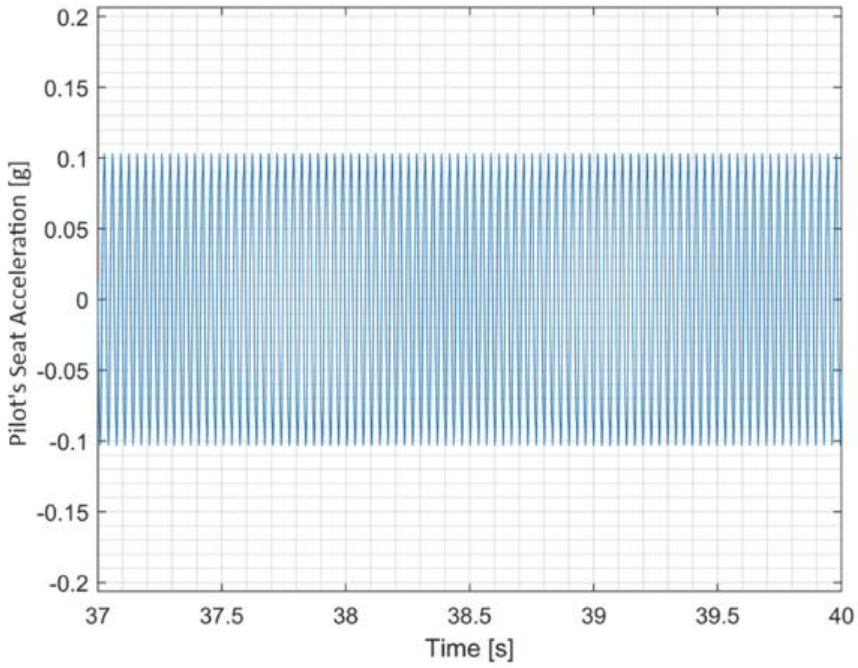

Figure 5.32. Pilot seat Acceleration vs Time for M=0.5 and ±0.4^{o} Freeplay Angle

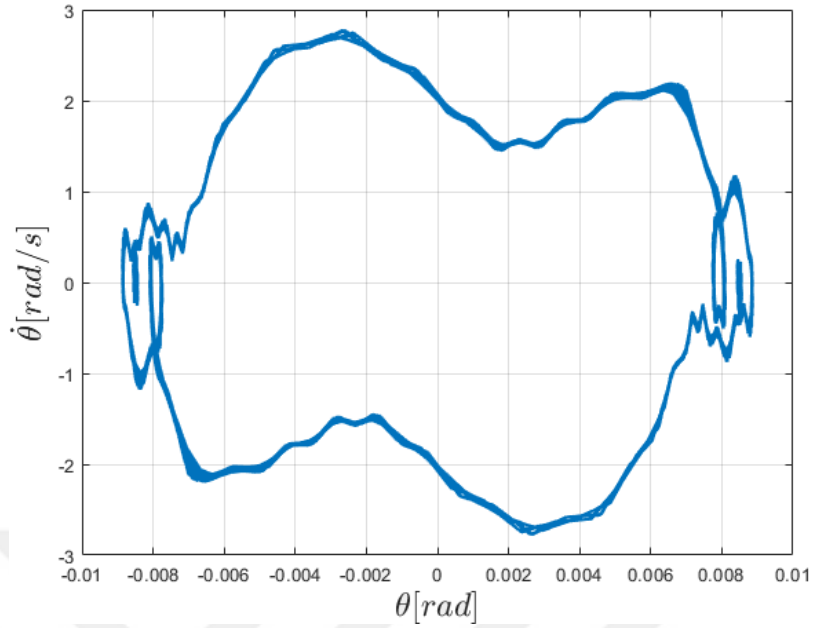

Figure 5.33. Phase-Portrait Plot for Elevator Rotation M=0.5 and ±0.4º Freeplay

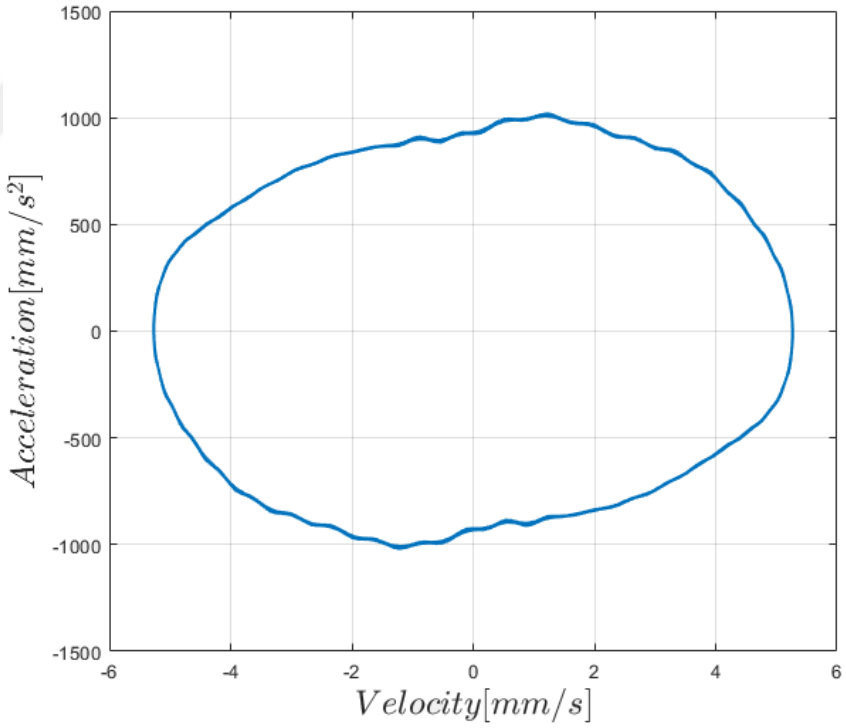

Figure 5.34. Phase-Portrait Plot for Pilot Seat M=0.5 and ±0.4º Freeplay

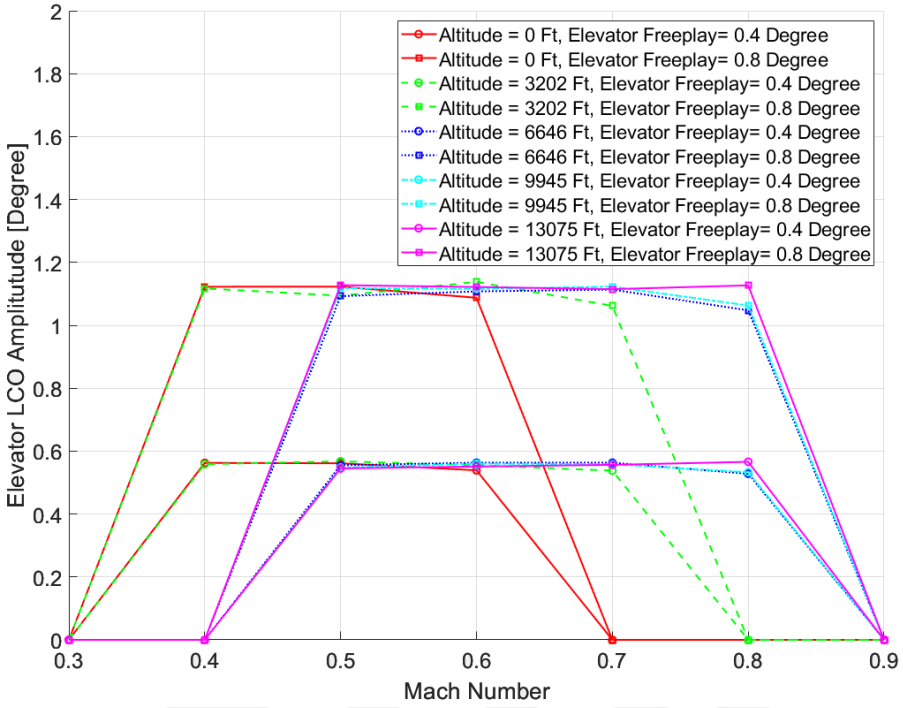

Figure 5.35. Elevator Oscillation Amplitude for Different Freeplay Angles

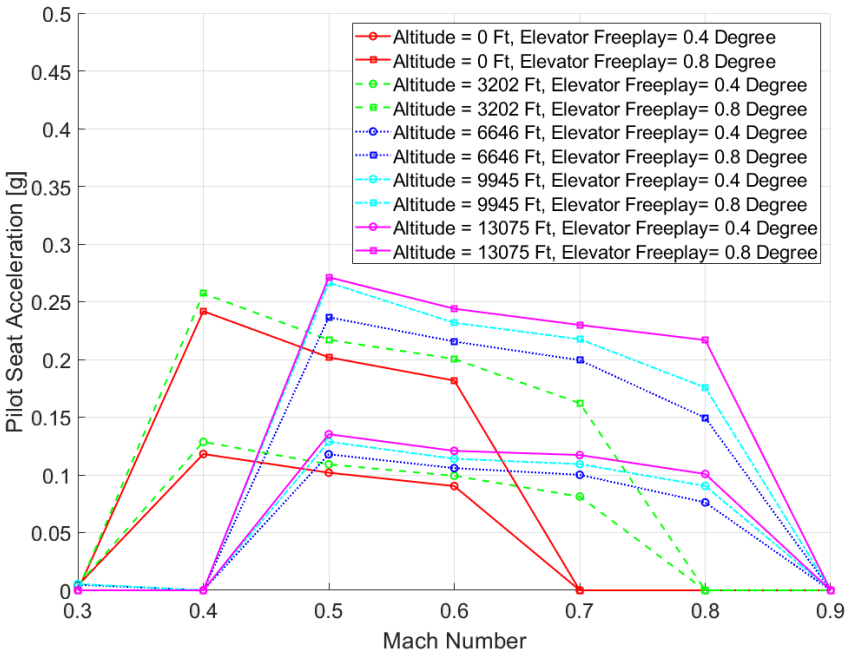

Figure 5.36. Pilot Seat Acceleration for Different Freeplay Angles

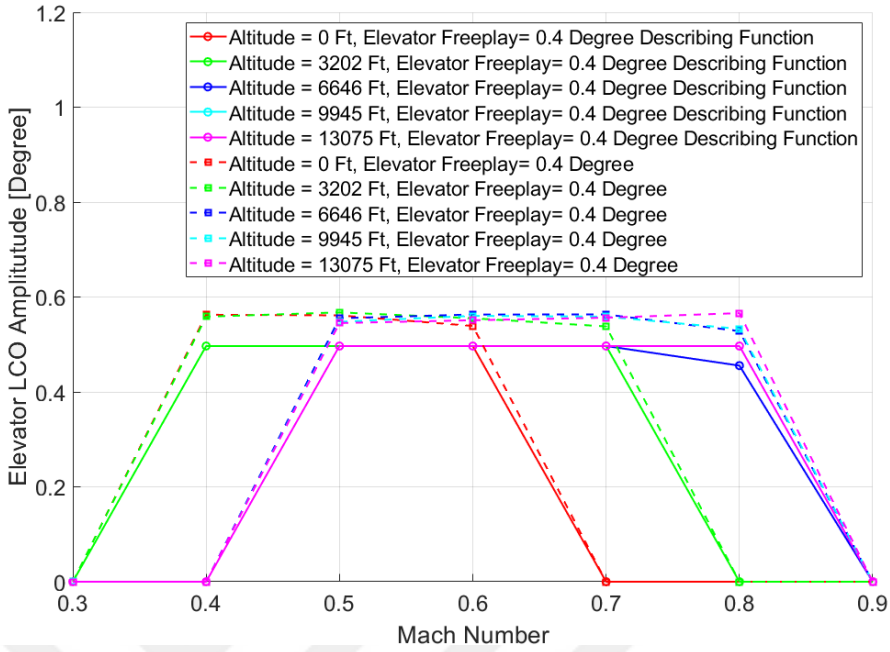

Figure 5.37. Comparison of Time Domain LCO Amplitude and Describing Function Results

In this case, the maximum acceleration occurs at Mach 0.5 and at an altitude of 13075 ft. The results show that maximum allowable freeplay for the elevator should not exceed ±0.36°.

5.3.4 Simultaneous Elevator, Rudder, and Aileron Freeplay Analysis

In the previous sub-sections, individual freeplay limits are determined from control surface only freeplay analysis. However, different combinations of the control surface freeplay cases should also be analyzed as in the actuator implemented GFEM freeplay analysis. The elevator allowable freeplay is already tight compared to the aileron. Therefore, the allowable elevator freeplay value is taken as ±0.36° for the combined analysis and the maximum allowable freeplay limit for the aileron is checked. Results show that critical case occurs at Mach 0.5 and at an altitude of 13075 ft. The pilot seat acceleration result is shown in Figure 5.38 for critical case. The RMS of the pilot seat acceleration is 0.12g for critical case which is shown

Figure 5.38. The pilot seat characteristic of the motion is not harmonic as seen in Figure 5.39.The combined analysis shows that the maximum allowable freeplay limit for the ailerons should be updated as ±3.10° to make pilot seat acceleration less than 0.12g.

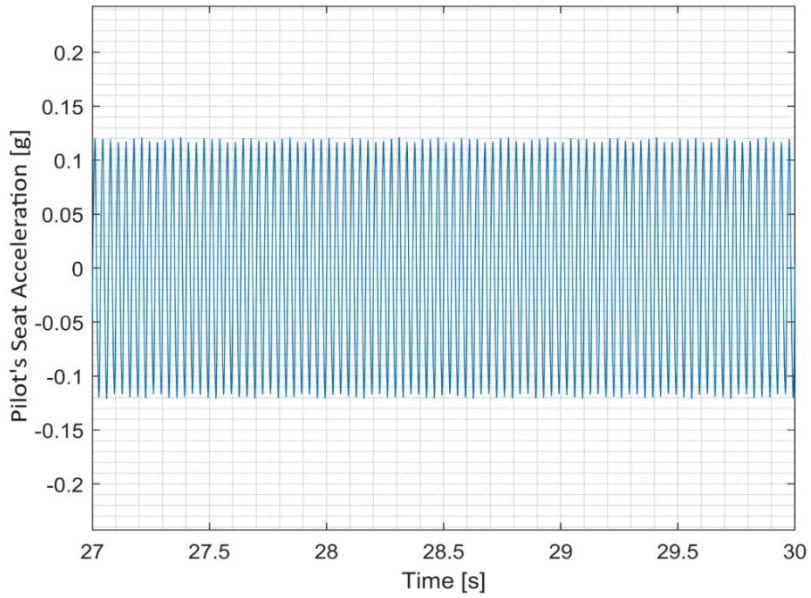

Figure 5.38. Pilot Seat Acceleration Result for the Simultaneous Freeplay Analysis

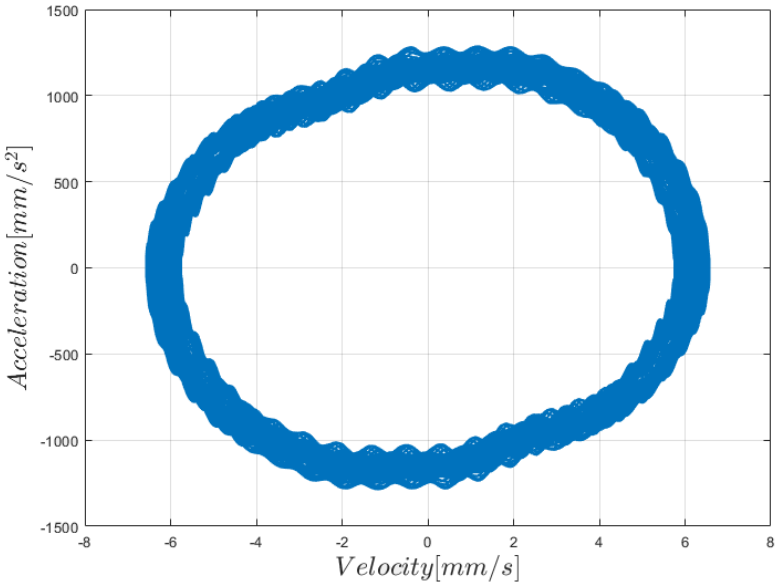

Figure 5.39. Phase-Portrait Plot for Pilot Seat for Simultaneous Freeplay Analysis

5.4 Comparison of Freeplay Analysis Results between the Bush Implemented GFEM and the Actuator Implemented GFEM

The dynamic behavior of bush implemented, and actuator implemented GFEM are determined as similar with same flutter points. Therefore, flutter driven LCO behavior is also expected to be similar. Figure 5.40 and Figure 5.41 compare the amplitudes of the LCO for both models for the individual freeplay analysis results of the aileron and elevator, respectively. Figure 5.40 and Figure 5.41 show that although the trends are similar, amplitudes of the oscillations are higher for the bush implemented case. The bush implemented GFEM analysis predicts a higher LCO amplitude than the actuator implemented GFEM for the aileron freeplay analysis. In contrast, the actuator implemented GFEM predicts higher LCO amplitude than the bush implemented GFEM for the elevator freeplay analysis. For the actuator and bush implemented GFEM analysis, Figure 5.42 and Figure 5.43 compare the pilot seat acceleration magnitudes for the aileron and the elevator freeplay cases, respectively. It is seen that the acceleration behaviors of both models are not similar for the aileron freeplay cases in terms of the trend of the variation of pilot seat acceleration with the Mach number. It means that although both systems show similar flutter behavior, the pilot seat acceleration magnitudes may converge to a different dynamic equilibrium state. It is noted that for the elevator freeplay case the trend of variation of the pilot seat acceleration with the Mach number is similar, but the resulting acceleration magnitudes are different. It is deemed that when the elevator oscillates in the actuator implement GFEM, the actuator tries to create an axial force along fuselage centerline. However, in the bush implemented GFEM model, the same oscillation tries to bend the fuselage. The reason for this difference is that even if the actuator and bush implement GFEM have the same flutter frequency and speed, the modes which are excited are different in the freeplay analysis. Table 5.2 shows the maximum of the modal displacement, velocity, and acceleration values of the elevator freeplay case at 0.4 Mach and sea level altitude with $\pm 0.4^{o}$ freeplay angle for both GFEM models. The 34 elastic modes which are

obtained after the fictitious mass implementation are used in the elevator freeplay analysis. Table 5.2 shows the maximum modal displacement, velocity, and acceleration values of each mode. As can be seen from Table 5.2, the excited modes are similar in terms of modal displacement. However, the maximum modal velocity and acceleration values are different. Therefore, this difference may cause different acceleration results in the nonlinear aeroelastic analysis. It is deemed that load path difference excites different modes apart from the flutter modes; hence it may cause the differences seen in the acceleration and LCO amplitude comparison plots.

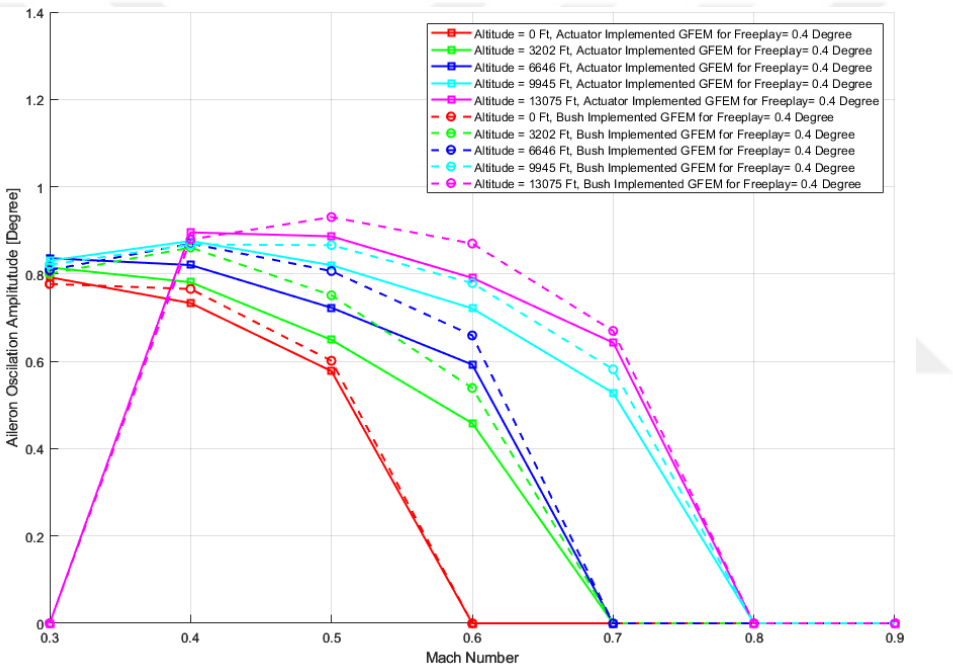

Figure 5.40. Comparison of Amplitudes of the Aileron LCO for the Actuator and the Bush Implement GFEM

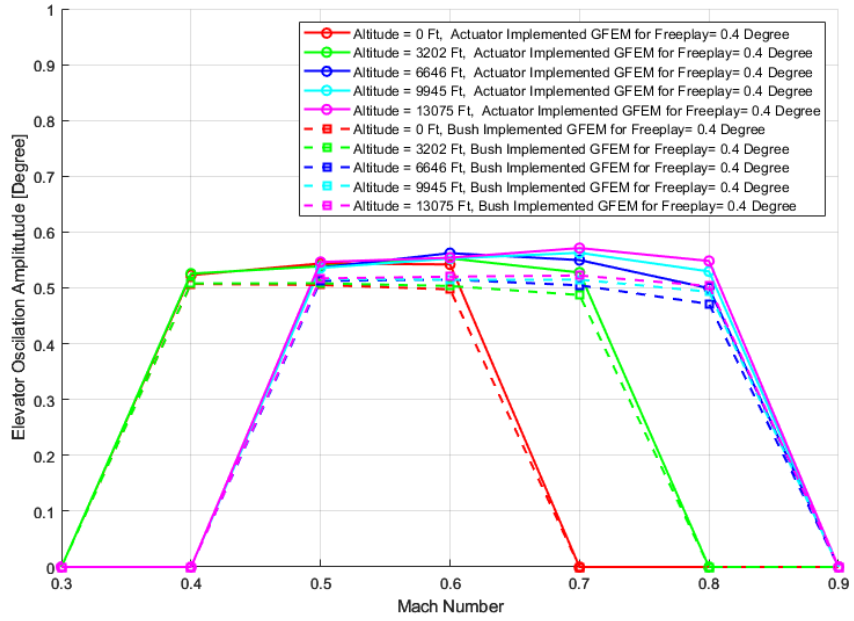

Figure 5.41. Comparison of Amplitudes of the Elevator LCO for the Actuator and the Bush Implement GFEM

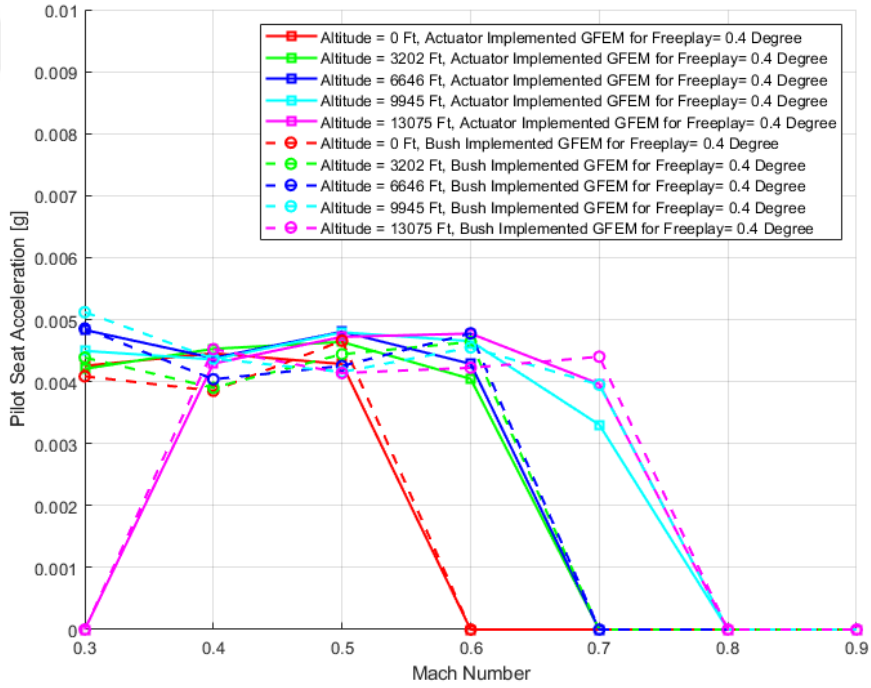

Figure 5.42. Comparison of Pilot Seat Accelerations of the Actuator and the Bush Implement GFEM Analysis for the Aileron Freeplay Case

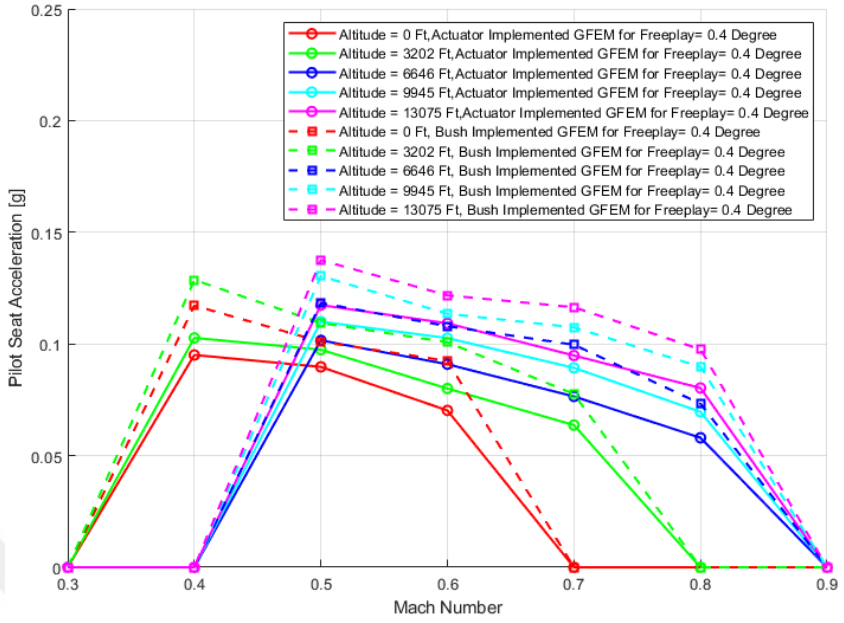

Figure 5.43. Comparison of Pilot Seat Accelerations of the Actuator and the Bush Implement GFEM Analysis for the Elevator Freeplay Case

Table 5.2 Modal Coordinate Comparison of the Bush Implemented and the Actuator Implemented GFEM of the VLA for M=0.4 and ±0.4º Freeplay Angle for the Elevator

	Bush Implemented GFEM of the VLA			Actuator Implemented GFEM of the VLA		
Mode Number #	Max. Modal Displacement	Max. Modal Velocity [1/s]	Max. Modal Acceleration [1/s^2]	Max. Modal Displacement	Max. Modal Velocity [1/s]	Max. Modal Acceleration [1/s^2]
1	0.00	0.09	109.65	0.00	0.18	98.83
2	0.00	0.02	6.38	0.00	0.05	29.40
3	0.00	0.02	17.18	0.00	0.04	14.99
4	0.00	0.06	29.19	0.00	0.10	29.12
5	0.17	32.33	6013.30	0.14	26.31	5231.37
6	0.00	0.33	117.32	0.00	0.71	291.39
7	0.00	0.10	29.48	0.00	0.13	62.93
8	0.00	0.51	122.90	0.00	0.23	79.22

Table 5.2 continued

9	0.00	0.01	4.55	0.00	0.04	9.69
10	0.02	2.79	838.58	0.01	1.77	604.08
11	0.00	0.10	32.59	0.00	0.30	113.12
12	0.14	23.23	6918.78	0.11	16.59	6635.44
13	0.00	0.03	17.99	0.00	0.13	50.41
14	0.00	0.06	27.70	0.00	0.10	52.21
15	0.00	0.02	11.99	0.00	0.06	29.05
16	0.00	0.00	4.84	0.00	0.03	17.17
17	0.00	0.09	130.38	0.00	0.11	73.78
18	0.01	1.21	533.76	0.00	1.58	774.24
19	0.00	0.03	33.79	0.00	0.14	77.16
20	0.00	0.94	407.58	0.01	2.08	1027.39
21	0.00	0.01	16.97	0.00	0.16	88.74
22	0.00	0.87	379.11	0.00	1.64	834.58
23	0.01	1.85	799.26	0.01	4.30	2206.62
24	0.00	0.04	23.43	0.01	3.31	1694.91
25	0.00	0.27	126.28	0.01	4.34	2351.14
26	0.02	5.37	2667.42	0.03	14.53	7872.02
27	0.00	0.01	5.19	0.00	1.17	607.42
28	0.00	0.14	84.57	0.00	0.09	60.36
29	0.00	0.14	60.06	0.00	0.44	389.15
30	0.00	0.17	170.25	0.00	0.44	451.52
31	0.00	0.06	58.33	0.00	1.29	1591.38
32	0.02	7.19	10071.17	0.02	6.82	6535.23
33	0.00	0.14	268.59	0.00	0.01	16.95
34	0.00	0.78	3910.08	0.00	0.04	155.77

CHAPTER 6

CONCLUSION

6.1 General Conclusion

This chapter discusses the findings of freeplay nonlinear aeroelastic analysis of the METU VLA aircraft performed using the equivalent stiffness methodology. The primary motivation for using the equivalent stiffness methodology is that the offset moment approach requires concentrated nonlinearity. However, the control loop stiffness of a control surface cannot always be represented in the model by converting the control loop stiffness into a bush element (CBUSH) in MSC Nastran. This is because the load path on the control surface changes, and as a result, dynamic behavior of the structure may change. Since the METU VLA GFEM does not have the flight control system implementation yet, in this study actuator systems are created in the FEM. The stiffness of the actuator rods is decided by checking the flutter condition in the flight envelope. The actuator stiffness values are adjusted to generate a flutter free envelope. After the implementation of actuators to the FEM, control loop stiffness is calculated, and the model is converted into a bush implemented GFEM model. The MAC are checked to be sure on the similar dynamic behavior of the models. The results show that MAC between the bush implemented, and the actuator implemented GFEM is one for all modes. The actuator is chosen as a nonlinear element in the actuator implemented GFEM. In the bush implemented GFEM, bush elements are chosen as nonlinear elements. Then, the equivalent stiffness technique is employed. METU VLA structural model, aerodynamic model, and aeroelastic model creation are explained in detail. The fictitious mass approach is implemented and verified to be used in nonlinear aeroelastic analysis of both models. Then, the effect of freeplay is investigated. Before starting the nonlinear analysis, flutter analysis for the free control surface case is performed to determine

the possible LCO regions. It is shown that the rudder is not critical in terms of freeplay nonlinearity, and it does not create any instability in the flight envelope for zero control loop stiffness. Any disturbance given for the investigation of rudder freeplay is damped out. Aileron freeplay limits are determined as ±10.00° for the actuator implemented GFEM and ±8.72° for the bush implemented GFEM. The elevator is another critical control surface in terms of freeplay. It has the smallest freeplay limits. Its maximum freeplay angle is determined as ±0.44° for the actuator implemented GFEM and ±0.36° for the bush implemented GFEM. After determining the control surface's maximum allowable freeplay limits individually, a combined analysis that includes all the control surfaces with their freeplay is performed. Due to the combination control surfaces with freeplay, the allowable freeplay limits were expected to change. The results show that the combined case is the most critical one. Freeplay limits should be updated according to results of the combined case. The elevator has a tight allowable freeplay angle when only elevator freeplay is considered. Therefore, the freeplay limit of the elevator is taken directly for the combined analysis and total acceleration is checked by changing the freeplay limits of the aileron. According to the analysis results, the maximum freeplay limits should be updated to ±2.90° for the aileron in the actuator implemented GFEM and to ±3.10° in the bush implemented GFEM. Rudder limits cannot be determined by aeroelastic analysis. Their limits may be defined by the flight control system requirements. It should be noted that acceleration at the pilot seat is highly dependent on the local mode shape of the seat. Also, results show that even if the two dynamic systems, actuator and bush implemented GFEMs, have the same flutter frequency and speed, their excited modes at the flutter instance may be different. Therefore, converting the actuator implemented GFEM model to the bush implemented model may mislead the engineers. The equivalent stiffness approach gives reasonable results and well correlated with the results of the describing function approach which is also known as the harmonic balance method. The main conclusion of this study is that the freeplay nonlinear analysis can be performed without using concentrated stiffness associated with the freeplay.

6.2 Recommendations for Future Work

In this study, the aeroservoelastic (ASE) effects are not considered. The actuator dynamic can affect the pilot seat acceleration and it can change the allowable freeplay limits. Therefore, the state space matrix can be updated by considering the ASE effects. After that, close and open loop analysis can be performed.

The actuator modelling is created as a representative one in this study. The VLA is not fly-by-wire aircraft. After the implementation of all flight control systems to the structural model, the freeplay analysis can be performed for a more realistic actuation system of the control surfaces as a future study. In addition to this, mesh dependency study for the structural model is not performed. Before starting the nonlinear analysis, the mesh dependency study can be performed as a future work.

Finally, while determining the allowable freeplay limits of the control surfaces, other factors such as the maximum hinge moment criteria or fatigue life can be taken into account.

REFERENCES

[1] Department of Defense. (1993). *MIL-A-8870C: Military specification-airplane strength and rigidity vibration, flutter, and divergence* (pp. 9-10).

[2] Hoffman, N. R., & Spielberg, I. N. (1954). Subsonic flutter tests of an unswept all-movable horizontal tail. *Aircraft Laboratory, Wright Air Development Center, Air Research and Development Command, US Air Force TR*, 54-53.

[3] Kholodar, D. B. (2014). Nature of freeplay-induced aeroelastic oscillations. *Journal of Aircraft*, *51*(2), 571-583.

[4] Chen, P. C., & Lee, D. H. (2008). Flight-loads effects on horizontal tail freeplay-induced limit cycle oscillation. *Journal of Aircraft*, *45*(2), 478-485.

[5] Tang, D., & Dowell, E. H. (2011). Aeroelastic response induced by freeplay, Part 1: theory. *AIAA journal*, *49*(11), 2532-2542.

[6] Verstraelen, E., Dimitriadis, G., Rossetto, G. D. B., & Dowell, E. H. (2017). Two-domain and three-domain limit cycles in a typical aeroelastic system with freeplay in pitch. *Journal of Fluids and Structures*, *69*, 89-107.

[7] Pitt, D. M., & Bansal, P. (2014). Uncertainties in control surface freeplay and structural properties and their effect on flutter and LCO. In *55th AIAA/ASMe/ASCE/AHS/SC Structures, Structural Dynamics, and Materials Conference* (p. 0679).

[8] Padmanabhan, M. A., Dowell, E. H., Thomas, J. P., & Pasiliao, C. L. (2016). Store-induced limit-cycle oscillations due to nonlinear wing-store attachment. *Journal of Aircraft*, *53*(3), 778-789.

[9] Liu, L., & Dowell, E. H. (2005). Harmonic balance approach for an airfoil with a freeplay control surface. *AIAA journal*, *43*(4), 802-815.

[10] Sebastiano, F., & Ricci, S. (2013). High order harmonic balance applied to an aeroelastic T-tail model with a control surface freeplay. In *54th AIAA/ASME/ASCE/AHS/ASC Structures, Structural Dynamics, and Materials Conference* (p. 1704).

[11] Liu, L., Dowell, E. H., & Thomas, J. P. (2007). A high dimensional harmonic balance approach for an aeroelastic airfoil with cubic restoring forces. *Journal of Fluids and Structures*, *23*(3), 351-363.

[12] Chen, Y. M., Liu, J. K., & Meng, G. (2012). An incremental method for limit cycle oscillations of an airfoil with an external store. *International Journal of Non-Linear Mechanics*, *47*(3), 75-83.

[13] Dimitriadis, G. (2011). Shooting-based complete bifurcation prediction for aeroelastic systems with freeplay. *Journal of Aircraft*, *48*(6), 1864-1877.

[14] Bae, J. S., Yang, S. M., & Lee, I. (2002). Linear and nonlinear aeroelastic analysis of fighter-type wing with control surface. *Journal of Aircraft*, *39*(4), 697-708.

[15] Anderson, W., & Mortara, S. (2007). Maximum control surface freeplay, design and flight testing approach on the F-22. In *48th AIAA/ASME/ASCE/AHS/ASC Structures, Structural Dynamics, and Materials Conference* (p. 1767).

[16] Chen, F., Liu, J., & Chen, Y. (2014). Flutter analysis of an airfoil with nonlinear damping using equivalent linearization. *Chinese Journal of Aeronautics*, *27*(1), 59-64.

[17] Panchal, J. (2020). *Freeplay Study using Peters Unsteady Aerodynamics with Applications to Probabilistic Modeling* (Doctoral dissertation, Rutgers The State University of New Jersey, School of Graduate Studies).

[18] Chung, K. W., Chan, C. L., & Lee, B. H. K. (2007). Bifurcation analysis of a two-degree-of-freedom aeroelastic system with freeplay structural

nonlinearity by a perturbation-incremental method. *Journal of Sound and Vibration*, *299*(3), 520-539.

[19] Vasconcellos, R. M., Abdelkefi, A., Hajj, M. R., Almeida, D. P., & Marques, F. D. (2016). Airfoil control surface discontinuous nonlinearity experimental assessment and numerical model validation. *Journal of Vibration and Control*, *22*(6), 1633-1644.

[20] Lee, D. H., & Chen, P. C. (2006). Nonlinear aeroelastic studies on a folding wing configuration with freeplay hinge nonlinearity. In *47th AIAA/ASME/ASCE/AHS/ASC Structures, Structural Dynamics, and Materials Conference 14th AIAA/ASME/AHS Adaptive Structures Conference 7th* (p. 1734).

[21] Dai, H., Yue, X., Yuan, J., Xie, D., & Atluri, S. N. (2015). A comparison of classical Runge-Kutta and Henon's methods for capturing chaos and chaotic transients in an aeroelastic system with freeplay nonlinearity. *Nonlinear Dynamics*, *81*, 169-188.

[22] Chen, Y. M., & Liu, J. K. (2014). Nonlinear aeroelastic analysis of an airfoil-store system with a freeplay by precise integration method. *Journal of Fluids and Structures*, *46*, 149-164.

[23] Conner, M. D., Tang, D. M., Dowell, E. H., & Virgin, L. N. (1997). Nonlinear behavior of a typical airfoil section with control surface freeplay: a numerical and experimental study. *Journal of Fluids and structures*, *11*(1), 89-109.

[24] Conner, M. D., Virgin, L. N., & Dowell, E. H. (1996). Accurate numerical integration of state-space models for aeroelastic systems with freeplay. *AIAA journal*, *34*(10), 2202-2205.

[25] Kholodar, D. B. (2016). Aircraft control surface and store freeplay-induced vibrations in aeroelastic stability envelope. *Journal of Aircraft*, *53*(5), 1538-1548.

[26] Karpel, M., & Raveh, D. (1996). Fictitious mass element in structural dynamics. *AIAA journal*, *34*(3), 607-613.

[27] Gündes, Ü. (n.d.). Two degrees of freedom flutter model. İstanbul Technical University. Retrieved from https://web.itu.edu.tr/~gundes/2dof.pdf

[28] MSC Software. (2021). Aeroelastic analysis. MSC Nastran Aeroelastic Analysis User's Guide.

[29] Sudiana, O. (2015). Doublet Lattice Method for Calculations of Steady Aerodynamic Forces on General Finite Wings in Incompressible Flow. In *Proceedings International Seminar of Aerospace Science and Technology, 2015* (No. III, pp. 18-25). LAPAN.

[30] Zona Technology. (2019). ZAERO users manual: Engineers toolkit for aeroelastic solutions. ZONA TECHNOLOGY INC

[31] DBD PUC Rio. (n.d.). https://www2.dbd.puc-rio.br/pergamum/tesesabertas/0611865_06_cap_03.pdf

[33] Karadal, F. M., Seber, G., Sahin, M., Nalbantoglu, V., & Yaman, Y. (2007, September). State space representation of smart structures under unsteady aerodynamic loading. In *Proceedings of the 4th International Aerospace Conference*.

[34] Van Oudheusden, B. W. (2000). Aerodynamic stiffness and damping effects in the rotational galloping of a rectangular cross-section. *Journal of Fluids and Structures*, *14*(8), 1119-1144.

[35] Raveh, D. E. (2008). Maneuver load analysis of overdetermined trim systems. *Journal of Aircraft*, *45*(1), 119-129.

[36] Zona Technology. (2020). ZAERO Version 9.3 Theoretical Manual.

[37] Zona Technology. (2020). ZAERO Version 9.3 Application Manual, Vol. 1.

[38] Karpel, M., & Wieseman, C. D. (1994). Modal coordinates for aeroelastic analysis with large local structural variations. *Journal of Aircraft*, *31*(2), 396-403.

[39] Karpel, M., & Wieseman, C. D. (1994). Time simulation of flutter with large stiffness changes. *Journal of aircraft*, *31*(2), 404-410.

[40] Yurtsever, U. (2022). *Nonlinear aeroservoelastic modelling and analysis of aircraft with control surface freeplay* (Master's thesis, Middle East Technical University).

[41] Wilde, K., Fujino, Y., & Masukawa, J. (1996). Time domain modeling of bridge deck flutter. *Doboku Gakkai Ronbunshu*, *1996*(543), 19-30.

[42] Bae, J. S., Kim, D. K., Shin, W. H., Lee, I., & Kim, S. H. (2004). Nonlinear aeroelastic analysis of a deployable missile control fin. *Journal of Spacecraft and Rockets*, *41*(2), 264-271.

[43] Luber, W. G. (2008). *Limit Cycle Oscillation on Control Surfaces due to Freeplay*. NATO RTO-MP-AVT-152.

[44] Zona Technology. (2020). ZAERO Version 9.3 Application Manual, Vol. 2.

[45] Tang, D., Dowell, E. H., & Virgin, L. N. (1998). Limit cycle behavior of an airfoil with a control surface. *Journal of Fluids and Structures*, *12*(7), 839-858.

[46] Carrese, R., Joseph, N., Marzocca, P., & Levinski, O. (2017). Aeroelastic response of the AGARD 445.6 wing with freeplay nonlinearity. In *58th AIAA/ASCE/AHS/ASC Structures, Structural Dynamics, and Materials Conference* (p. 416).

[47] Köse, O. (2023). Development of reduced order model for dynamic analysis of aircraft via global optimization (Master's thesis, Middle East Technical University).